8-3-2007

Remote Sensing and GIS Analysis of Spatial Distribution of Fracture Patterns in the Makran Accretionary Prism, Southeast Iran

Shankar Babu Pokharel

REMOTE SENSING AND GIS ANALYSIS OF SPATIAL DISTRIBUTION OF FRACTURE PATTERNS IN THE MAKRAN ACCRETIONARY PRISM, SOUTHEAST IRAN

by

SHANKAR BABU POKHAREL

Under the Direction of Hassan A. Babaie

ABSTRACT

This study shows that remote sensing and GIS are powerful tools in identifying geologically induced lineaments from digitally enhanced ETM+ satellite imageries and the digital elevation model (DEM) in remote areas such as the Makran accretionary prism, southeast Iran. The presence of the conjugate shear fractures in the eastern part, along with the extensional, and the presence of reidal sets associated with the subsidiary fractures of the Minab-Zendal fault system in the western part, suggests that the structural pattern changes from pure shear to simple shear from east to the west across the prism. Moreover, the gradual increase in the value of the angle between the two conjugate shear fractures, from south (coastal Makran) to north across the prism, and the presence of high-angle north-dipping reverse faults, with few south-dipping normal faults, suggest that deformation changes from brittle, in the south, to ductile in the northern part of the prism.

INDEX WORDS: Remote sensing, GIS, Lineaments, ETM+ satellite imageries, DEM, Iran, Makran, Accretionary prism, Principal component analysis, Color composite

REMOTE SENSING AND GIS ANALYSIS OF SPATIAL DISTRIBUTION OF FRACTURE PATTERNS IN THE MAKRAN ACCRETIONARY PRISM, SOUTHEAST IRAN

by

SHANKAR BABU POKHAREL

A Thesis submitted in Partial Fulfillment of the Requirements for the Degree of

Master of Science

in the College of Arts and Sciences

Georgia State University

2007

REMOTE SENSING AND GIS ANALYSIS OF SPATIAL DISTRIBUTION OF FRACTURE PATTERNS IN THE MAKRAN ACCRETIONARY PRISM, SOUTHEAST IRAN

by

SHANKAR BABU POKHAREL

Major Professor:	Hassan A. Babaie
Committee:	Seth Rose
	Jeremy W. Crampton

Electronic Version Approved

Office of Graduate Studies
College of Arts and Sciences
Georgia State University
August 2007

ACKNOWLEDGEMENT

I would like to thank Dr. Hassan A. Babaie, my thesis advisor, for all of his help, support, direction, and encouragement. I specially thank the members of the thesis committee Dr. Seth Rose and Dr. Jeremy W. Crampton for reviewing this study and providing valuable comments at such a short notice. My thanks also go to Dr. Crawford Elliott and to Mr. Ken Terrell for all of their valuable advice and help. I acknowledge the financial support provided by Georgia State University, Department of Geosciences through a teaching assistantship. Finally, I thank my friends and family especially my wife Usha, my mom and dad for their continuous support and motivation.

TABLE OF CONTENTS

LIST OF TABLES

LIST OF FIGURES

LIST OF ABBREVIATIONS

o	= Degree
2α	=Angle between the conjugate sets of fractures
3D	= Three dimensional
asl	= Above sea level
CC	=Color composite
DEM	=Digital elevation model
DN	=Digital number
ETM	=Enhanced thematic mapper
FCC	=False color composite
GIS	=Geographic information systems
HT	=Hough transformation
ILWIS	=Integrated land and water information systems
ITC	=International institute for geo information science and earth observation
km	=Kilometer
m	=Meter
M-plane	=Movement plane
NASA	=National aeronautics and aerospace administration
NIOC	=National Iranian oil company
NIR	=Near infra red
OIF	=Optimum index factor
P	=Oblique shear fracture set
PCA	=Principal component analysis
R	=Synthetic sets of Riedal shear fracture
R’	=Antithetic sets of Riedal shear fracture
RGB	=Red, green, blue
SRTM	=Shuttle radar topographic mission
TIR	=Thermal infra red
TM	=Thematic mapper
Y	=Oblique shear fracture set

ZFTB	=Zagros fold and thrust belt
σ_1	=Maximum principal compressive stress
σ_3	=Minimum principal compressive stress
%	=Percentage

CHAPTER 1

1.1 Introduction

Lineaments are natural crustal structures that may represent a zone of structural weakness (Masoud and Koike, 2006). Discontinuities such as fracture, including both fault and joint, shear zone, and any type of planar and linear feature can be observed as lineament on satellite imageries and digital elevation models (DEMs). Lineaments generally develop from strain that generate due to stress concentration around flaws, heterogeneities, and/or physical discontinuities (O'Learly et al., 1976; Davis, 1984; Clark and Wilson, 1994).

In regional scale studies, field mapping of each lineament is impossible due to the significant requirement for time and expense (Mabee et al., 1994). Extraction and analysis of lineaments from digitally enhanced satellite imageries and shaded relief maps derived from DEMs can provide base sources for regional structural and tectonic studies (Masoud and Koike, 2006; Solomon and Ghebreab, 2006). In remotely sensed images, lineaments are lines or edges of presumed geologic origin (Campbell, 1987).

Lineament identification using remote sensing technique can be done in two ways; i) visual interpretation of digitally enhanced satellite imageries, and ii) automated approach using complex statistical programs and segment tracing algorithms such as Hough Transformation (Karnieli et al., 1996; Koike et al., 1995; Dehls et al., 1998). In automated method, lineaments are derived from the brightness distribution pattern within the satellite images without supplementary geological information (Koike et al., 1998). This requires less human intervention, and relies basically on the parameters and

algorithms used for programming (Karmieli et al., 1996), which may lead to a biased output that may include lineaments originating from sources other than geological structures (Leech, et al., 2003).

In this study, I used digitally enhanced Landsat (enhanced thematic mapper) ETM+ imageries, and the hill shade maps derived from the DEM of shuttle radar topographic mission (SRTM-DEM), to extract and manually digitize the lineaments and other discontinuities such as the major faults and the axial traces of the folds in the Makran accretionary prism, southeast Iran. Most of the Makran accretionary prism is highly inaccessible since it is hidden behind inaccessible mountain barriers and deserts (Shearman et al., 1976). Rigorous climate and severe terrain (Shearman, 1976) make field mapping very difficult. The absence of good road infrastructure to support effective field work, logistical problems in this remote and harsh environment, and absence of vegetation, together with the relatively young age of the accreted rocks, provides a rationale and a unique opportunity for detailed structural analysis of faults and fractures using remote sensing and GIS in this large and widely-exposed accretionary prism. Although excellent past field work (see subsequent chapter) has led to the production of good maps and resolution of many geological problems, many outstanding questions remain unresolved. More specifically, the spatial distribution and gradient in the orientation, density, scale, and type of fractures and faults, and their relationship with the regional tectonics, are not well known in the area. In such environments, satellite images and DEMs can provide important sources of information (Nalbant and Alptekin, 1995; Vincent, 1997).

In this study, I have used a domain-based, lineament characterization technique to analyze the lineament patterns in the accretionary prism. In addition to the bearing of the traces of fractures, I have used the two-line technique to estimate the (3 dimensional) 3D attitude (i.e., strike and dip amount and direction) of fractures. The attitudes of major faults were estimated using constructed structural contours.

The study shows that remote sensing and GIS are powerful tools in identifying geologically-induced lineaments and other discontinuities. Different image filtering and stretching techniques, such as false color composites, created by combining the Landsat ETM + bands 7 (mid infra-red), 4 (near infra-red) and 2 (visible green), hill shade maps derived from SRTM-DEM, and the principal component analysis (PCA), were used to identify the linear features.

The presence of the NW-SE and NE-SW trending conjugate sets of fractures along with the N-S trending extensional set, in the eastern part of the study area, and the presence of riedal sets associated with the subsidiary fractures of the Minab-Zendan strike-slip fault system in the western part, suggests that the structural style changes from pure shear to simple shear from east to the west across the accretionary prism. Moreover , the gradual increase in the value of the angle between the two conjugate sets of shear fractures (i.e., 2α), from south (coastal Makran) to north across the prism, and the presence of high-angle north-dipping reverse faults, with few south-dipping normal faults, suggest that deformation changes from brittle, in the south, to ductile in the northern part of the prism.

CHAPTER 2

2.1 Study Area and Geological Setting

The study area is located in the Makran accretionary prism in the Sistan-Baluchestan, Hormozgan, and the southernmost part the Kerman provinces, in southeast Iran. The area also covers a small part of the Baluchistan Province in Pakistan. The coordinates of the area are between 25°03'33"N – 26°26'35"N and 56°59'38"E – 56°46'58"E (Figure 2.1).

Figure 2.1: Study area shown by four Landsat imageries.

The Makran accretionary prism is located between Strait of Hormuz in the southeastern part of Iran and Sonmani bay near Karachi Pakistan (Grando and McClay, 2007). The prism is structurally bounded to the west by Minab-Zendan, right-lateral fault system in Iran, and to the west by the left-lateral Ornach-Nal fault in Pakistan. Topographically, the prism extends from 3000 m or more below sea level (under Gulf of Oman) to a height of 1500 m above sea level (Grando and McClay, 2007). The Makran accretionary prism is formming by the northward subduction of the Arabian oceanic plate under the Eurasian plate (Regard et al., 2004). The prism is one of the most extensive accretionary prisms in the world (Barzi and Talbot, 2003), and hence considered as one of the type examples of subduction complexes (White, 1982; Platt et al., 1985; Byrne et al., 1992).

The Makran accretionary prism comprises a number of active thrust faults and thrust-related growth folds. These faults bound imbricates of folded sediment which is scraped off the subducting oceanic plate, and accreted (Grando and McClay, 2007) and underplated (Platt et al., 1995) sediment carried beneath the prism.

The sediments entering the deformation front of the Makran accretionary prism can be divided into two sections; i) lower 4 km thick Himalayan turbidites derived from the Indus fan to the east (Kopp et al., 2000) and, ii) upper 3 km thick section of the Makran sands derived from the north (Barzi and Talbot, 2003; Grando and McClay, 2007). Only the upper 4 km of this sequence is currently being accreted at the subduction zone (Barzi and Talbot, 2003). The rest is being subducted with the oceanic plate.

Generalized geological map of the Iranian Makran (Figure 2.3), compiled by McCall (2003), on the basis of work done by Paragon-Contech, Geological Survey of

Iran, and Intercon-Texas Instrument, divides the Makran accretionary prism, from south to north, into three main parts: i) Cenozoic accretionary sediments, ii) Ophiolite sequences, and, iii) Microcontinental blocks (McCall, 1997; McCall, 2003).

The width of the Cenozoic accretionary prism is extended, along north-south, 350 km on land and 150 km offshore before the active subduction front in the Indian Ocean is reached (McCall, 2003). The geological map of Iran, published by National Iranian Oil Company (NIOC, 1977), and the geological map of Sistan-Balushestan (Figure 2.2), (National Geoscience Database of Iran, www.ngdir.com), show that the southernmost coastal region of the accretionary prism is covered by Quaternary alluvial deposits. The age of the rock sequences progressively becomes older from south to north across the prism. The southernmost alluvial fans are followed to the north by Cenozoic accretionary deposits as shown in Figure 2.3. McCall (1997, 2003) divided the Cenozoic accreted sediements, from south to north, into four main sequences; i) Upper Miocene-Pliocene neritic and coastal sediments, ii) Lower-Upper Miocene neritic sediments, iii) Upper Oligocene-Lower Miocene "Flysch" turbidites and iv) Lower Eocene-Lower Oligocene "Flysch" turbidites, which are shown in Figure 2.3.

The red beds (NIOC, 1977) of the Lower-Upper Miocene neritic sediments and Upper Oligocene-Lower Miocene "Flysch" turbidites (McCall, 2003) occur in a number of packets, bounded by active thrust fault, and thrust-related growth folds (Grando and McClay, 2007) with alternating anticlines and synclines. These sequences are separated to the north, by WNW-ESE trending major faults from Paleogene flysch and wild exotic flysch throughout the prism (NIOC, 1977) which are leveled as tectonic mélange in Figure 2.2.

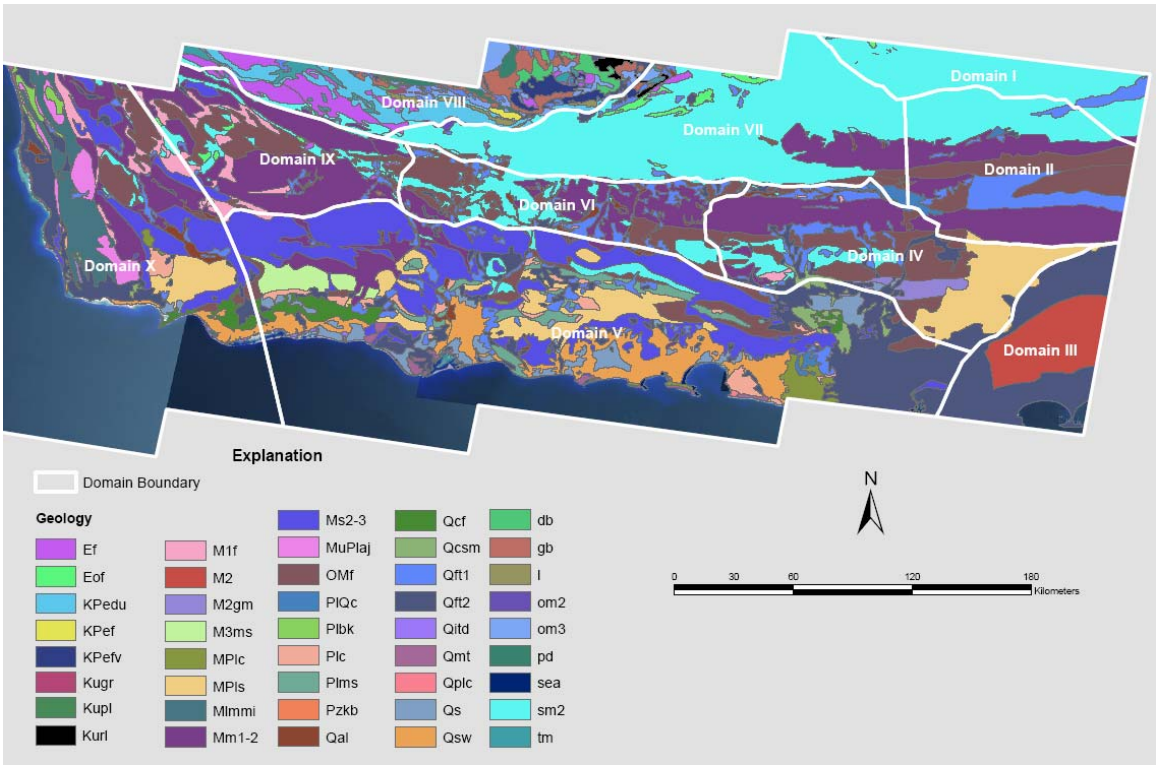

Figure 2.2: Geological map of the study area with structural domains. See Appendix A for abbreviations. [Modified after Geological map of Sistan-Baluchestan, Southeast Iran (www.ngdir.com) and NIOC, 1977]

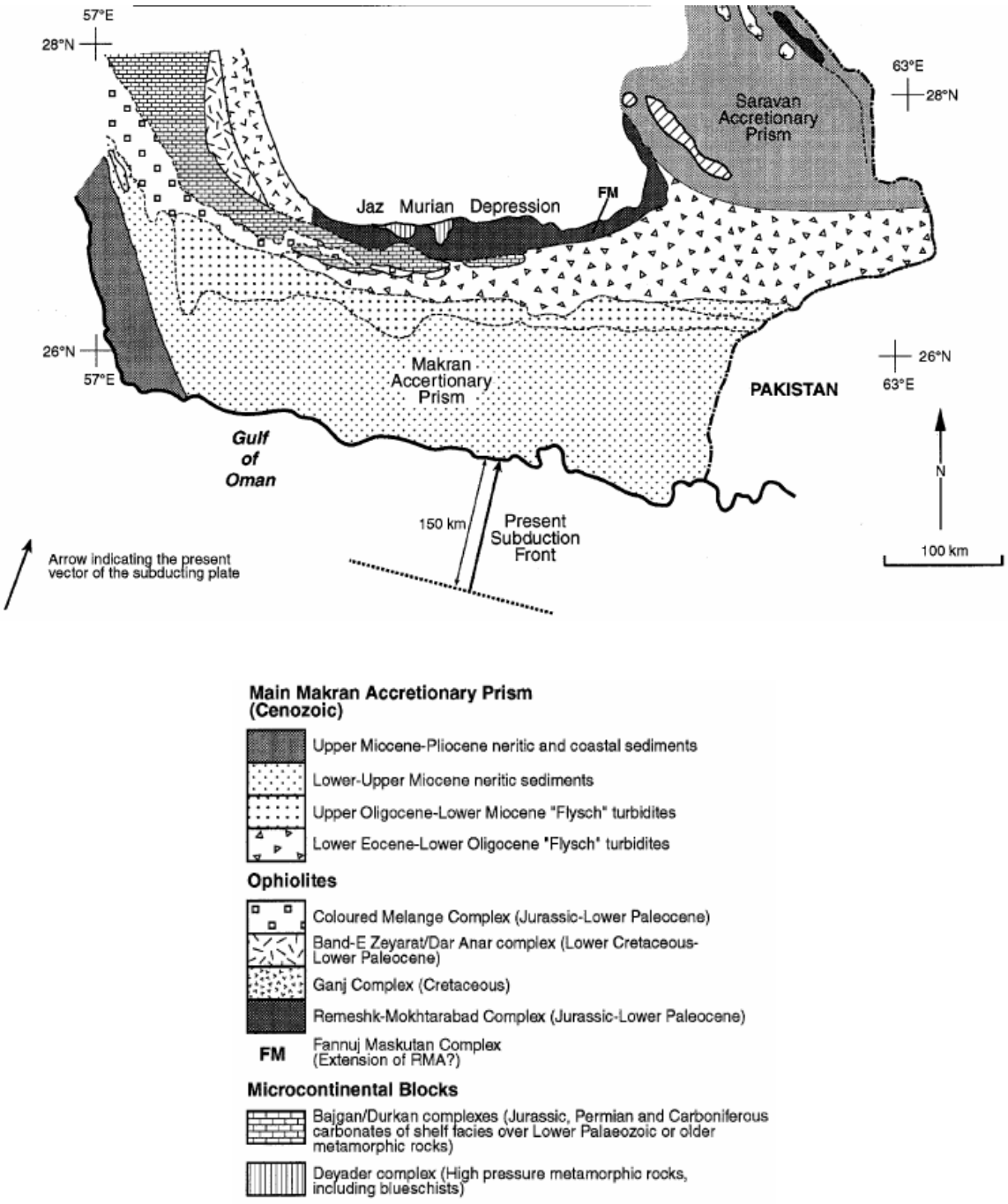

Figure 2.3: Generalized geological map of the Makran accretionary prism and the adjacent areas. [Source: McCall, 2003]

The east-west trending thrust fault that runs to the north of Kuh-e-Taku, separates the Cenozoic accretionary sediments from the Mesozoic Ophiolites and the microcontinental blocks (NIOC, 1977; McCall, 2003). Mesozoic Ophiolites are comprised of Colored Mélange complex, Band-E-Zeyarat/Dar Anar complex, Ganj complex and Remeshk-Mokhtarabad complex as shown in Figure 2.3 (McCall, 1997; McCall, 2003). Colored Mélange is the classic ophiolitic mélange of tectonic origin (McCall, 1983), formed in Jurassic-Lower Paleocene age, which represents the main Mesozoic-early Paleozoic subduction zone of Makran (McCall, 1997). The ophiolitic mélanges are chaotic assemblages of great blocks of ultramafic rock, serpentinite, pillow lava and radiolarian chert (Shearman, 1976). The Band-E-Zeyarat and overlying Dar Anar complexes (Lower Cretaceous-Lower Paleocene) consist of basic/ultrabasic rocks overlain by basaltic dykes and pillow lava interbedded by limestone and a diversity of other rock types (Shearman, 1976; McCall, 1997). The Ganj Ophiolite complex (Cretaceous age) to the north consists of sheeted dykes of intermediate to acid composition (McCall, 1997; McCall, 2003). The Remeshk-Mokhtarabad complex (Jurassic-Lower Paleocene) consists of folded magmatic layering of gabbro and leucogabbro. Parts of the Ophiolite sequences are interbedded by deep oceanic sedimentary rocks such as micrite, radiolarite, and Globotruncana limestone (McCall, 1997; McCall, 2003).

The microcontinental blocks were separated from the Gondwana in the Traissaic (Sengor et al., 1988). The microcontinental blocks are exposed to the north of Cenozoic accretionary prism together with Mesozoic ophiolites (McCall, 2003). These microcontinental blocks are divided into the Bajgan/Durkan complexes and the Deyader

complex (Figure 2.2). The Bajgan/Durkan complexes consist of metamorphic basement of early Paleozoic or older age, which is overlain to the east by Lower and Upper Cretaceous shelf limestone and remnant rafts of Carboniferous, Permian and Jurassic shelf limestone (McCall, 1997; McCall, 2003).

2.2 Previous Investigation

Remote sensing and GIS have been used to extract the spatial distribution of lineaments and other geologic structures, and to study and interpret the active tectonics in SE Iran and elsewhere. Lineaments are natural simple or composite, and linear or curvilinear features, discernible on the Earth's surface, which may depict crustal structure or represent a zone of structural weakness (Masoud and Koike, 2006). They originate mainly from strains that arise from stress concentrations around flaws, heterogeneities, and physical discontinuities, largely reflected in the form of faults, fractures, joint sets, or dykes (O'learly et al., 1976; Davis, 1984; Clark and Wilson, 1994).

Yun and Moon (2001) proposed a lineament extraction technique from DEM using drainage network, which may relate to the lineaments of the underlying bedrocks. North and Pairman (2001) proposed a smoothening filter to remote sensing imageries to detect edge boundary between two different land cover objects. Leech et al. (2003) used digitally processed Landsat TM imageries to identify the lineaments in the coastal Cordillera of northern Chile, and successfully interpreted the kinematics of the area by analyzing the statistics of lineament frequency and their spatial distribution. Nama (2004) used Landsat ETM to detect newly formed lineaments due to 1999 Mount Cameroon volcanic eruption. Ali and Pirasteh (2004) used digitally processed Landsat Enhanced

Thematic Mapper (ETM) imageries for mapping and structural interpretation in the Zagros structural belt, and concluded that remote sensing can be very helpful to detect new geologic structures, and to confirm previously field-mapped faults and folds. Jansson and Glasser (2005) found that, false color composite (FCC) images created by combining thermal infra-red (TIR) and near infra-red (NIR) bands of Landsat ETM+ draped over the digital terrain model (DTM) substantially enhanced the lineaments identification. Mostafa and Bishta (2005) used Landsat ETM+ imageries to calculate the lineament density map of Gharib-Dara area in northeastern desert of Egypt, and correlated the lineament density with radiometric map, and located new uranium targets. Abarca (2006) proposed a semi-automatic technique called Hough Transformation (HT) to extract linear features from grid based DEM in south eastern Cuba, and found that it was one of the most efficient and time economic ways to detect linear features like fold and fault. Masoud and Koike (2006) used Landsat ETM+ imageries and Digital Elevation Model, obtained from the Shuttle Radar Topographic Mission (SRTM-DEM), to analyze the spatial variation in the orientation of the lineaments, and correlated them to the geology and hydrogeology of the Siwa region, NW Egypt. Walker (2006) used remote sensing to study active faulting and folding by observing and analyzing the geomorphologic features in southern Kerman province, NW of the Makran accretionary prism in the study area.

Many authors have studied the structure, tectonics, and mechanism of latest deformation in the Makran accretionary prism in Iran and Pakistan. McCall (1997) has identified multiple co-existence of subductions: i) Mesozoic subduction, characterized by blueschist, quartzite, and marble, preserved south of the Jaz Murian Depression, ii) Cenozoic subduction, characterized by the presence of calc-alkaline intrusions north of

the the Jaz Murian Depression. Seismic study by Kopp et al. (2000), that found a series of low velocity zones within the accretionary wedge, suggests thrusting of compacted older sediments over younger ones, or presence of a large amount of fluid expulsion towards north. Landward flow of a large amount of fluid, expelled by subduction, is also evident by the presence of mud diapirs and mud volcanoes that occur in the accretionary complexes of Iran and Pakistan (Schluter, et al., 2002; Delisle, 2004). Kukowski et al. (2001) used swath bathymetric images and seismic reflection data to study the evolution and deformation of submarine convergent wedges in the Makran accretionary wedges off Pakistan. Field work done by Smith et al. (2006) suggests that the decreasing intensity of EW-trending folds and thrusts, from north to south across the prism, expresses a bulk N-S Eocene to Miocene shortening.

2.3 Aims and Objectives

The main aims of this thesis are to characterize the lineaments using remote sensing and GIS techniques and understand the tectonic origin of the linear features in the Makran accretionary prism. The principal objectives are to determine the large architecture of a part of the prism, analyze the spatial variation in the pattern and distribution of the lineaments, determine the kinematic singificance of these lineaments in accretionary tectonics, and their relation to major faults and folds. To achieve these objectives, I have used remote sensing and GIS for mapping and acquisition of fracture data, and applied statistical software, such as SPSS, for statistical analysis and interpretation of the data. The study mainly focuses on the: (1) digital enhancement of the satellite imageries based on different image processing techniques such as radiometric, spatial, and spectral enhancement techniques; (2) methods of measuring

(detecting and digitizing) the traces and lengths of lineaments including the major faults and axial traces of the folds, based on visual interpretation of enhanced satellite imageries and processed DEMs in the GIS environment; (3) kinematic analysis of the brittle structures; (4) differentiation of the structures formed by accretionary processes from those that developed due to the shearing within the Minab-Zendan strike-slip fault zone. The Minab-Zendan is a right-lateral, strike-slip fault system that transfers the Zagros collision into Makran subduction (Regard et al., 2004; Lacombe et al., 2006).

CHAPTER 3

3.1 Methodology

I used remote sensing programs ERDAS Imagine 8.7 and ILWIS (Integrated Land and Water Information Systems), version 3.3 for digital image processing. Visible, near infrared (NIR), and mid infrared (MIR) bands of the Landsat Enhanced Thematic Mapper Bands Plus (ETM+) imageries, downloaded from the Global Land Cover Facility, were used for this study. The ETM+ is the sensor onboard the Landsat 7 satellite lunched by National Aeronautics and Aerospace Administration (NASA) in 1999 (Barsi et al., 2003). The Landsat 7 satellite has a near polar sun-synchronous orbit, which rotates around the earth from the north pole to the south pole, and vice versa, and covers each place on Earth at a constant local time of day (Barsi et al., 2003). It has the revisit time of 16 days (Barsi et al., 2003; Fisher and Mustard, 2004). The ETM+ sensor can provide image data from the visible to thermal infrared spectral regions. The band characteristics of the Landsat ETM+ sensor with their wavelength and resolution are given in Table 3.1 below;

Table 3.1: Landsat ETM+ band characteristics. IR=Infrared.

Bands	**Description**	**Wavelength (µm)**	**Resolution (m)**
1	Visible Blue	0.45-0.515	30
2	Visible Green	0.525-0.605	30
3	Visible Red	0.63-0.690	30
4	Near IR	0.75-0.90	30
5	Short wavelength IR	1.55-1.75	30
6	Thermal IR	10.40-12.50	60
7	Mid IR	2.09-2.35	30
8	Panchromatic	0.52-0.90	15

I used four scenes of Landsat ETM+ imageries in this study. The path and row numbers, coordinates of the center of the imageries, sun azimuth, sun elevation and the data acquisition date are given in Table 3.2. Identification and mapping of lineaments require digital processing of the satellite imageries. The digital image processing methods, described below, includes radiometric, and spatial and spectral enhancement techniques.

Table 3.2: List of Landsat Enhanced Thematic Mapper Bands (ETM7+) imageries. [Source: Global Land Cover Facility URL: <http://glcfapp.umiacs.umd.edu:8080/esdi/index.jsp>]

Path	**Row**	**Scene Center**		**Sun Azimuth**	**Sun Elevation**	**Acquisition Date**
		Lat	Long			
156	042	26.94	60.96	105.14	65.76	2001-05-10
157	042	25.99	60.15	95.64	65.15	2000-07-17
158	042	25.99	58.60	108.48	65.62	2000-05-05
159	042	25.94	57.05	94.79	66.88	2001-05-31

3.2 Radiometric enhancement

Radiometric enhancement deals with an individual pixel of the image (Leica Geosystems, 1999). Contrast enhancement is one of the radiometric enhancement techniques applied in this study, which includes both linear and non-linear stretching, also known as histogram equalization.

3.2.1 Linear stretching

The linear stretching operation re-distributes the digital number (DN) values of an input map over a wider or narrower range of values in an output map which can, for instance, be used to enhance the contrast in the image when it is displayed (Leica Geosystems, 1999; ITC, 2001). Any raw satellite image has a narrower range of digital number (DN) values than it is capable of displaying (Leica Geosystems, 1999). Linear stretching technique stretches the DN values of the image in such a way that, the lowest input value is brought to the output value of 0 and the highest input value is brought to the output value of 255 (Leica Geosystems, 1999; Lillesand and Kiefer, 2000; ITC, 2001) and all the other values change accordingly as shown in Figure 3.1. As 0 is by default displayed in black and 255 in white, the contrast will be better when the image is displayed.

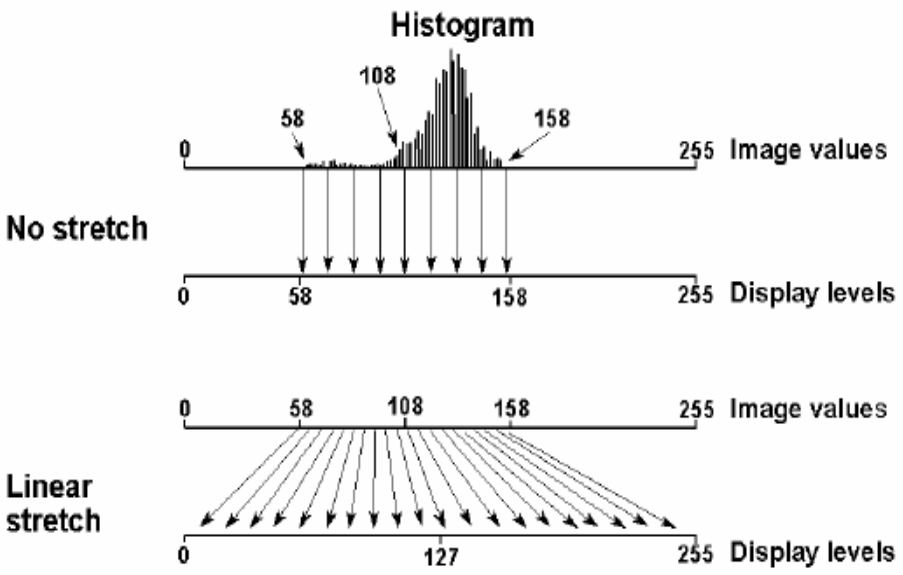

Figure 3.1: Example of linear stretching, where pixel values 58-158 are stretched to 0-255. [Source: Lillesand and Kiefer, 2000; ITC, 2001]

The linear stretching technique was applied to ETM+ band 7 of all the scenes listed in Table 3.2, the statistical parameters of both the stretched and unstretched images and their corresponding figures with histograms are shown in Table 3.3 and Figure 3.2, respectively.

Table 3.3: Statistical parameters showing the digital number values (DN) of both the stretched and unstretched ETM+ band 7 images.

	Unstretched	**Stretched**
Mean	53.25	81.68
Median	91	146
Standard Deviation	49.33	80.58

The histograms show that the original value range of the DN (10-160) has been stretched to 0-255 (Figure 3.2). Similarly, the mean, median and the standard deviation of the histograms have also become higher due to the redistribution of the DN values (Table 3.3).

3.3 Spatial enhancement

Unlike the radiometric enhancement, the spatial enhancement technique modifies the DN value of a pixel based on the values of the surrounding pixels (Leica Geosystems, 1999, p.154; ITC, 2001, ILWIS user's Guide, p.222). A spatial enhancement technique called Edge enhancement filter was applied to the images in the study. Filtering is a process in which each pixel value in a raster map is replaced with a new value. The new value is obtained by applying a certain function to each input pixel and its direct neighbors (ITC, 2001). For example, in the case of a 3x3 array (kernel) function, the surrounding pixels are 8 adjacent pixels.

3.3.1 Edge enhancement filter

I applied the Edge enhancement filter as a spatial enhancement technique. The Edge Enhancement filter is one of the linear convolution filters, which consists of a matrix with values and a gain factor (ITC, 2001). This filter works in a 3X3 environment, also known as convolution, where the 9 matrix values are multiplied with the gain factor and the result is assigned to the center pixel in the output image. This is done by altering the spectral features of an image (Jensen, 1996). The result is assigned to the center pixel in the output image. The values in the matrix are shown in Table 3.4. The Edge enhancement filter can be used to enhance the sharpness of a satellite image for better visual interpretation and to reduce noise in an image prior to a multi-band image

operation (ILWIS 3.3, online help). In the edge enhancement filter, the overall look of the output image remain the same, but the pixels at the borders of light areas become more lighter, similarly, the pixels at the dark areas become more darker, which gives the sharper impression to the output image (ILWIS 3.3, online help). The output images are shown in Figure 3.3.

Table 3.4: Standard matrix values used for the Edge enhancement filter. Gain factor = 1/8 = 0.125.

-1	-1	-1
-1	16	-1
-1	-1	-1

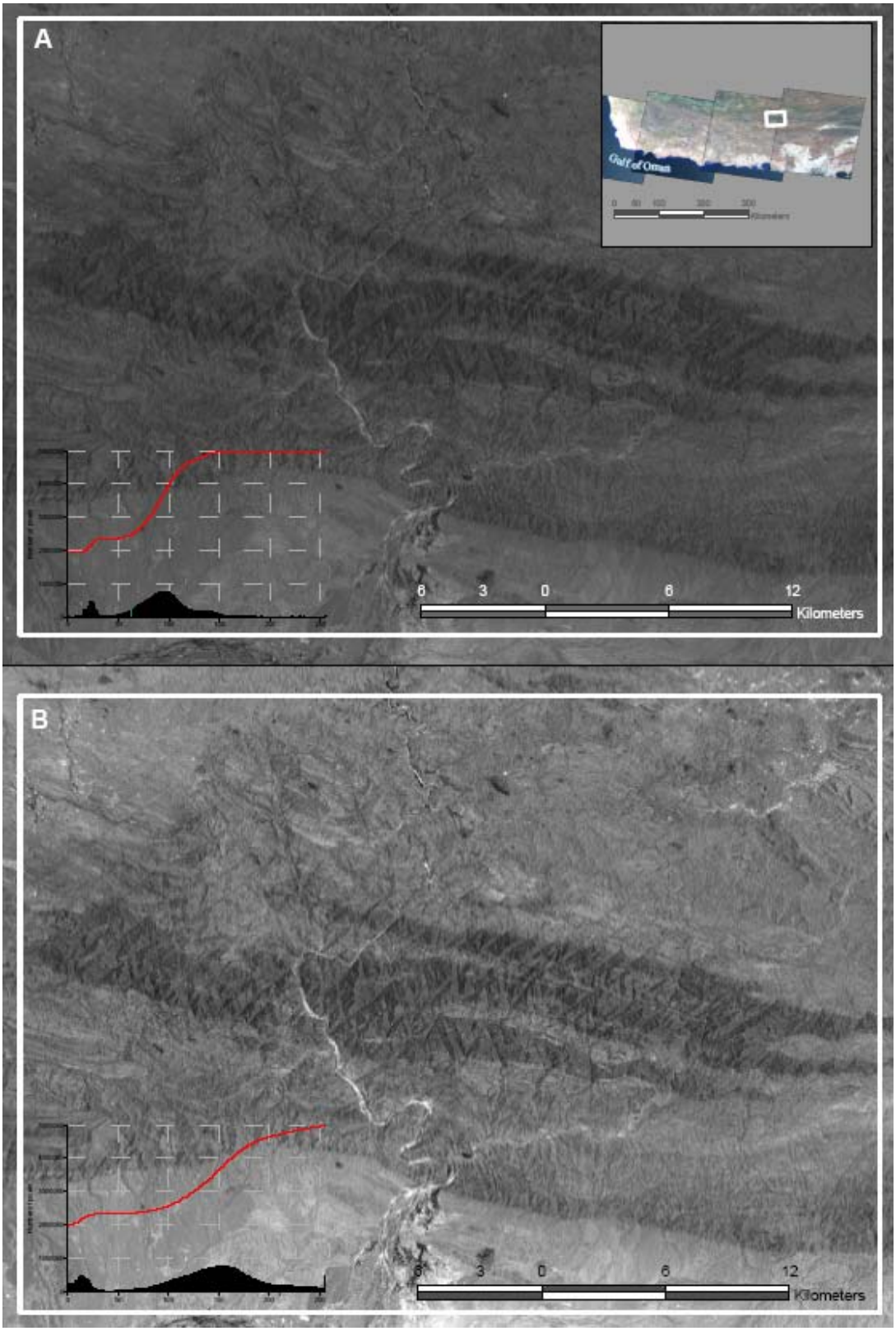

Figure 3.2: Linear stretching technique applied to Landsat ETM+ band 7 images. (A) Unstretched image. (B) Stretched image.

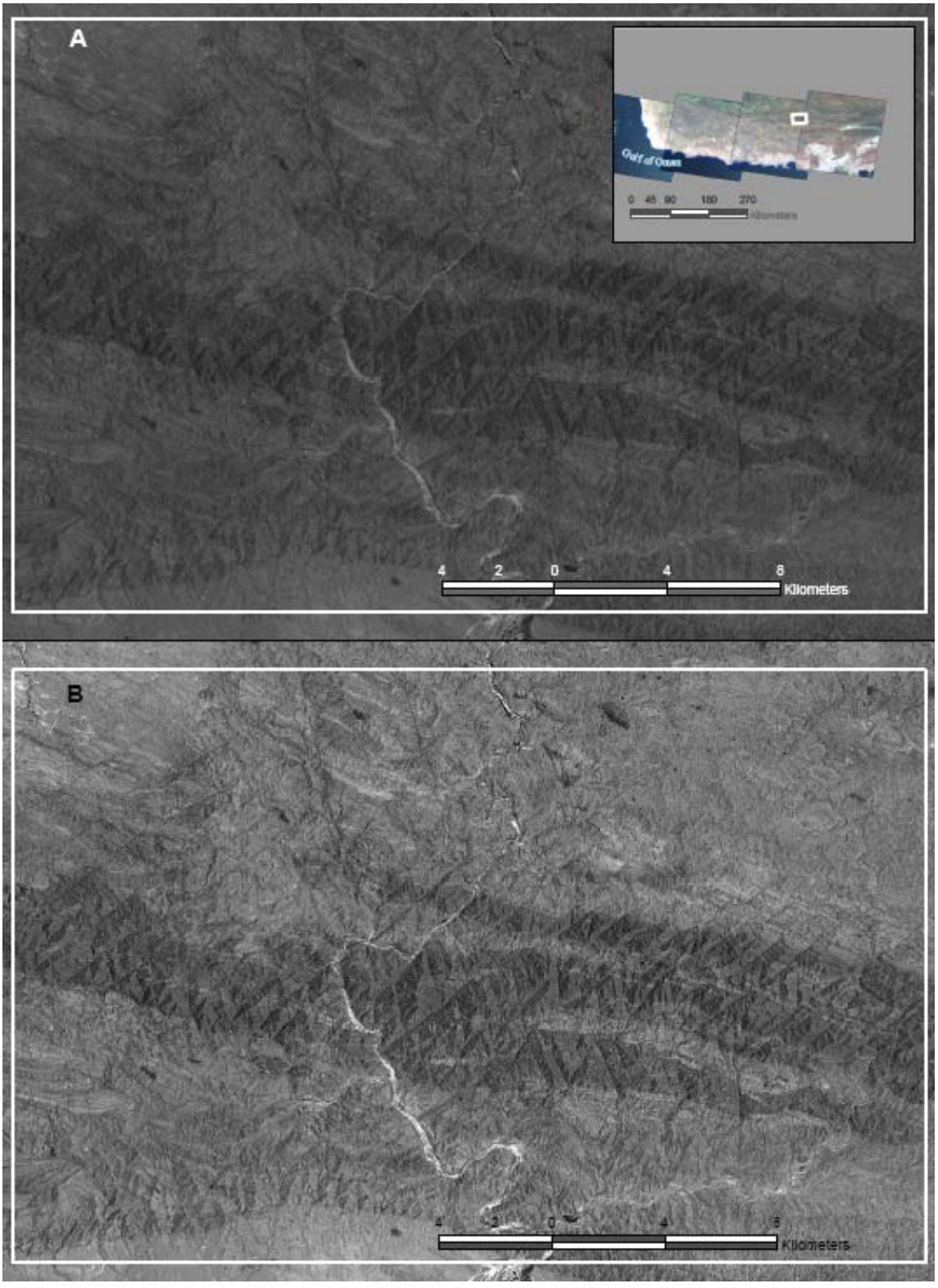

Figure 3.3: Edge Enhancement filter applied to Landsat ETM+ band 7 images where the filtered image looks more sharper than the unfiltered one. (A) Before filtering. (B) After filtering.

3.4 Spectral enhancement

Spectral enhancement technique requires more than one spectral band, and involves data compression in order to reduce redundancy, extraction of new visually interpretable bands, and displaying a wider variety of information by creating different color composites (Leica Geosystems, 1999, p.163). I applied the principal component analysis (PCA) and color composite (CC) as multi band spectral enhancement techniques.

3.4.1 Principle component analysis

Principal component analysis (PCA) is a multispectral image enhancement technique used to compress data in order to reduce redundancy by reducing spectral dimensions of the data (Gonzalez and Woods, 1993; Jensen, 1996; Leica Geosystems, 1999, p.164; ITC, 2001, p.254). PCA transforms a set of bands in such a way that the output bands, called principal components, are not correlated with one another, and each component carries new spectral information and become more interpretable than the source data. PCA rotates the axis of spectral space by changing the spectral coordinate of the pixel. The new axes are parallel to the axes of the ellipse as shown in Figure 3.4.

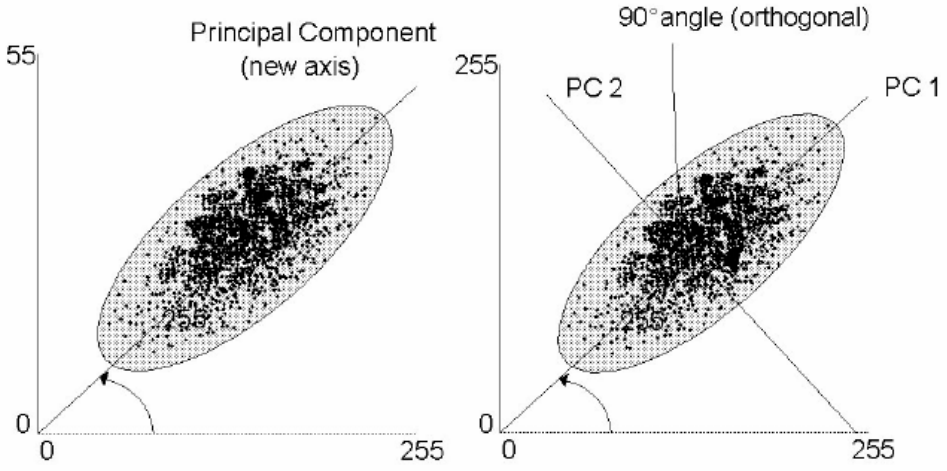

Figure 3.4: First and second principal components (PCs). [Source: ITC, 2001, ILWIS user's guide, p. 254]

In this study, PCA was done using six Landsat ETM+ bands (bands 1, 2, 3, 4, 5 and 7) as listed in Table 3.1. Bands 6 (thermal) and 8 (panchromatic) were not used in the study. The length and direction of the widest transect of the ellipse were calculated. The transect that corresponds to the major axis of the ellipse is called the first principal component (PC1), and the one orthogonal to the PC1 is called the second principal component (PC2) in two dimensional spectral space as shown in Figure 3.4. The directions of the PCs are the eigenvectors, and their lengths are the eigenvalues (Taylor, 1977; Faust, 1989). Since the numbers of both input and output bands of the analysis were six in this study, six different spectral dimensions were derived. The principal component matrix (covariance matrix) with calculated eigenvectors and the percentage of variance contributed by each eigenvalue for all the six dimensions are shown in Table 3.5. The first three PC images (PC 1, 2 and 3) contain more than 99% of the variation of the original six ETM+ bands, which is a significant compression of data (Table 3.5).

The output raster maps also known as principal components are listed in decreasing order of variance, and the first few components carry most of the spectral information while the others show noise in the data (Leica Geosystems, 1999; ITC, 2001). I used the first three PCs to create RGB color composite, in which PC1 was used in red and PC2 and PC3 were used in green and blue, respectively. The output false color composite image is shown in Figure 3.5, which combine different spectral information uncorrelated with other components. A standard color composite (CC) image contains only 73% of the available image variance, whereas the false color composite (FCC) calculated by combining the first three PC images contains 97% of the available image variance (Canas and Barnett, 1985).

Table 3.5: The principal component matrix with eigenvectors and percentage of variance contributed by each eigenvalue.

```
Variance per band:
27460.96   660.45    31.07    11.14     6.32     2.66
Variance percentages per band:
97.47    2.34    0.11    0.04    0.02    0.01
```

	tm1	tm2	tm3	tm4	tm5	tm7
PC 1	0.396	0.392	0.453	0.220	0.486	0.446
PC 2	0.708	0.311	0.053	-0.049	-0.447	-0.444
PC 3	0.418	-0.112	-0.637	-0.363	0.028	0.523
PC 4	0.360	-0.564	-0.171	0.395	0.481	-0.369
PC 5	0.149	-0.521	0.327	0.333	-0.551	0.429
PC 6	0.125	-0.384	0.499	-0.742	0.168	-0.098

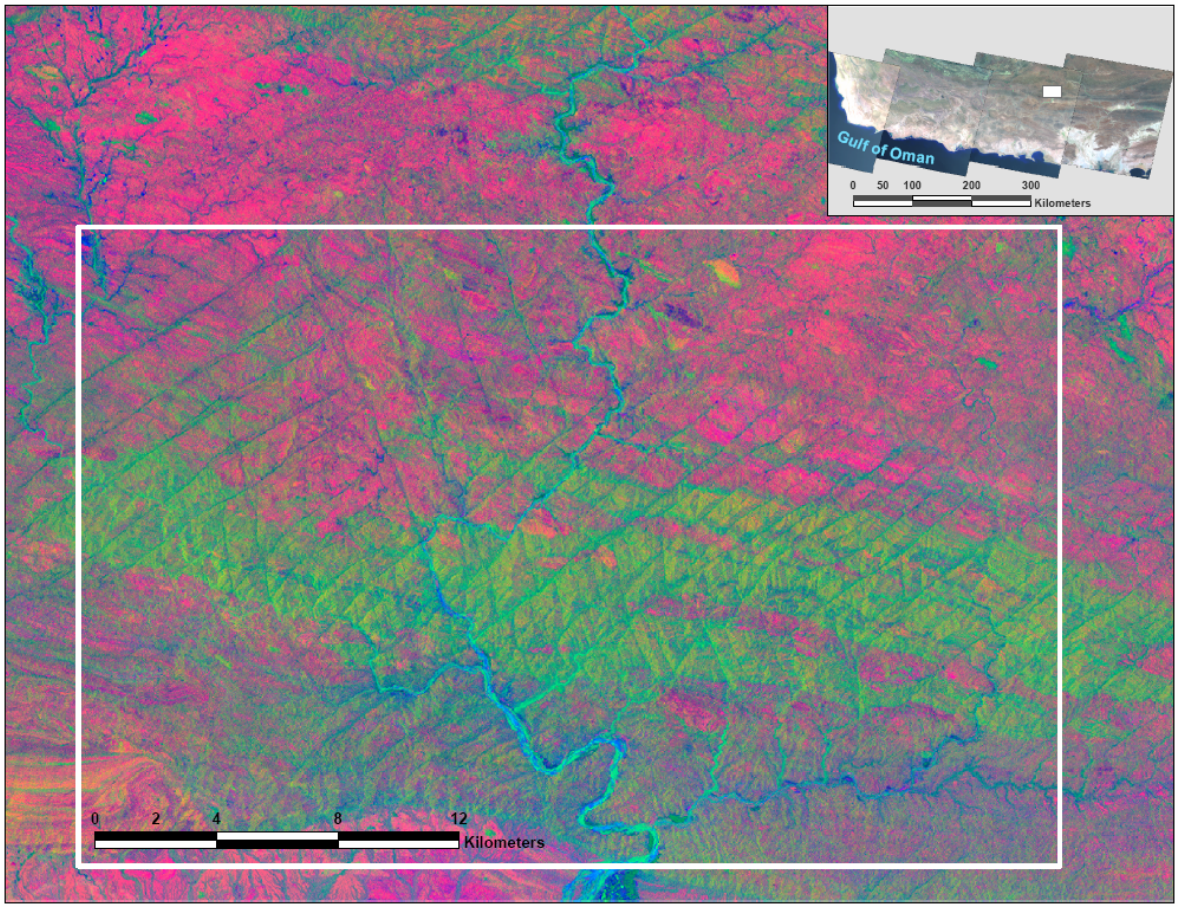

Figure 3.5: Color composite map created by combining the first three Principal Components, which contains about 97% of the available image variance (Canas and Barnett, 1985).

3.4.2 Color composite

Color composite is another multi-band spectral technique which was applied in the study to enhance the images digitally. Color composites are one of the most basic forms of images that are used for first-order analysis of remotely sensed data (Mustard and Sunshine, 1999). Spectral data stored in separate bands are integrated by combining them into one band, so that strong spectral anomaly is displayed and the image becomes more interpretable (Zumsprekel and Prinz, 2000; ITC, 2001).

Color composites are created by combining three raster images (bands). One band is displayed in shades of red and other two are displayed in shades of green and blue respectively. Statistical analysis of all digital numbers (DN) of the ETM+ bands was done to derive the correlation matrix and to determine the correlation coefficients of all the 6 ETM+ bands which characterize the distribution of pixel values in two raster maps (Leica Geosystems, 1999; ITC, 2001). The values for the correlation coefficient were derived by calculating a 6x6 correlation matrix (Table 3.6) that ranges from -1 to +1, where, +1 indicates a direct relationship between the two given bands, whereas -1 indicates an inverse relationship between the bands (Leica Geosystems, 1999; ITC, 2001).

Table 3.6: Correlation matrix showing the correlation between all the ETM+ image pairs with the mean and standard deviation for each input band.

	TM1	**TM2**	**TM3**	**TM4**	**TM5**	**TM7**
TM1	1.00	0.99	0.98	0.96	0.94	0.93
TM2	0.99	1.00	0.99	0.98	0.97	0.96
TM3	0.98	0.99	1.00	1.00	0.99	0.98
TM4	0.96	0.98	1.00	1.00	0.99	0.99
TM5	0.94	0.97	0.99	0.99	1.00	1.00
TM7	0.93	0.96	0.98	0.99	1.00	1.00
Mean per band	59.01	54.66	61.41	43.75	60.33	53.25
Standard deviation per band	49.24	46.80	53.72	38.61	55.76	49.33

In addition to the correlation coefficient matrix, I also calculated the optimum index factors (OIF) to determine the optimum band combinations of all the six bands (Table 3.7). OIF is the combinations of three input maps with largest sum of standard deviations and smallest correlations which gives an idea of which bands to use to create the color combinations (ITC, 2001). OIF can be used to rank red, green and blue (RGB) combinations of bands based on the amount of correlation between bands and total variance within the individual band (Chavez et al., 1984).

Table 3.7: Statistical values showing the highest sum of standard deviation and least value of correlation.

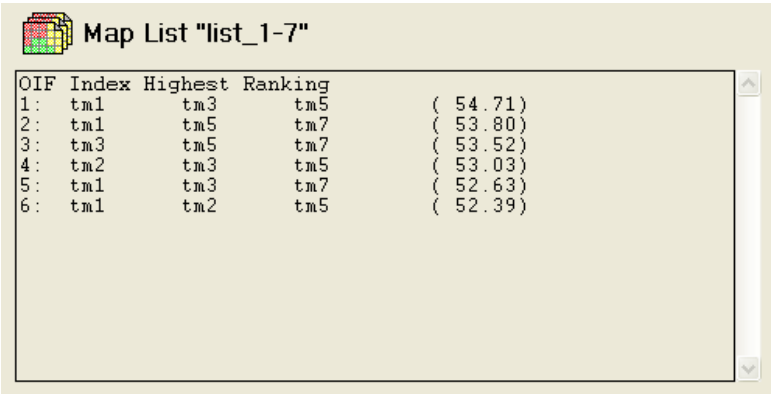

The OIF values suggest that from the 6 bands of the ETM+ images, the combination of bands 5, 3 and 1 (Figure 3.6) is the best statistical choice to create a color composite. In addition to the combination of 5, 3 and 1, combinations of bands 7, 5 and 1 (Figure 3.7) and bands 7, 4 and 2 (Figure 3.8) were also calculated by using the shades of red, green and blue respectively. Among these color combinations, the color composites created by combining bands 5, 3 and 1, and 7, 4 and 2, were found to be more useful on identifying the lineaments.

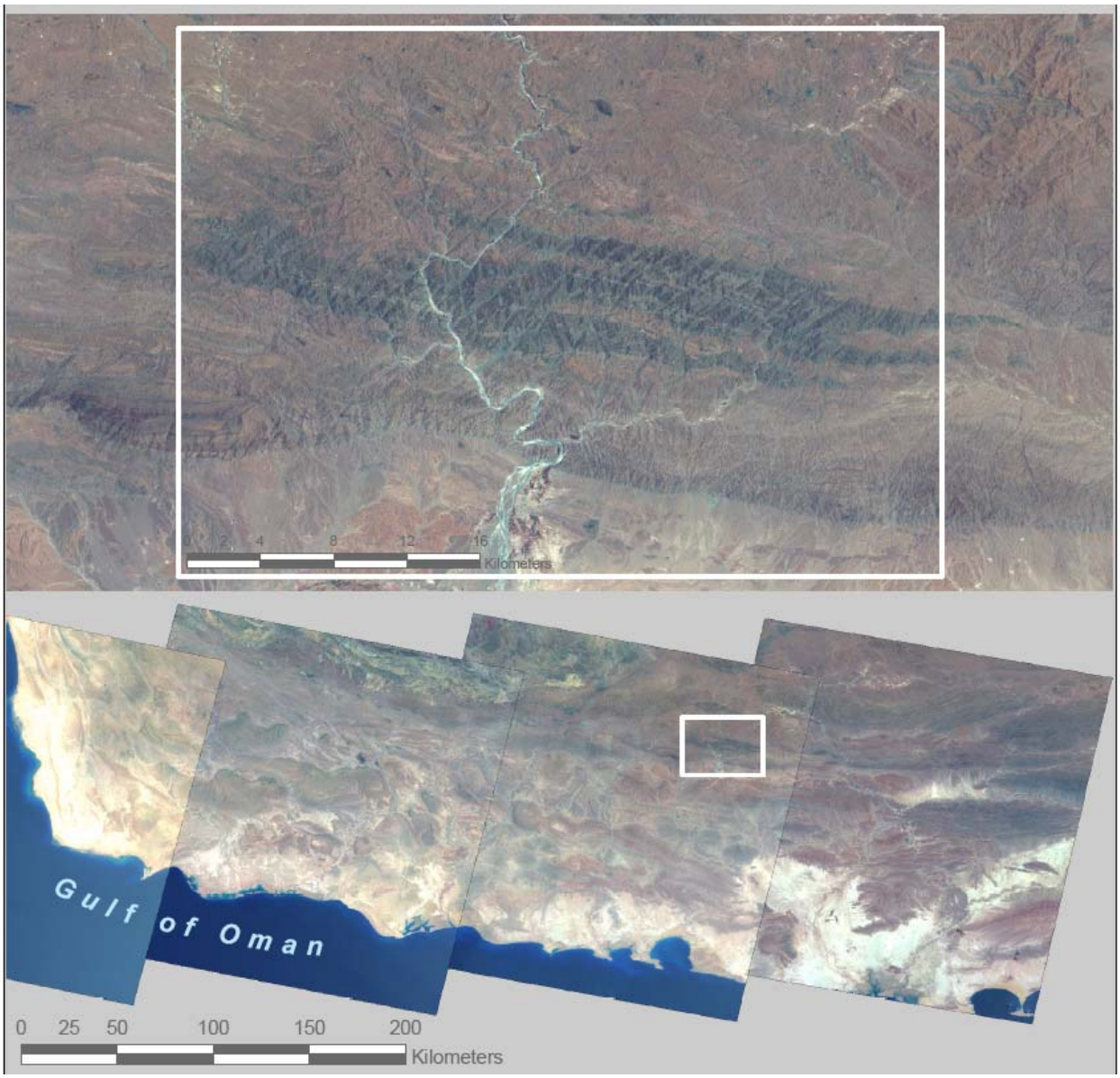

Figure 3.6: Color composite created by combining bands 5 (short wavelength infra-red), 3 (visible red) and 1(visible blue) as suggested by the OIF calculation shown in Table 3.8.

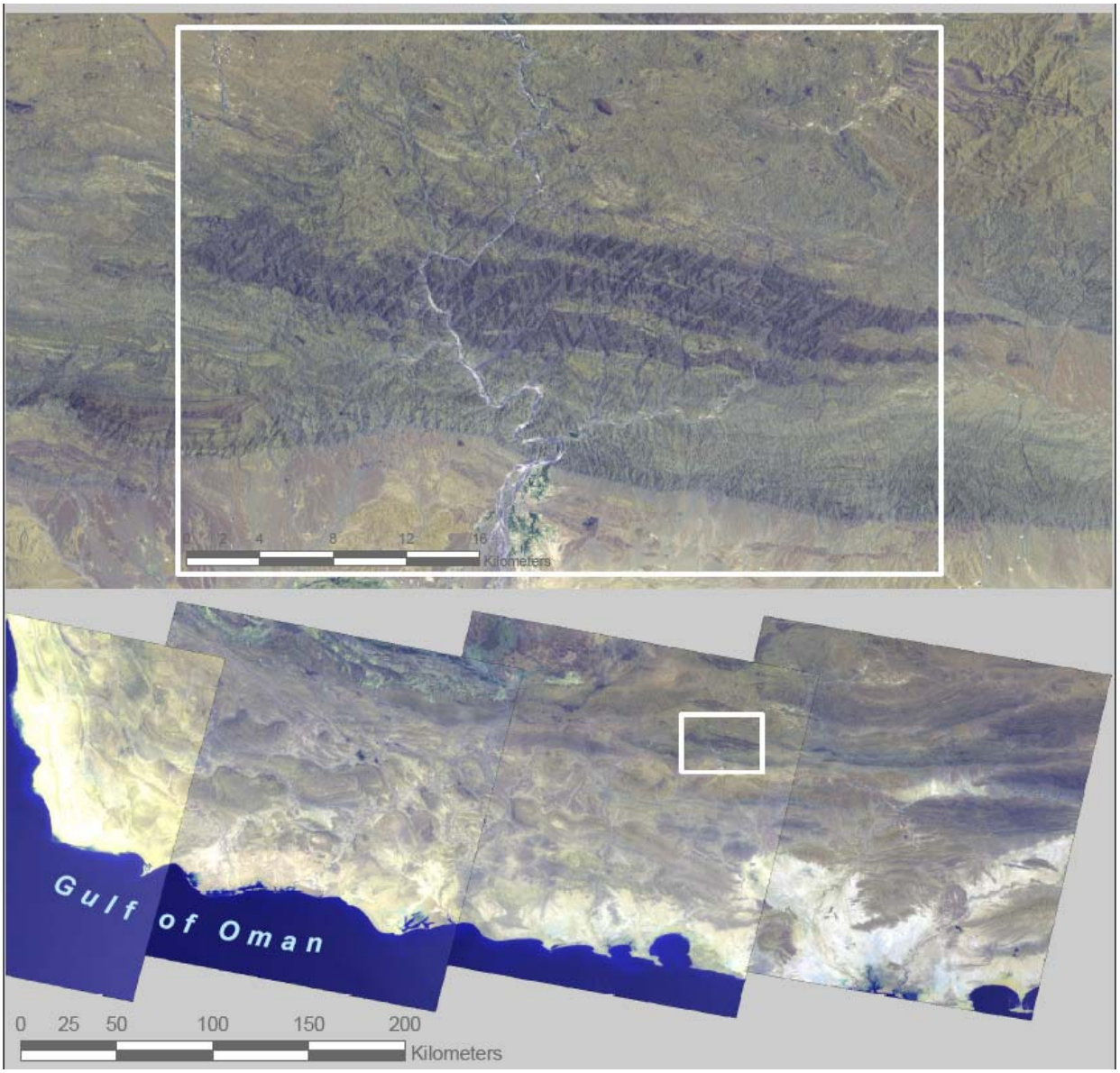

Figure 3.7: Color composite created by combining bands 7 (mid infra-red), 5 (short wavelength infra-red) and 1 (visible blue) as suggested by OIF calculation shown in Table 3.8.

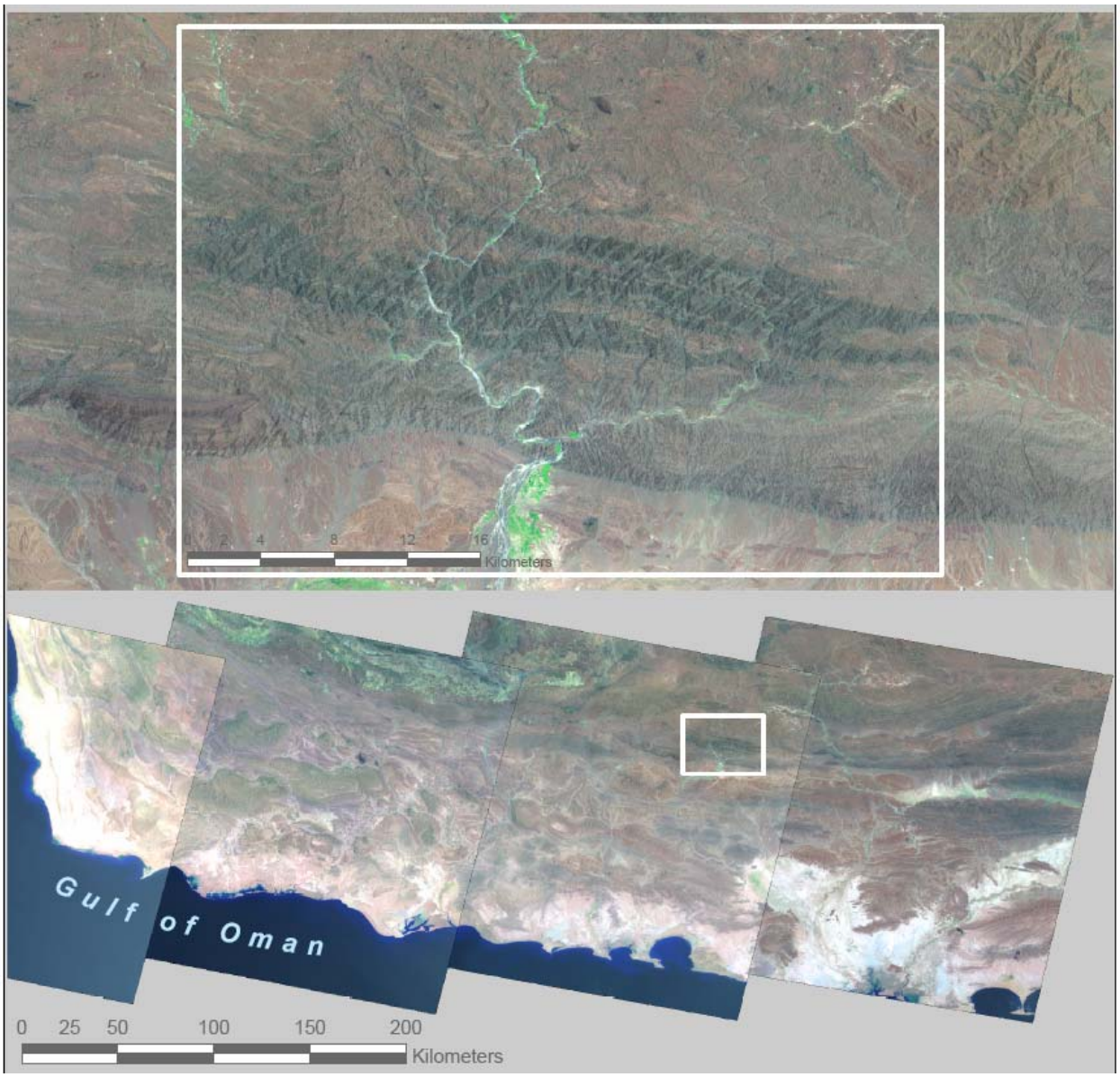

Figure 3.8: Color composite created by combining bands 7 (mid infra-red), 4 (infra-red) and 2 (visible green).

CHAPTER 4

4. Digitization and lineament characterization

Digitally processed scenes of the Landsat ETM+ imageries and the shaded relief map derived from SRTM DEM were used to map the lineaments in the study area. The traces of these lineaments were converted into digital vector format using ArcGIS 9.1 and ILWIS 3.3 software programs. Lineaments are simple or composite linear features which are aligned in a rectilinear or slightly curvilinear relationship and which differ from the adjacent features and presumably represent the subsurface phenomenon (O'Leary et al., 1976).

The lineaments were detected by analyzing photographic, geologic, and structural properties such as change in micro relief, change in topography, drainage pattern, and change in tones and textures due to different reflectance of the rocks and minerals. Fractures, E-W trending thrust faults, and E-W trending axial traces of the alternating anticlines and synclines were identified and digitized.

4.1 Lineaments

False color composites (FCCs) were created, from the study of the digitally processed images, including principal components (PCs), by combining Landsat ETM+ bands 7, 5, and 1; 7, 5 and 3, and 7, 4 and 2, and the shaded relief map derived from SRTM DEM. I recognized 17,049 lineaments. The spatial distribution of lineaments in relation to lithology in study area is shown in Figure 4.1. The distribution of lineament populations, their orientation, and distribution vary spatially, lithologically, and structurally throughout the study area. I used a domain-based quantification approach to treat and analyze these lineament populations separately. This was done by plotting the

trends and frequencies of the lineaments in rose diagrams (circular histograms displaying the number of lineaments against compass direction), and creating a lineament density maps for all the lineaments. First, I plotted a single rose diagram for the entire lineaments, which showed three main lineament populations trending NW-SE, N-S, and NE-SW directions (Figure 4.2). Then I separated the lineaments into three different classes based on their representative orientations, and created corresponding line density maps for each population (Figures 4.3). The lineament density maps show the spatial distribution and concentration of lineaments in kilometer per square kilometer (km/km^2) in a particular geographic location. I analyzed the relative density of each set of lineaments in order to compare the dominance of one set over others (Figure 4.3). The homogeneity was also evaluated visually and using the mean and standard deviation of the dominant modes (i.e., lineament sets). In addition to this, I also created several rose diagrams one for each lineament cluster (Figure 4.4). I merged the lineament populations with similar orientations in order to reduce the number of domains. I identified and separated the study area into 10 structural domains based on the homogeneity of the lineament orientations, length, frequency and their spatial distribution; these are shown in Figure 4.5.

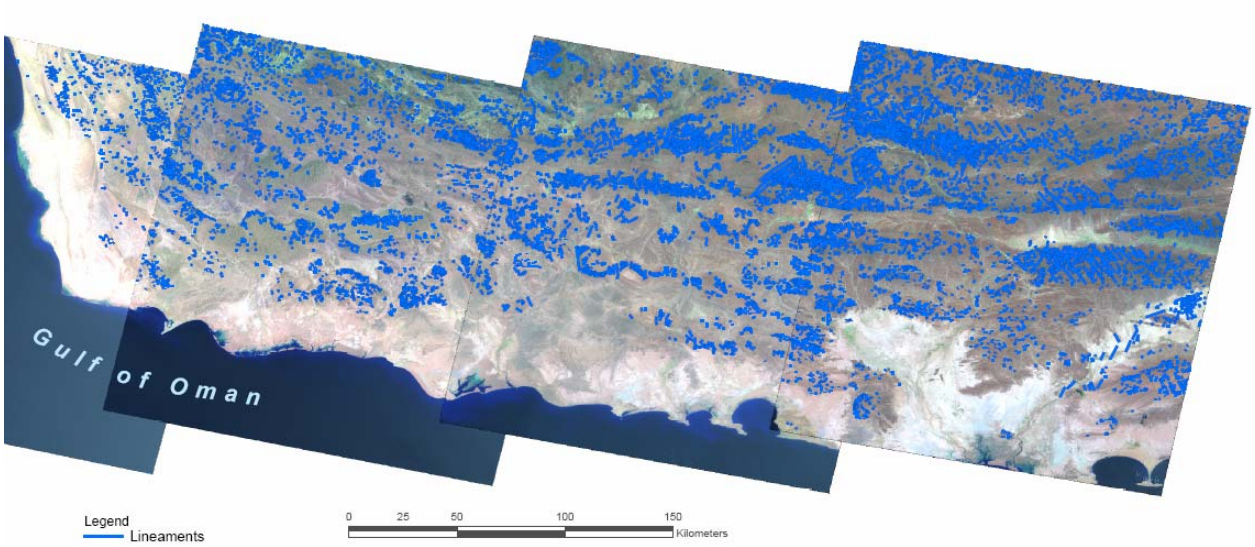

Figure 4.1: Spatial distribution of the lineaments in the study area.

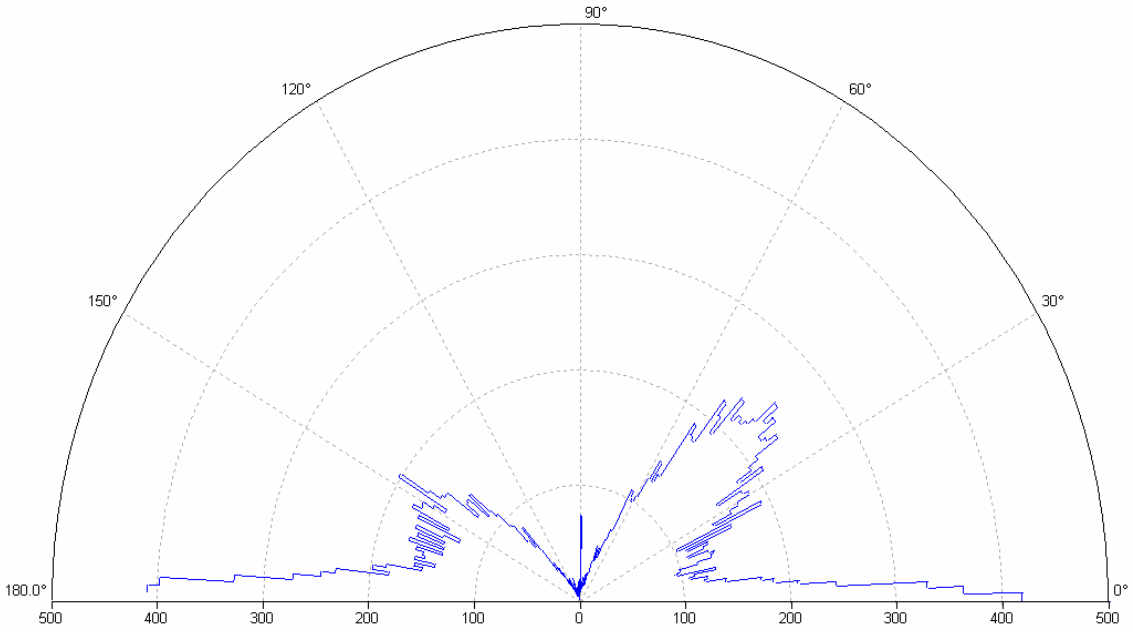

Figure 4.2: Rose diagram plot of all 17,049 lineaments showing three main lineament populations trending NE-SW, N-S and NW-SE directions.

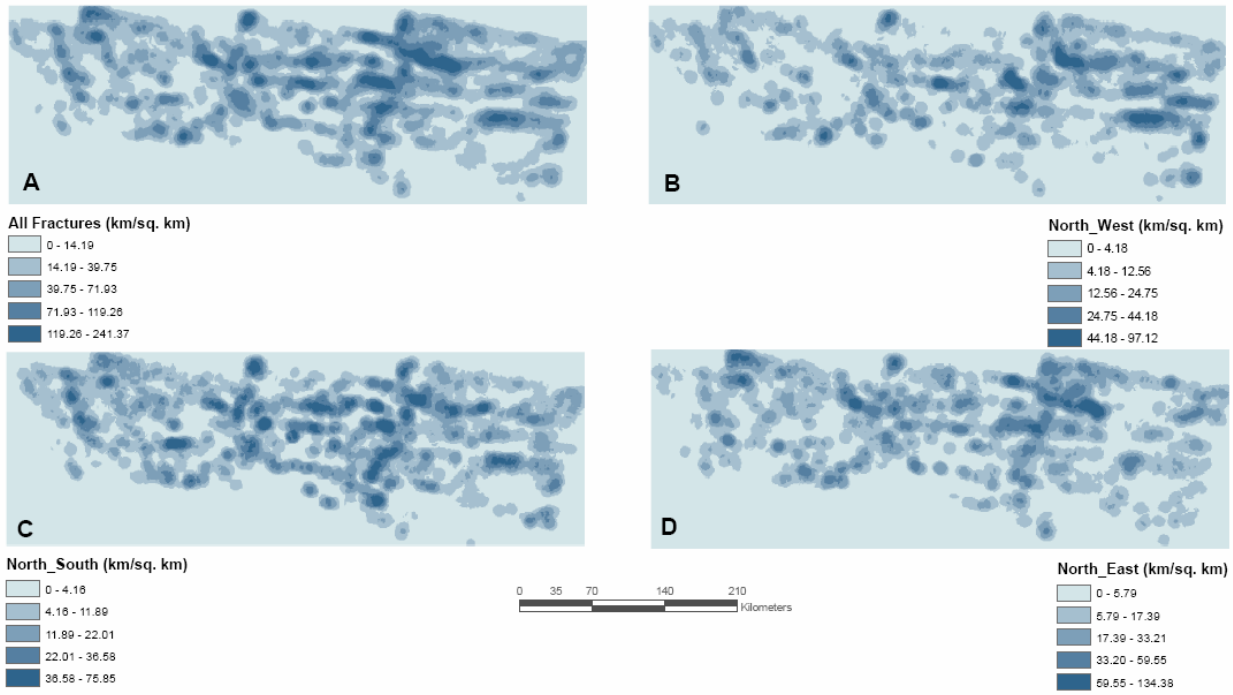

Figure 4.3: Lineament density maps measured in length of lineament per square km. (A) for all the lineaments, (B) NW oriented, (C) NS oriented, and (D) NE oriented.

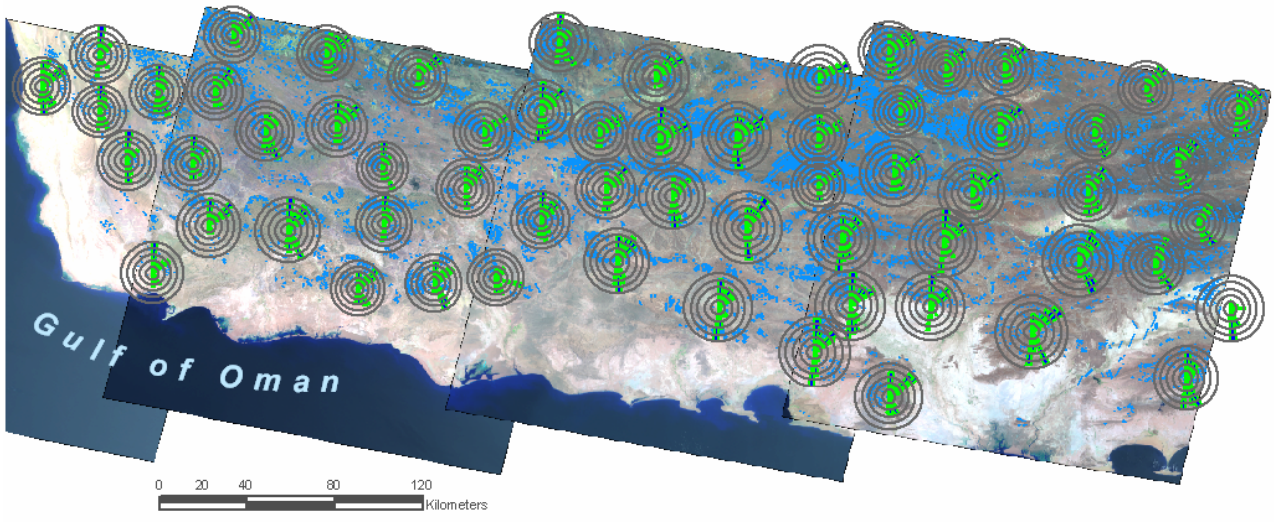

Figure 4.4: Rose diagrams showing the orientation of lineaments for each lineament cluster.

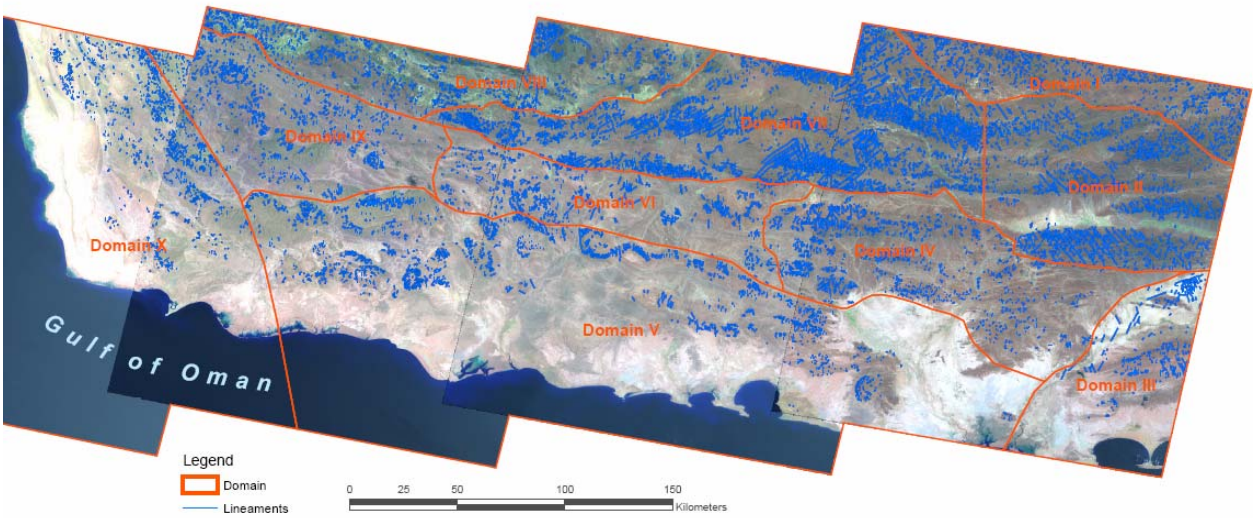

Figure 4.5: Structural domains separated based on homogeneity, spatial distribution, and orientation of the lineaments.

4.1.1 Domain I

Domain I is located in the northeastern part of the Makran accretionary prism. Geographically it also covers a small area in western Pakistan (Figure 2.1; Figure 4.5). Geologically it comprises sedimentary mélange with no recognizable stratigraphy, and tectonic blocks of the Cretaceous to Miocene time (Figure 2.2). Altogether 1,246 lineaments (7.3% of the total of 17,049) were digitized in domain I. The rose diagram and the histogram were prepared by plotting the number of lineaments against their orientation (compass direction). Figure 4.6 (A) and (B)) show three main sets of lineament populations based on their frequency in around a specific orientation. The first set has a total of 410 lineaments, between N25E and N42W, with the mean orientation at N39E, and a standard deviation of 8.2^{o}. The trend of second set ranges from N25W to N42W, with a total of 194 lineaments, and a mean orientation of N35W and a standard deviation of 4.6^{o}. A third set is ranges between N7W and N5E, with total of 188 lineaments, and a mean orientation of N2W and a standard deviation of 1.5^{o} (Table 4.1).

In addition to these three major sets, a fourth set (N10W-N25W) including 142 lineaments, has a mean orientation of N17W, and a standard deviation of 4.8^{o}. A fifth set (N9E-N22E) including 84 lineaments, has a mean orientation of N16E and a standard deviation of 3.6^{o}. The populations of the fourth and the fifth sets are significantly smaller than that of other sets. About 35 lineaments, with trends ranging from N70E to N50W, and a mean orientation of N80W and a standard deviation of 16.4^{o} were also found in this domain. As indicated by the high standard deviation, these lineaments are highly dispersed and are not considered as an individual set.

Table 4.1: Statistics of the three main sets of lineaments in domain I.

	Orientation	**No. of lineaments**	**Mean**	**Standard Deviation**
Set 1	N25E-N55E	410	N39E	8.2
Set 2	N25W-N42W	194	N35W	4.6
Set 3	N7W-N5E	188	N2W	1.5

The maximum and minimum lengths of the lineaments in domain I are 4.6 km and 144 m, respectively. The length of lineaments represented in the histogram (Figure 4.6 (B)) shows that they follow a log-normal distribution. The maximum frequency lies between 400 and 600 m, with most lineaments included in the interval between 300 to 700m. The number of lineaments on either side of this range of orientation falls rapidly. Even though the maximum length reaches 4.6 km, only very few lineaments are longer than 2.5 km.

A

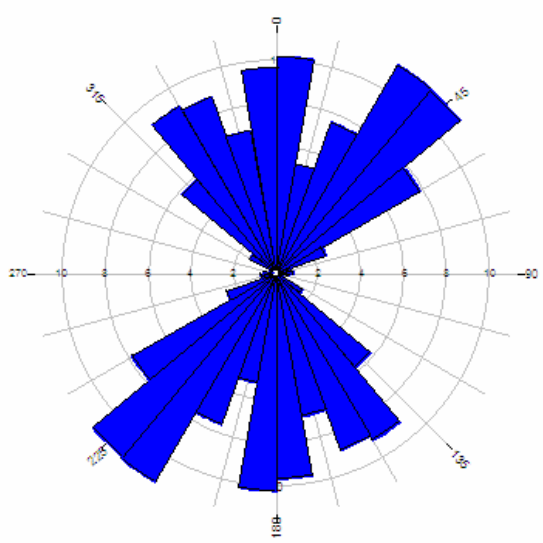

B

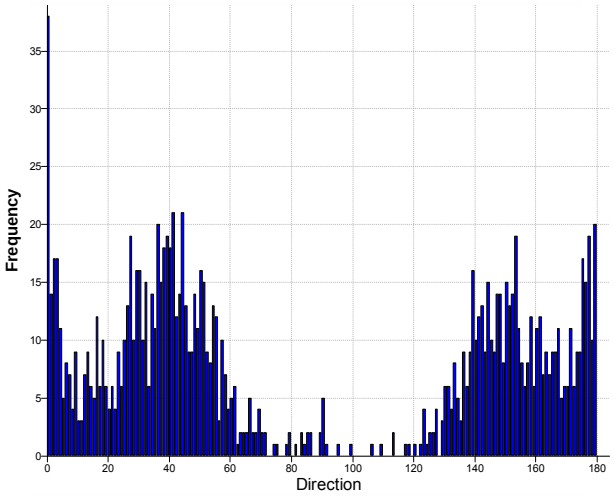

C

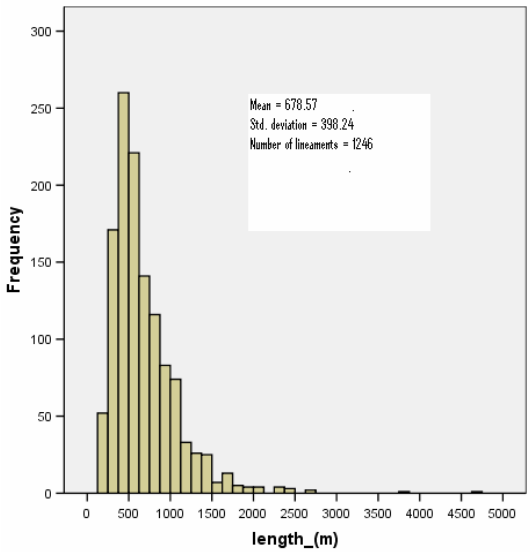

Figure 4.6: Plots of 1,246 lineaments in Domain I. (A) Rose diagram of the lineaments orientation. (B) Frequency of orientation against number of lineaments, and (C) Frequency of length against the number of lineaments.

4.1.2 Domain II

Domain II is situated in the eastern part of the study area (Figure 4.5). Altogether 1,724 lineaments (about 10% of the total of 17,049) were mapped in this domain. More than 59% of the total lineaments (i.e., 1,015) are in Pakistan. Geologically, the upper part of the domain comprises sedimentary mélange with sheared and boudinaged sediments with no recognizable stratigraphy, and tectonic blocks of the Cretaceous to Miocene age (Figure 2.2). The upper and lower part of the domain also consists of Oligocene and Miocene flysch, whereas the middle part of the domain is comprised of Neogene and Miocene red beds (NIOC, 1977) and valley terrace deposits (Figure 2.2).

Three dominant sets of lineament populations occur in this domain (Figure 4.7 (A) and (B)). The first set has 533 lineaments, with orientation ranging between N20W and N50W, with a mean oriented N45W, and a standard deviation of 7.6^{o} (Table 4.2). The second set has trends between N17E and N53E. Altogether, there are 471 lineaments in the second set, with a mean oriented N32E, and a standard deviation of 10^{o}. The third set has 371 lineaments, and trends between N10W and N7E, with a mean oriented N2W, and a standard deviation of 2.3^{o}. In addition to these three major sets of lineament, there is a fourth set oriented N10W-N20W, with a mean orientted N25W, and a standard deviation of 3^{o}. There are about 103 lineaments between N55E and S50E with a mean around 090 (i.e., E-W) and a standard deviation of 29.5^{o}. Since the standard deviation is significantly high, the lineaments are highly dispersed. For this reason, these lineaments are not classified as a set. However, these fractures may have some structural significance, which I will discuss in the subsequent chapter.

A

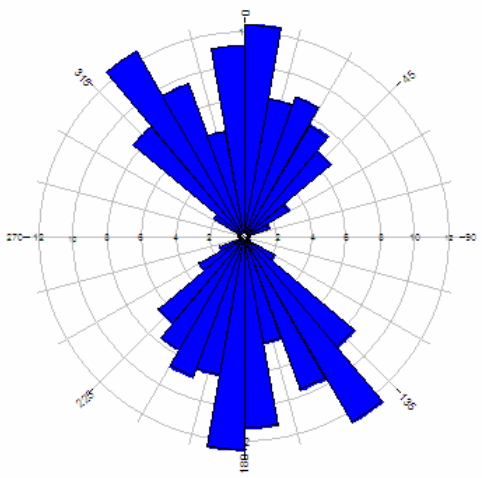

B

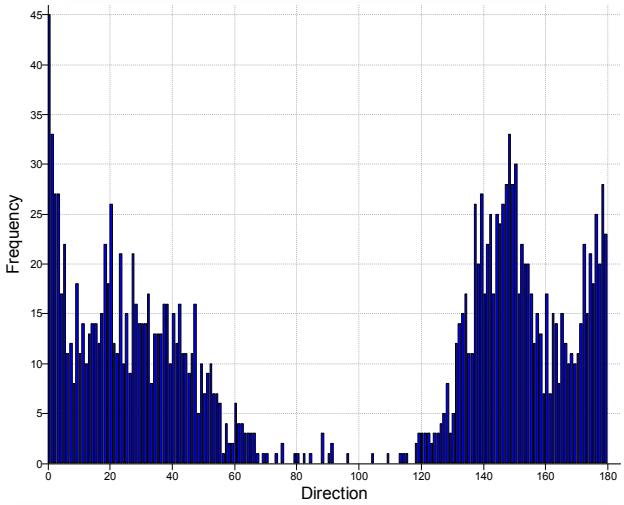

C

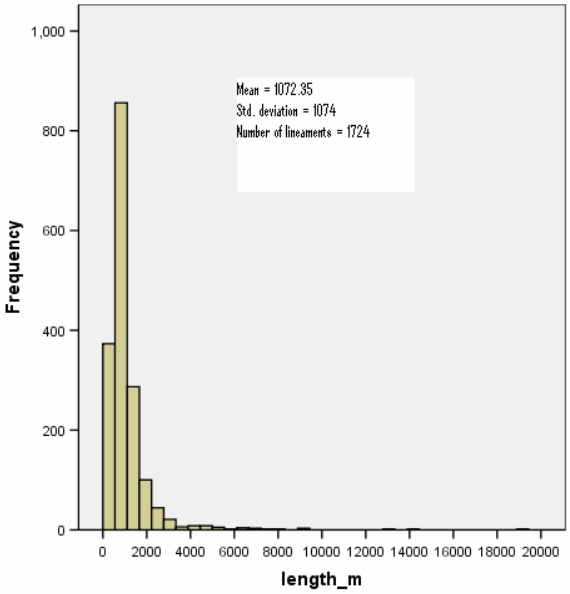

Figure 4.7: Plots of 1,724 lineaments in Domain II. (A) Rose diagram showing the orientation frequency of the lineaments, (B) Histogram showing frequency of the lineament orientation, and (C) Histogram showing length against orientation of the lineaments.

Table 4.2: Statistics of the three main sets of lineaments in domain II.

	Orientation	No. of lineaments	Mean	Standard Deviation
Set 1	N20W-N50W	533	N45W	7.6
Set 2	N17E-N53E	471	N32E	10
Set 3	N10W-N7E	371	N2W	2.3

The minimum and the maximum lengths of the lineaments in domain II are 160 m and 19.1 km, respectively. The length of the lineaments plotted against the frequency shows a log-normal distribution (Figure 4.7). The 500 m and 1000 m long fractures are the most frequent, with a mode between 300 m to 1,500 m. The number falls rapidly on the either side of this range. Even though the maximum length reaches up to more than 19 km, only a very few lineaments are longer than 3 km.

4.1.3 Domain III

Domain III is situated in the southeastern corner of the study area (Figure 4.5). Geographically, this domain lies in Pakistan. Geologically, the upper and lower part of the domain is cover by low level piedmont fan and valley terrace deposits. The middle part is comprised of marl and marlstone with locally gypsiferous sandstone and interbedded shale (Figure 2.2). Altogether 344 (2% of the total of 17,049) lineaments are detected and digitized in this domain. This is the smallest domain in the study area in terms of areal extent and number of lineaments identified.

The rose diagram and histogram plotted in terms of frequency against orientation show three dominant sets of lineament population (Figure 4.8 (A) and (B); Table 4.3). The First set (80 lineaments) is oriented between N18W and N40W, and a mean orientated N28W, and a standard deviation of 6.02^{o}, The second set (78 lineaments) oriented between N20E and N50E, has a mean orientation of N34E, and a standard

deviation of 8.59^{o}. The third set (65 lineaments) is oriented between N5E and N7W, and has a mean oriented along N1W, and a standard deviation of 1.59^{o}. In addition to these three major sets of lineament populations, there is a fourth set (36 lineaments) with individual lineaments oriented between N8W and N18W, a mean along N12W, and a standard deviation of 3.24^{o}. There are also about 10 lineaments in almost E-W direction.

Table 4.3: Statistics of the three main sets of lineament in domain III.

	Orientation	**No. of lineaments**	**Mean**	**Standard Deviation**
Set 1	N18W-N40W	80	N28W	6.02
Set 2	N20E-N50E	78	N34E	8.59
Set 3	N7W-N5E	65	N1W	1.59

The minimum and the maximum length of the lineaments in domain III are 189 m and 9.3 km, respectively. The distribution of the length of these lineaments is log-normal (Figure 4.8 (C)). The maximum length lies between 500 m and 1,000 m, and most lineaments have lengths between 200 m and 1,500 m. The numbers of lineaments on either side of this range fall rapidly. Even though the maximum length is 9.3 km, only very few lineaments are longer than 4 km.

A

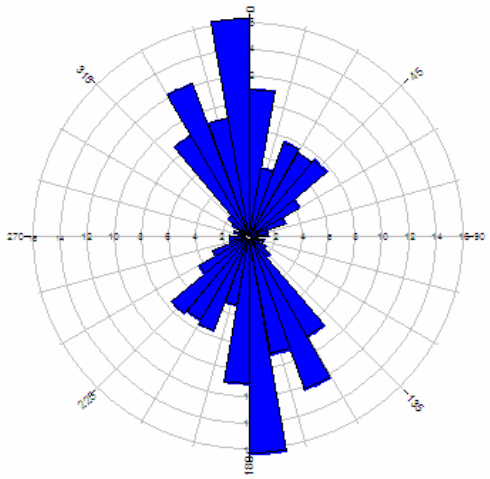

B

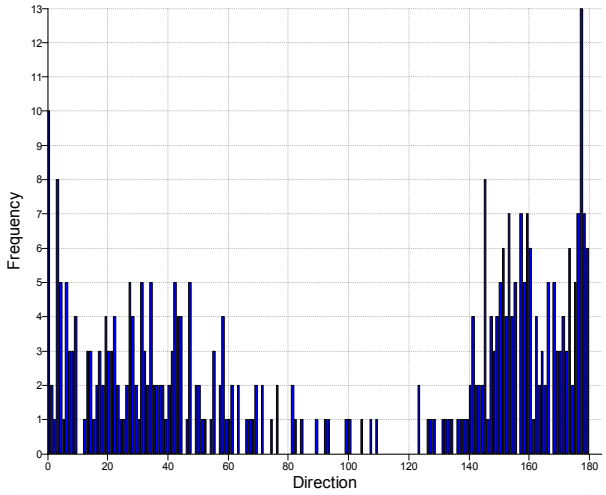

C

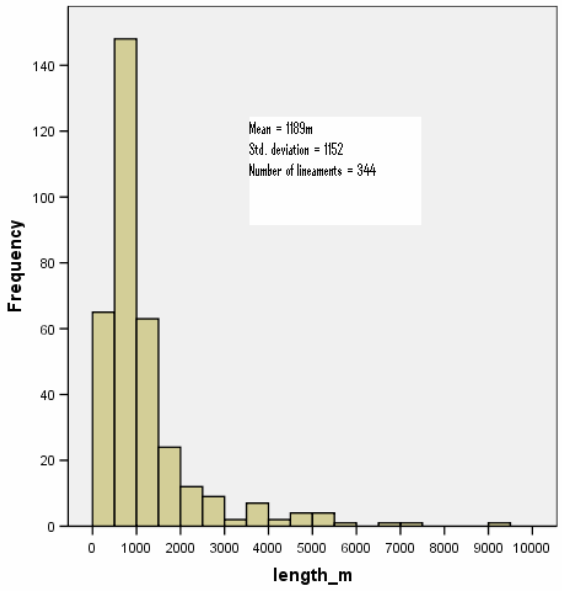

Figure 4.8: Plots of 344 lineaments in Domain III. (a) Rose diagram showing lineaments frequency against orientation. (b) Histogram plot of lineament frequency against orientation. (c) Length of the lineaments against frequency.

4.1.4 Domain IV

Domain IV is situated to the north of the Bahu Kalat Kor River in the southeastern boarder of Iran (Figure 4.5). This domain consists of 1,666 (i.e., 9.7% of the total of 17,049) lineaments. Geologically, this domain is comprised of three main types of deposits. The northern part of the domain consists of undifferentiated Paleogene flysch (NIOC, 1977) with sedimentary mélange containing tectonic blocks of Cretaceous to Miocene age. The middle part of the domain is characterized by rhythmically bedded sandstone and shale with minor siltstone and mudstone (Figure 2.2). The southern part of the domain has some gypsiferous and calcareous marl interbedded with siltstone and sandstone (Figure 2.2).

Three main sets of lineament occur in this domain (Figure 4.9 (A) and (B); Table 4.4). The first set (601 lineaments), oriented between N15E and N60E, has a mean orientation of N38E, and a standard deviation of 10.7^{o}. The second set (529 lineaments) is oriented between N8W and N10E, and has a N-S mean orientation and a standard deviation of 2.43^{o}. The third set (197 lineaments) oriented between N37W and N20W has a mean orientation of N30W and a standard deviation of 4.49^{o}. In addition to these three major sets of lineaments, there is a fourth set (135 lineaments) between N20W and N8W with a mean oriented along N14W and a standard deviation of 3.35^{o}. About 75 lineaments are also identified between N40W and N55W, with mean oriented N44W and a standard deviation of 3.75^{o}.

Table 4.4.: Statistics of the three main sets of lineaments in domain IV.

	Orientation	**No. of lineaments**	**Mean**	**Standard Deviation**
Set 1	N15E-N60E	601	N38W	10.7
Set 2	N8E-N10E	529	N-S	2.43
Set 3	N37W-N20W	197	N30W	4.49

A

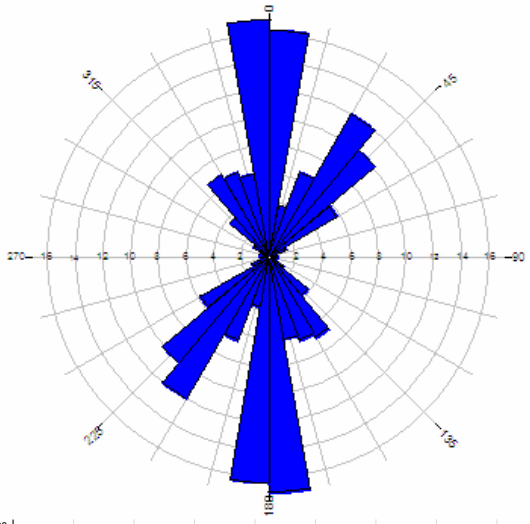

B

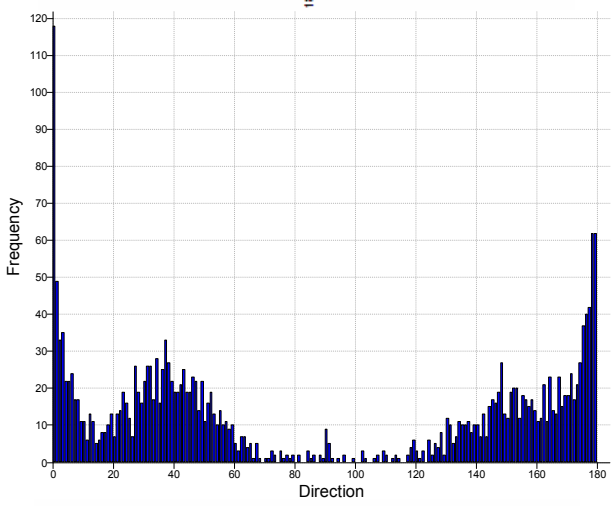

C

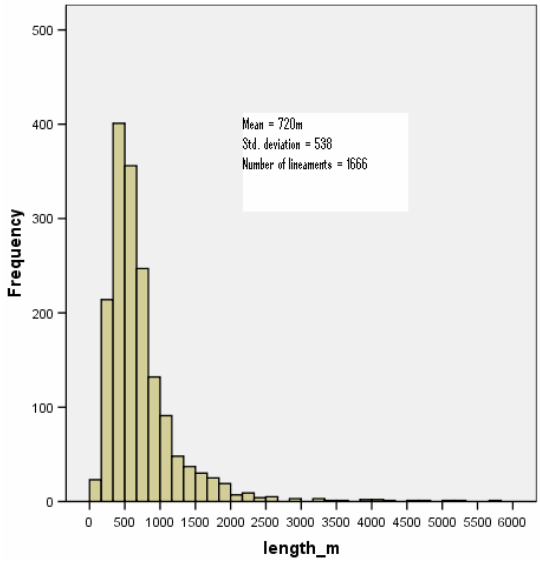

Figure 4.9: Plots of 1,666 lineaments in Domain IV. (A) Rose diagram showing lineaments frequency against orientation. (B) Histogram plot of lineament frequency against orientation. (C) Length of the lineaments against frequency.

The minimum and maximum lengths of the lineaments in the domain IV are 36 m to 5.7 km, respectively. The length of the lineaments in this domain shows a log-normal distribution (Figure 4.9 (C)). The maximum frequency lies between 300 and 500 m, and most of the lineaments are within the range of 300 to 700 m. The number of lineaments on either side of this range falls rapidly. The longest lineament is more than 5.7 km long, but only a few are longer than 2 km.

4.1.5 Domain V

Domain V is located in the mid-southern part of the study area (Figure 4.5). It is bounded by sedimentary mélange to the north, and swamps and marshland north of Gulf of Oman (Figure 2.2). The domain consists of a number of E-W trending anticlinal and synclinal folds and fold related thrusts. Geologically, this domain can be divided into three main categories. The northern part is mainly comprised of Lower Miocene deposits, Neogene clastics, Paleocene conglomerate, and some Miocene red beds (Figure 2.2). The middle part consists of sedimentary mélange and rhythmically bedded sandstone and shale with some siltstone and conglomerate. The southern part of the domain is cover by piedmont fan and valley terrace deposits, which is followed by swamps and marshes. Altogether 2,330 lineaments (13.6% of the total of 17,049) are identified, most of which are mapped on the limbs of the folds in the northern and middle part of the domain (Paleocene to Miocene deposits). No lineaments are identified in the satellite images in the southern part of the domain since terrace deposits, swamps and marshes cover it.

Three main sets of lineament occur in this domain (Figure 4.10 (A) and (B); Table 4.5). The first set has 778 lineaments oriented between N10W and N10E, with a mean orientation along N1W, and a standard deviation of 2.72^{o}. The second set consists of 711

lineaments oriented between N25E and N60E, with a mean orientation of N41E, and a standard deviation of 8.9^{o}. The third set has 314 lineaments oriented between N27W and N47W, with a mean orientation of N36W and a standard deviation of 5.12^{o}. In addition to these three main sets of lineaments, a fourth set of 245 lineaments is oriented between N8W and N26W, and has a mean of N16W and a standard deviation of 5.43^{o}. A fifth set of 188 lineaments has a mean along N16E and a standard deviation of 4.12^{o}.

Table 4.5: Statistics of the three main sets of lineaments in domain V.

	Orientation	**No. of lineaments**	**Mean**	**Standard Deviation**
Set 1	N10W-N10E	778	N1W	2.72
Set 2	N25E-N60E	711	N41E	8.9
Set 3	N27E-N47W	314	N36W	5.12

The shortest and longest lineaments in domain V are 44 m and 10.2 km long, respectively. The length of these lineaments shows a log-normal distribution (Figure: 4.10 (C)). The maximum frequency lies between 200 and 800 m, with most lineaments lying in the interval between 100 and 1,000 m. The number of lineaments on either side of this range falls rapidly. Although the longest lineament in the domain is greater than 10 km, only a few are longer than 350 m.

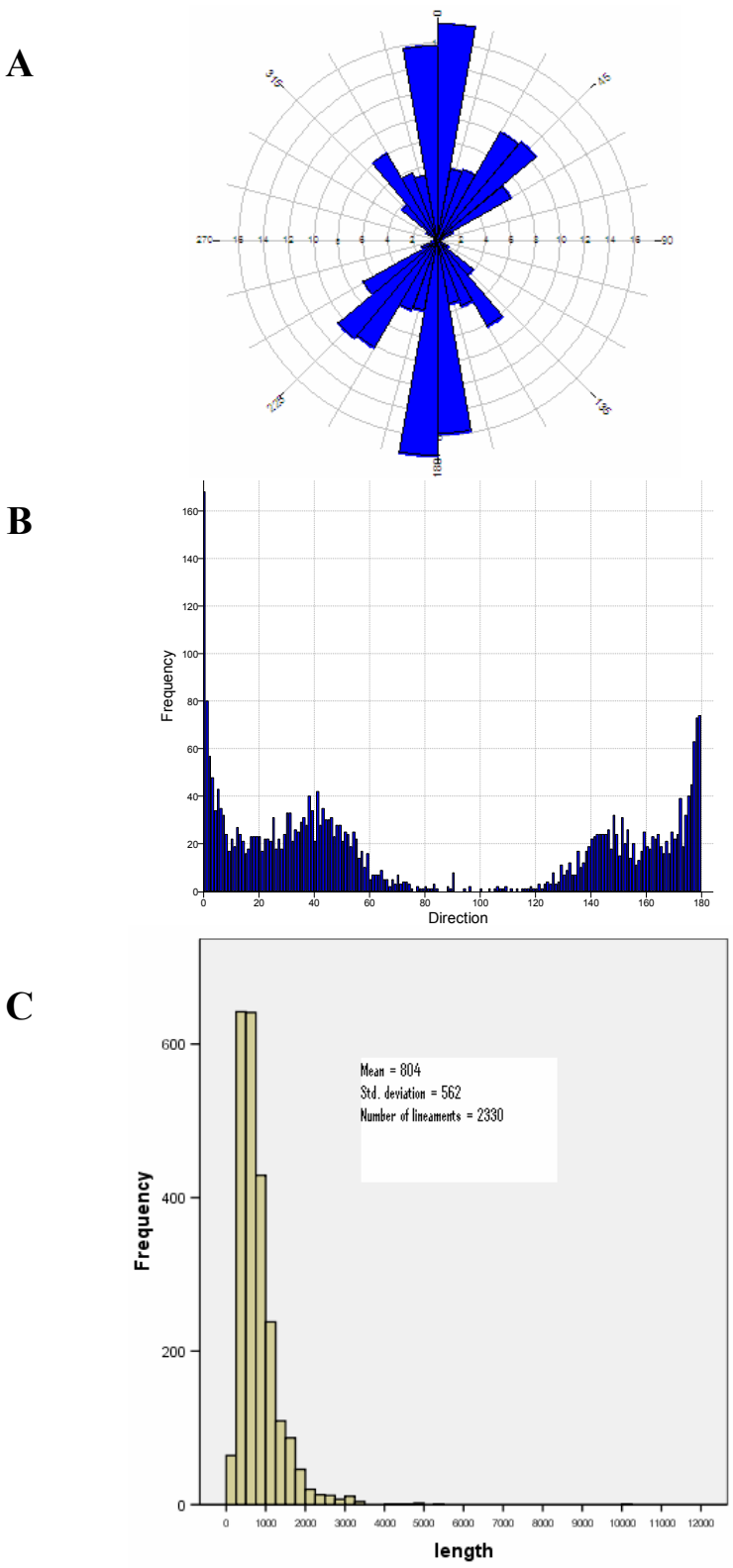

Figure 4.10: Plots of 2,330 lineaments in Domain V. (A) Rose diagram showing lineaments frequency against orientation. (B) Histogram plot of lineament frequency against orientation. (C) Length of the lineaments against frequency.

A

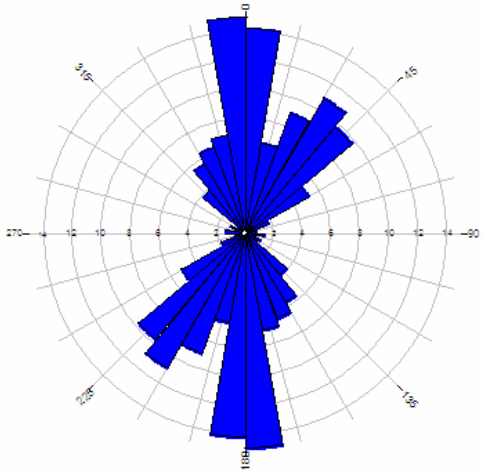

B

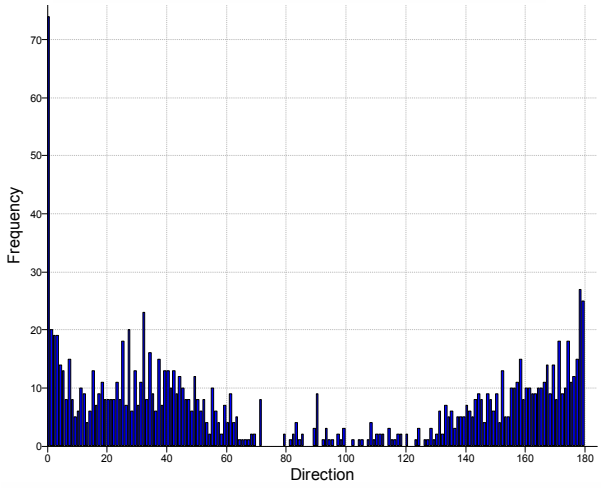

C

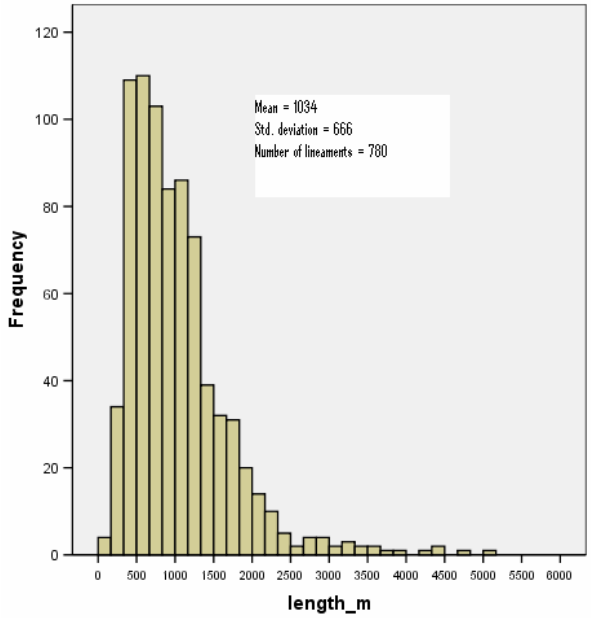

Figure 4.11: Plots of 780 lineaments in Domain VI. (a) Rose diagram showing lineaments frequency against orientation. (b) Histogram plot of lineament frequency against orientation. (c) Length of the lineaments against frequency.

4.1.6 Domain VI

Domain VI is located in the central part of the study area (Figure 4.5). The eastern part of this domain is comprised of undifferentiated Paleogene flysch (NIOC, 1977; Figure 2.2) and the central part of the domain consists of sedimentary mélange with no recognizable stratigraphy, with tectonic blocks of Cretaceous to Miocene age. The western part of the domain consists of rhythmically bedded sandstone and shale. Low altitude areas of this domain are covered by piedmont fans and valley terrace deposits. Altogether, 780 lineaments (4.5% of the total of 17,049) are identified in domain VI. The majority of lineaments in this domain are identified in the sedimentary mélange, rhythmically bedded sandstone, and shale, with a smaller number measured in the undifferentiated Paleogene flysch.

Three main sets of lineament occur in domain VI (Figure 4.11 (A) and (B)). The first set consists of 238 lineaments oriented between N20E and N52E, and a mean orientation of N36E and a standard deviation of 8.3^{o}. The second set has 180 lineaments oriented between N5W and N10E, and a mean orientation along N-S, with a standard deviation of 2.82^{o}. The third set consists of 152 lineaments oriented between N5W and N30W, and a mean along N26W with a standard deviation of 7.2^{o}. In addition to these three major sets of lineaments there is a fourth set of 52 lineaments oriented between N10E and N20E with a mean of N15E and a standard deviation of 3.0^{o}. A fifth set is identified between N30W and N50W (76 lineaments) with a mean along N39W and a standard deviation of 5.5^{o}. About 30 lineaments, oriented between 075 and 120, with a mean along 098 (or S82E) with a standard deviation of 12.3^{o} define another set. The standard deviation shows that these lineament clusters are dispersed and hence not

considered as an individual set. However, EES-WWN mean orientation may have some structural significance.

Table 4.6: Statistics of the three main sets of lineaments in domain VI.

	Orientation	**No. of lineaments**	**Mean**	**Standard Deviation**
Set 1	N20E-N52E	238	N36E	8.3
Set 2	N5E-N10E	180	N-S	2.82
Set 3	N5W-N30W	152	N26W	7.2

The maximum and the minimum length of the lineaments in the domain VI are 92 m and 5.1 km, respectively. The lengths of the lineaments have a log-normal distribution (Figure 4.11 (C)). Most lineaments have length between 200 and 1,400 m, with a maximum between 350 and 650 m. The number of lineaments on either side of this range falls rapidly. The longest lineament is more than 5 km long, but only a few are longer than 3 km.

4.1.7 Domain VII

Domain VII is situated in the mid-northern part of the study area (Figure 4.5). This domain is predominantly made of sedimentary mélange with sheared and boudinaged sediments containing tectonic blocks of Cretaceous to Miocene age (Figure 2.2). The northern part of the domain has some rhythmically bedded sandstone and shale, with piedmont fan and valley terrace deposits covering low elevation areas. There are 4,904 lineaments (28.7% of the total of 17,049) in this domain. The lineament density is very high in this domain. Almost all of the lineaments are identified in the sedimentary mélange.

Three main lineament sets occur in this domain (Figure 4.12 (A) and (B)). The lineaments of the first set, which consists of 1,977 lineaments, are oriented between N25E and N75E, with mean orientation of N46E and a standard deviation of 10.8^{o}. The second set has 1,250 lineaments which are oriented between N10W and N10E, with a mean orientation of N2W and a standard deviation of 2.79^{o}. The third set consists of 1,117 lineaments, which are oriented between N10W and N45W with a mean orientation of N35W and a standard deviation of 9.6^{o}. In addition to these three major sets of lineaments, a fourth set is oriented between N10E and N25E (290 lineaments), with a mean of N17E and a standard deviation of 4.4^{o}. About 55 lineaments oriented between N85E and S80E (085 and 100^{o}) with a mean along E-W direction and a standard deviation of 3.3^{o} are also recognized.

Table 4.7: Statistics of the three main sets of lineaments in domain VII.

	Orientation	**No. of lineaments**	**Mean**	**Standard Deviation**
Set 1	N25E-N75E	1,977	N46E	10.8
Set 2	N10W-N10E	1,250	N2W	2.79
Set 3	N10W-N45W	1,117	N35W	9.6

The length of the shortest and the longest lineaments in domain VII are 46 m and 19 km, respectively. The lengths of the lineaments in this domain also show a log-normal distribution (Figure 4.12 (C). The majority of the lineaments have length between 200 and 1,000 m, with a maximum between 400 and 800 m. The length of the longest lineament is greater than 19 km but only a few are longer than 3 km.

A

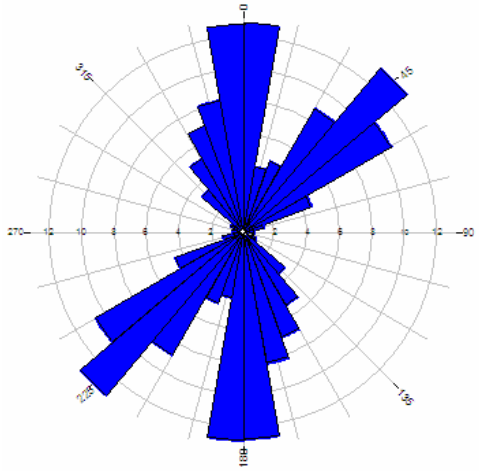

B

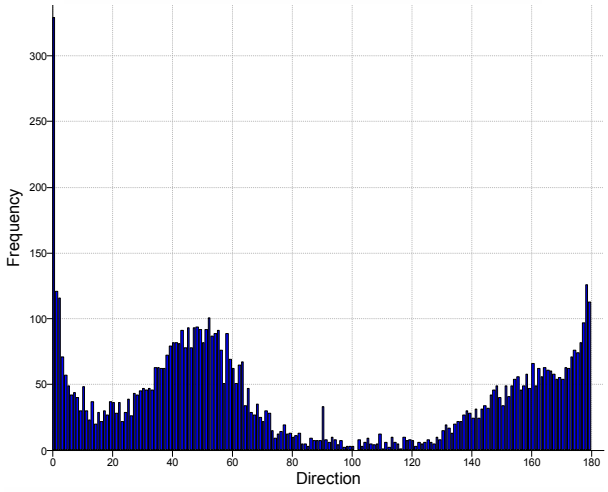

C

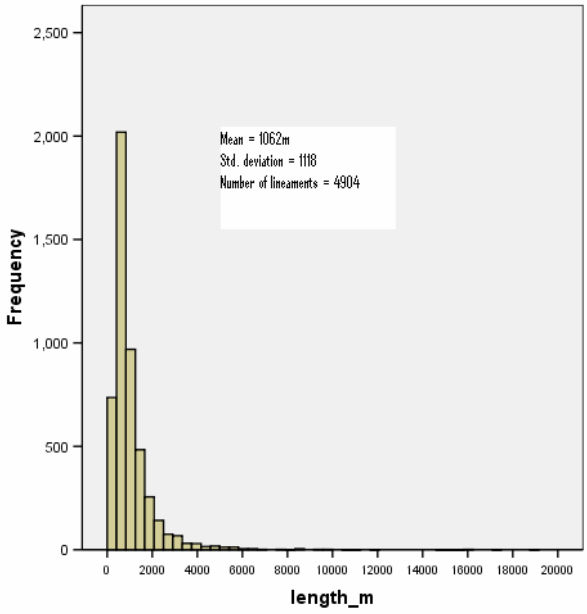

Figure 4.12: Plots of 4,904 lineaments in Domain VII. (A) Rose diagram showing lineaments frequency against orientation. (B) Histogram plot of lineament frequency against orientation. (C) Length of the lineaments against frequency.

4.1.8 Domain VIII

Domain VIII is situated in the northern part of the study area (Figure 4.5). This domain is made of colored mélange with gabbro and dunite (NIOC, 1977). It also consists of basalt and basaltic andesite with pillow lava (Figure 2.2). The northern part of the domain also has some rhythmically bedded sandstone and shale, exotic crystalline limestone, schist and diabase. Structurally, the domain is bounded to the north by the Jaz-Murian depression, and to the south by the Kuh-e-Taku thrust, which separates the colored mélange sequence (north) to the sedimentary mélange sequence (south).

Domain VIII consists of 1,500 lineaments (8.8% of the total of 17,049). Three major sets of lineament occur in this domain (Figure 4.13 (A) and (B)). The first set consists of 529 lineaments oriented between N30E and N60E, with a mean orientation along N45E and a standard deviation of 7.7^{o}. The second set has 350 lineaments which are oriented between N10W and N10E, and a mean orientation along N-S and with a standard deviation of 4.3^{o}. Similarly, the third set has 214 lineaments oriented between N25W and N47W with a mean orientation of N36W and a standard deviation of 5.8^{o}. In addition to these major sets of lineament, a fourth set oriented between N10E and N30E (176 lineaments) has a mean orientation of N20E and a standard deviation of 5.9^{o}. There are also 130 lineaments which are clustered between N10W and N35W with a mean orientation of N18W and a standard deviation of 4.3^{o}.

Table 4.8: Statistics of the three main sets of lineaments in domain VIII.

	Orientation	**No. of lineaments**	**Mean**	**Standard Deviation**
Set 1	N30E-N60E	529	N45E	7.7
Set 2	N10W-N10E	350	N-S	4.3
Set 3	N25W-N47W	214	N36W	5.8

A

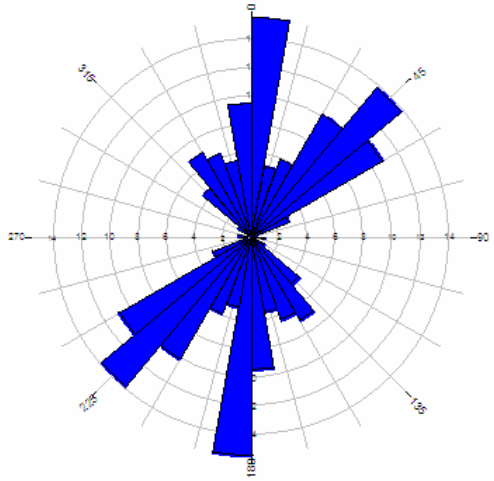

B

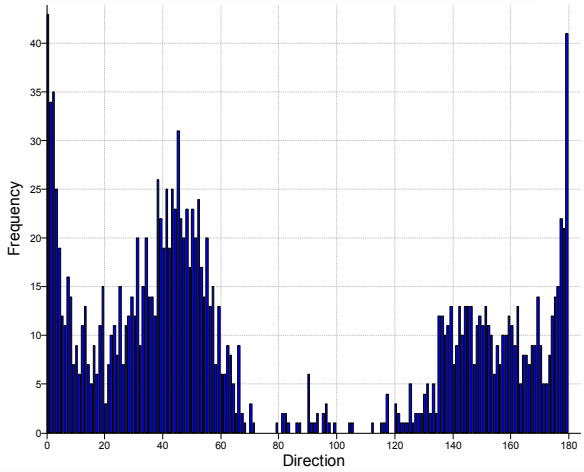

C

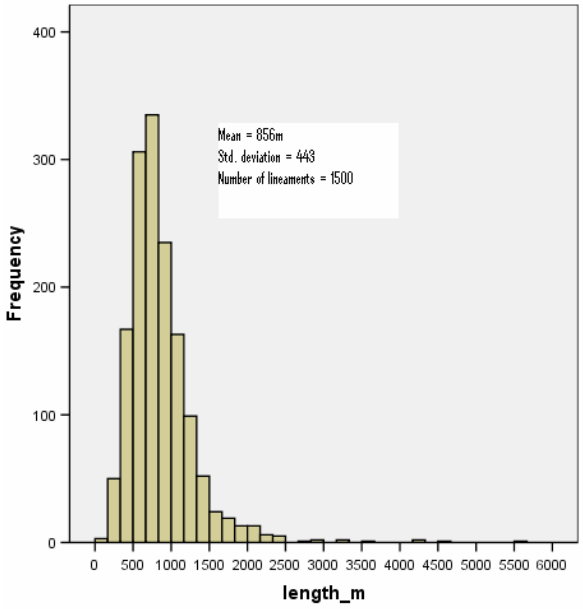

Figure 4.13: Plots of 1,500 lineaments in Domain VIII. (A) Rose diagram showing lineaments frequency against orientation. (B) Histogram plot of lineament frequency against orientation. (C) Length of the lineaments against frequency.

The length of the shortest and the longest lineaments in domain VIII are 134 m and more than 5.6 km, respectively. The length of the lineaments shows a positively skewed log-normal distribution (Figure 4.13 (C)). The maximum length lies between 500 and 850 m, with most of the lengths within the range of 500 and 1,000 m. The number falls rapidly on either side of this range. The longest lineament is more than 5.6 km, and only a few of them are longer than 2,500 m.

4.1.9 Domain IX

Domain IX is situated in the mid-western part of the study area (Figure 4.5). The domain is basically made of the Oligocene and Miocene flysch (NIOC, 1977). The area also consists of rhythmically bedded sandstone and shale and some sedimentary mélange (Figure 2.2). There are also some oval shaped synclines filled with deltaic sediments (NIOC, 1977). Piedmont fan and terrace deposits cover the low altitude areas.

There are 1,157 lineaments (6.7% of the total of 17,049) in the domain. Three prominent sets of lineament exist in this domain (Figure 4.14 (A) and (B)). The first set of 420 lineaments is oriented between N15E and N56E with a mean of N36E and a standard deviation of 10.5^{o}. The second set has 412 lineaments, which are oriented between N15W and N15E with a mean along N-S and a standard deviation of 6.8^{o}. The third set has 178 lineaments which are oriented between N24W and N45W with a mean of N33W and a standard deviation of 5.6^{o}. In addition to these three major sets of lineaments, there is a fourth set which is oriented between N12W and N24W (82 lineaments) with a mean at N18W and a standard deviation of 3.5^{o}. 12 lineaments are also recorded between N80E and S80E (080 and 100^{o}).

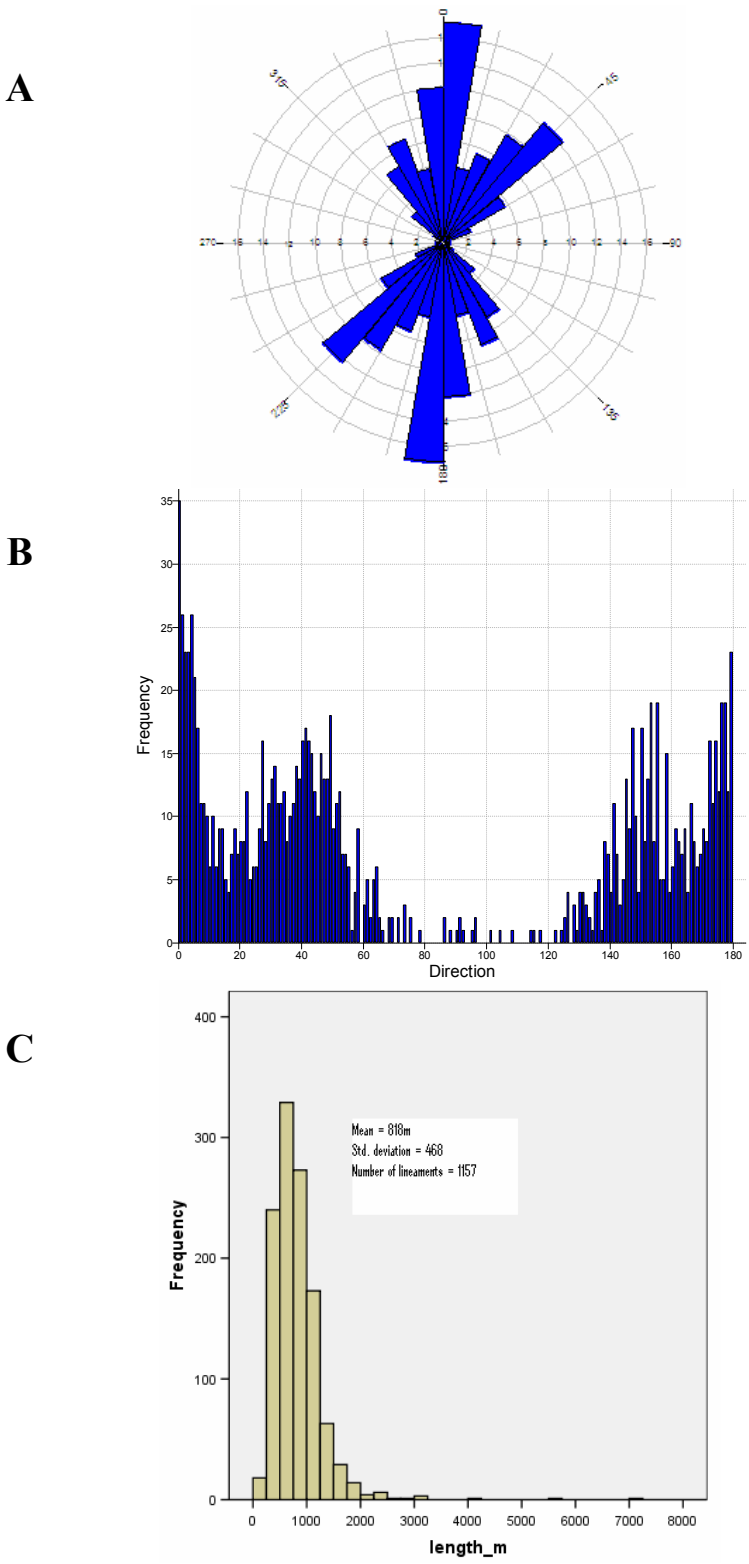

Figure 4.14: Plots of 1,157 lineaments in Domain IX. (A) Rose diagram showing lineaments frequency against orientation. (B) Histogram plot of lineament frequency against orientation. (C) Length of the lineaments against frequency.

Table 4.9: Statistics of the three main sets of lineaments in domain IX.

	Orientation	No. of lineaments	Mean	Standard Deviation
Set 1	N15E-N56E	420	N36E	10.5
Set 2	N15W-N15E	412	N-S	6.8
Set 3	N24W-N45W	178	N33W	5.6

The minimum and the maximum length of the lineaments are 172 m and 7.2 km, respectively. The lengths of the lineaments have a log-normal distribution (Figure 4.14 (C)). Although the maximum frequency lies between 400 and 600 m, majority of lineaments have length between 250 m and 1,000 m. The number of lineaments on either side of this range falls rapidly. The longest lineament is more than 7.2 km but only a few are longer than 2 km.

4.1.10 Domain X

Domain X is situated in the western part of the study area (Figure 4.5). It is made of NW-SE oriented oval shaped alternating anticlinal and synclinal folds. The lower part of the domain is covered by low level piedmont fan and valley terrace deposits. The middle part is comprised of less weathered grey marls, alternating with limestone (Figure 2.2). It also consists of rhythmically bedded sandstone and shale. The upper part of the domain is made of the Oligocene and Oligocene-Miocene deposits.

1,404 lineaments (8.2% of the total of 17,049) are identified in this domain, which can be divided into three main sets (Figure 14.15 (A) and (B)). The first set consists of 529 lineaments which are oriented between N12W and N15E, with a mean orientation along N-S, and a standard deviation of 5.6^{o}. The second set represents 393 lineaments oriented between N26E and N60E, with a mean of N42E and a standard deviation of 8.1^{o}. The third set consists of 232 lineaments which range between N27W and N55W, and

have a mean along N39W and a standard deviation of 6.9^{o}. In addition to these three major sets of lineaments, there is a fourth set having 112 lineaments which are oriented between N12W and N27W, and have a mean of N20W and a standard deviation of 4.2^{o}. Moreover, there are about 76 lineaments oriented between N15E and N26E with a mean at N20E and a standard deviation of 3.0^{o}.

Table 4.10: Statistics of the three main sets of lineaments in domain X.

	Orientation	**No. of lineaments**	**Mean**	**Standard Deviation**
Set 1	N12W-N15E	529	N-S	5.6
Set 2	N26E-N60E	393	N42E	8.1
Set 3	N27W-N55W	232	N39W	6.9

The shortest and the longest lineaments in the domain are 145 m and 2,832 m respectively. The lineaments show a log-normal distribution (Figure 4.15 (C)). The majority of the lineaments are within the range of 300 and 700 m, with a maximum between 350 and 550 m. The number on either side of this range falls rapidly. Although the longest lineament is greater than 2,800 m, only a few are longer than 1,400 m.

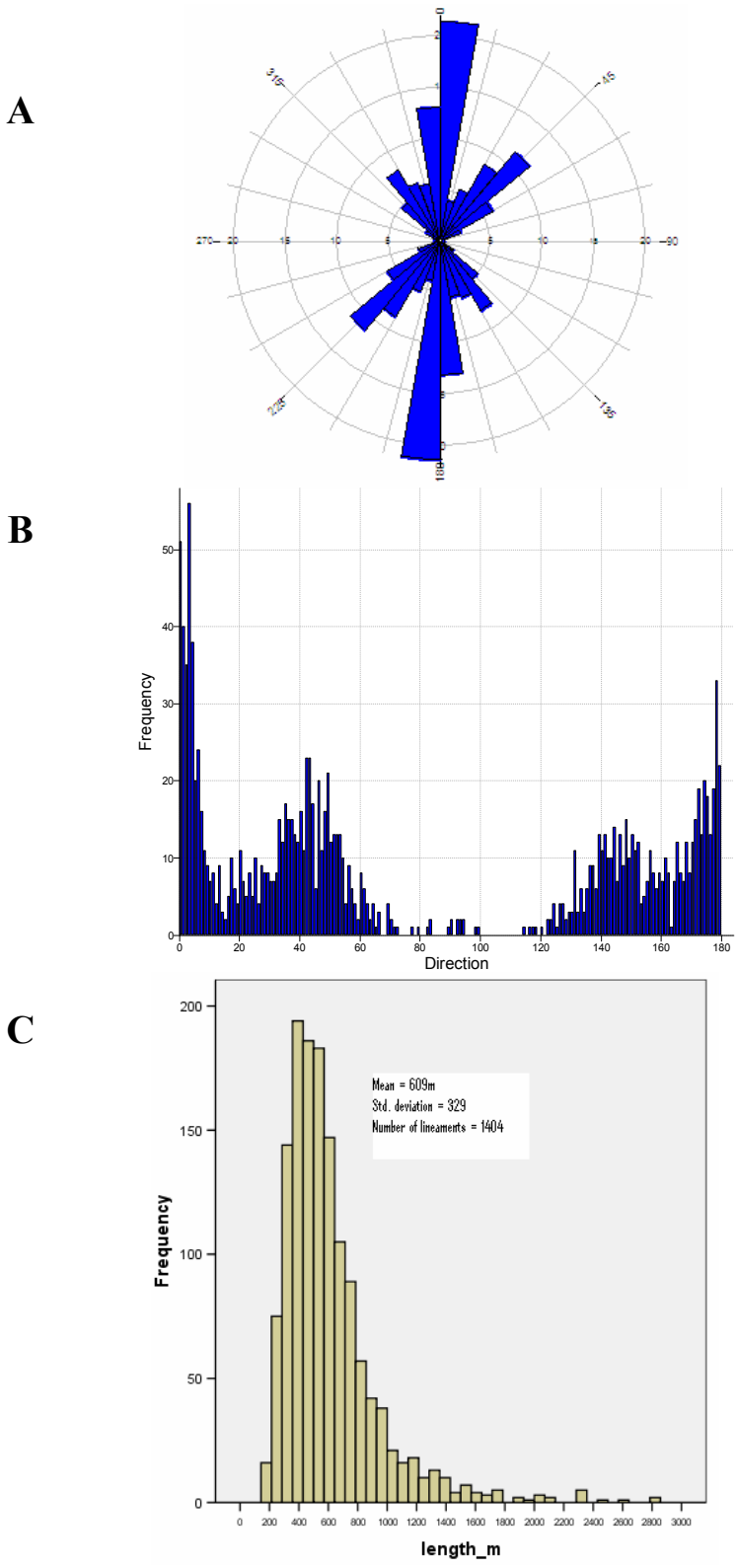

Figure 4.15: Plots of 1,404 lineaments in Domain X. (A) Rose diagram showing lineaments frequency against orientation. (B) Histogram plot of lineament frequency against orientation. (C) Length of the lineaments against frequency.

CHAPTER 5. Results and Discussion

5.1 Fracture analysis

Rock undergoing brittle deformation under a contractional regime, such as the one in an accretionary prism, may develop three different types of fractures; extensional, shear, and transitional tensile fracture also known as hybrid shear (Suppe, 1985; Hancock, 1985). Two intersecting sets of shear fracture that simultaneously form under the same state of stress constitute a conjugate set (array or pair) (Marshak and Mitra, 1988). The acute angle between the conjugate set is estimated to be roughly 60^{o} for a homogenous, flawless and intact rock according to the Coulomb friction criterion (Byerlee, 1978). The Anderson-Byerlee fault mechanism (Anderson, 1951) assumes that, the bisector of the angle (2α) between these two conjugate sets faces the maximum principal compressive stress (σ_1) direction. Experimental work (Twiss and Moores, 2007) shows that tensile fractures are formed parallel to the σ_1 direction and shear fractures are formed at about 30^{o} to the σ_1 direction.

Among the 17,049 lineaments mapped in the study area, the sets trending NW-SE and NE-SW are conjugate sets of strike slip faults with significant amount of displacement. I used the two-line technique to measure the true attitude of the conjugate sets of fracture planes. In order to ensure the quality of the data, I measured the attitude only for domains I, II, IV, VI and VII where the conjugate sets are seen prominently with the help of the DEM and digitally enhanced satellite images as shown in the corresponding figures below. The digital elevation model was used to measure the elevation of any given two points on the fracture segment, and the relief *(dh)* was calculated by subtracting the elevation of the points (points A and B or, B and C in Figure

5.1(A)). The ArcGIS distance-measuring tool was used to measure the horizontal distance *(dx)* between the two points (AB and BC in Figure 5.1(A)). The trends of the fractures were measured using the ArcGIS direction-measuring tool and the plunges of the fractures *(θ)* were measured by using the following formula:

$$\tan \theta = dh/dx$$

$$\text{Plunge } (\theta) = \arctan (dh/dx)$$

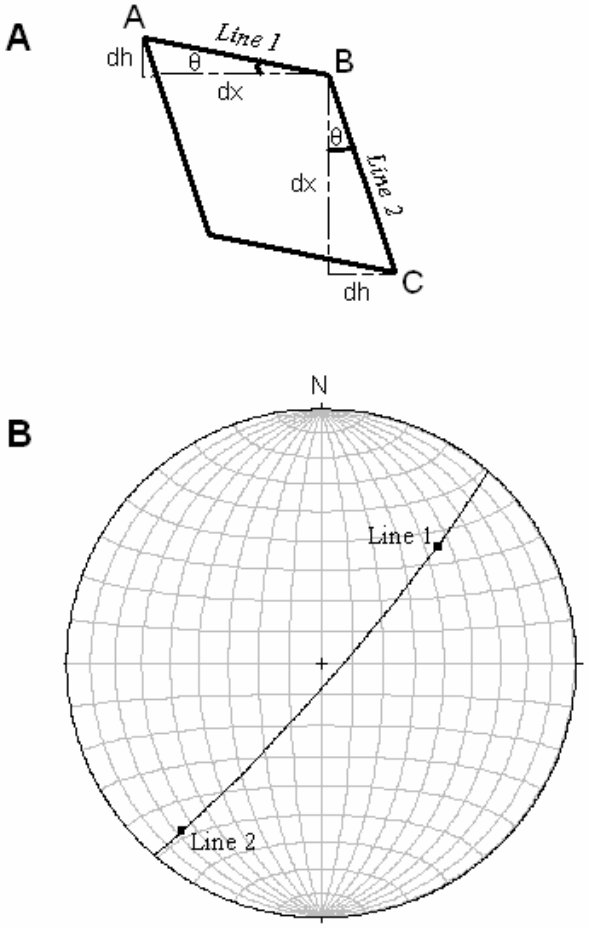

Figure 5.1: Two-line technique applied for the measurement of the attitude of a plane. (A) trend and plunge of the lines 1 and 2 were measured by using the DEM and ArcGIS distance and direction measuring tools. (B) The trend and plunge of the lines were plotted on a equal area stereonet in order to measure the attitude of the corresponding plane.

Both the trend and plunge were plotted on the equal area stereonet where they were projected as points (Figure 5.1 (B)). Since both of the lines are parts of the same fracture plane, they aligned on the same great circle as shown in Figure 5.1 (B). The attitude of the plane was measured by reading the strike, dip-angle and the dip-direction on the stereonet.

In domain I, the first two sets of fractures, with mean trends N39E and N35W, show clear displacement of the tectonostratigraphic contacts, indicating that they are shear fractures. I applied the two-line technique to estimate the attitude of the NE and NW trending conjugate sets as described in Figures 5.1 above. Elevations were measured along the lines plunging in opposite directions (Figure 5.2 (A)). Two sets of lineaments were measured and aligned in the great circles (Figure 5.2 (B)). Since both great circles are dipping in opposite directions, and the dihedral, acute angle (2α) between them is about 70^{o}, these two sets can be considered as conjugate set of shear fractures that formed under the same state of stress. The calculated value of 2α (i.e., 70^{o}) is consistent to the value of 74^{o} derived from the lineament analysis by plotting the histogram and the rose diagram as shown in Figure 4.6 (A) and (B). The 37^{o} angle of α is very close to the value reported in experimental deformation of rock under laboratory conditions (Twiss and Moores, 2007). In domain I, the direction of the mean σ_1 along the bisector of the two sets can be estimated to be N2E. When the direction of σ_1 persists through time, an extensional set of fracture develops sub-parallel to it (i.e., at $\alpha \cong 0$). In domain I, the third set of fracture with mean at N2W is almost parallel to the calculated value of σ_1 (i. e., N2E) and hence considered as the extensional set. In addition, the fourth and fifth set with mean orientation at N17W and N16E respectively fall within the conjugate sets and

hence are considered as the subsidiary sets formed in between the two major conjugate sets.

A

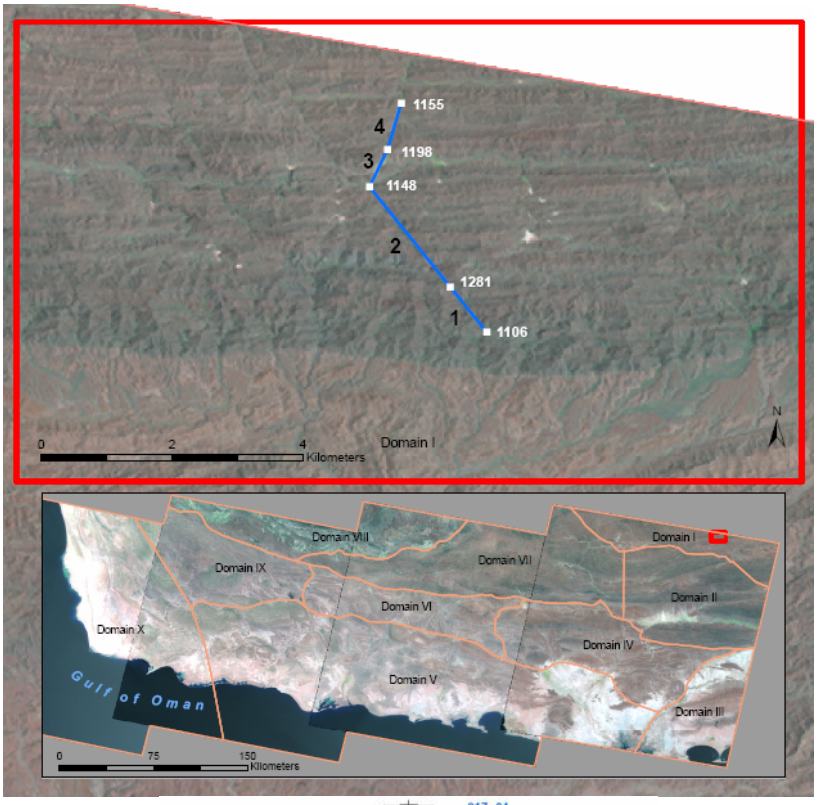

B

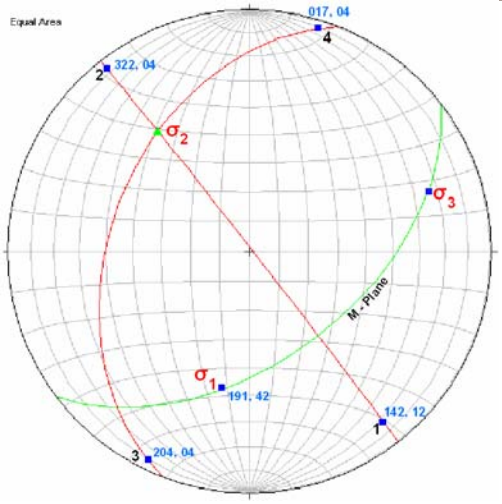

Figure 5.2: The two-line technique applied to estimate the attitude of a pair of conjugate sets in domain I. (A) white boxes are the points where the elevation were measured by using the DEM. Blue lines labeled with 1, 2 and 3,4 are NW and NE trending fractures respectively. (B) Conjugate sets calculated by aligning the points 1, 2 and 3, 4 (blue dots with trend and plunge) on the great circles. σ_1, σ_2 and σ_3 are the maximum, intermediate and the minimum principle stresses respectively. M-plane = movement plane.

In domain II, the two-line technique, applied to estimate the attitude of the planes, shows that the first and second sets of lineaments with mean orientation at N45W and N32E are conjugate sets of shear fractures (Figure 4.7 (A) and (B); Figure 5.3). The trend and plunge of the two lines measured using the DEM and the ArcGIS distance and direction measuring tools as described in Figure 5.1 (A) and (B) show that the NE and the NW trending fracture sets have attitudes of N34E, 48E and N26W, 83E, respectively (Figure 5.3 (B)). The angle 2α between these conjugate shear fractures was calculated as 70^{o}. This value is consistent with the angle (2α) of 76^{o} derived by analyzing more than 1,700 lineaments in domain II. The 38^{o} angle of α is close to the value reported in experimental deformation of rock under laboratory conditions. In domain II, the direction of the maximum principle stress (σ_1) along the bisector of the two conjugate sets can be estimated as N6W. The third set having a mean orientation of N2W is subparallel to the σ_1 direction. The orientation of σ_1 derived from the two-line technique is N18E, 32^{o} (Figure 5.4 (B)). The discrepancy may be due to the local heterogeneity in the small area in domain II (Figure 5.3 (A)). However, the orientation is within the range of the angle of 2α (i.e., N45W to N32E) as shown in Figure 4.7 (A) and (B).

In addition, a fourth set with a mean orientation of N25W is close to the first set (mean at N45W), and considered as a subsidiary set. There are about 90 highly dispersed lineaments with standard deviation of about 29^{o} in E-W direction (Figure 4.7 (A) and (B)). This is not considered as a separate set.

A

B

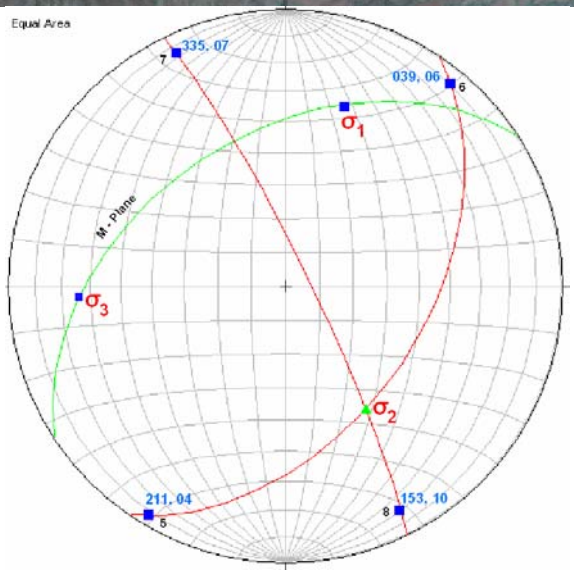

Figure 5.3: The two-line technique applied to estimate the attitude of a pair of conjugate sets in domain II. (A) white boxes are the points where the elevation were measured by using the DEM. Blue lines labeled with 5, 6 and 7, 8 are NE and NW trending fractures respectively. (B) Conjugate sets calculated by aligning the points 5, 6 and 7, 8 (blue dots with trend and plunge) on the great circles. σ_1, σ_2 and σ_3 are the maximum, intermediate and the minimum principal stresses respectively. M-plane = movement plane (i.e., the $\sigma_1\sigma_3$ plane).

In domain III, the first two sets of lineaments with mean trend at N28W and N34E are conjugate sets of shear fractures (Figure 4.8 (A) and (B)). The angle between these conjugate sets (2α) is about 62^o. The 31^o angle of α is close to the value reported in experimental deformation of rock under laboratory conditions. The direction of maximum principle stress (σ_1) along the bisector of the two conjugate sets can be estimated as N3E. The direction of σ_1 is almost parallel to the third set of lineaments trending N1W direction which may have formed as extensional fractures when σ_1 persists over time. In addition to this, the fourth set with a mean trend of N12W fall within NW-SE and N-S orientated fractures, and hence considered as a subsidiary. About 10 lineaments also exist at about E-W direction which may have formed as tension gashes.

In domain IV, the first and third sets of lineaments trending N38E and N30W, respectively are conjugate sets of shear fractures (Figure 4.9 (A) and (B)). The dihedral angle between the conjugate sets (2α) is about 68^o. The angle of α (i.e., 34^o) is close to the value derived from the laboratory experiment. Therefore, the direction of maximum principle stress (σ_1) can be estimated as N4E. In addition, the two-line technique was applied to the two of the NW and NE orientated fractures in the middle part of domain IV (Figure 5.4 (A)) in order to calculate the attitudes of the conjugate fractures and to estimate the direction of σ_1. The trends of the three NW and two NE trending lineaments were measured by using the ArcGIS direction measuring tool, and the plunges were calculated by using the DEM as shown in Figure 5.4 (A).

A

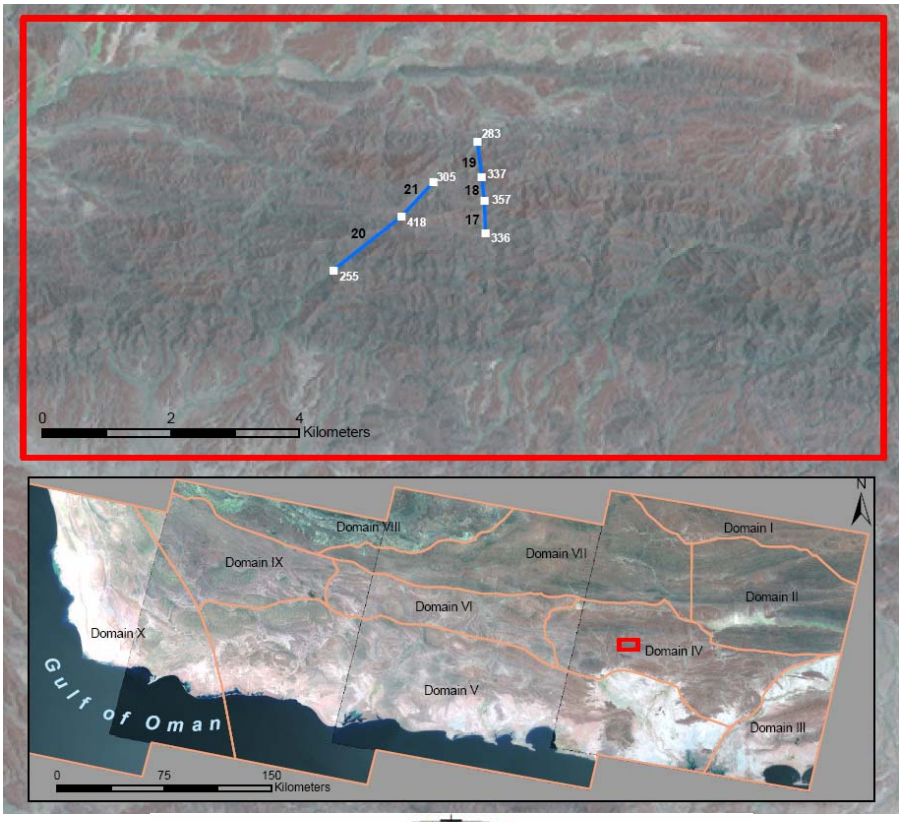

B

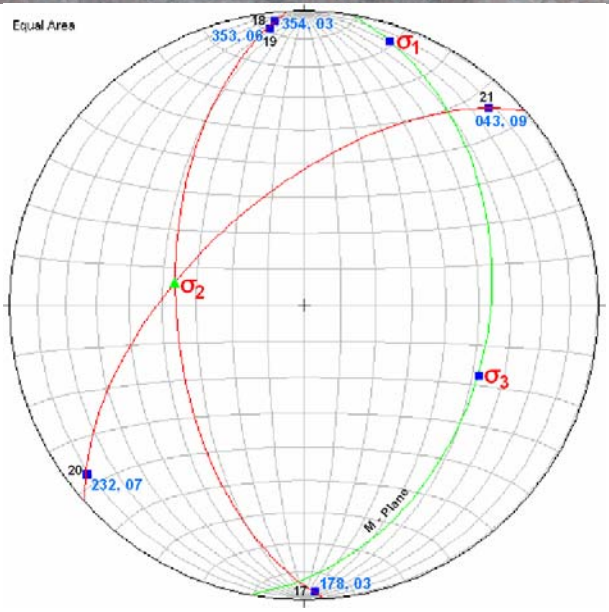

Figure 5.4: The two-line technique applied to estimate the attitude of a pair of conjugate sets in domain IV. (A) white boxes are the points where the elevation were measured by using the DEM. Blue lines labeled with 17, 18, 19, 20 and 21 are NE and NW trending fractures respectively. (B) Conjugate sets calculated by aligning the points 17, 18, 19 and 20, 21 (blue dots with trend and plunge) on the great circles. σ_1, σ_2 and σ_3 are the maximum, intermediate and the minimum principle stresses respectively. M-plane = movement plane.

The trends and plunges were plotted on the equal area steroenet as described in Figure 5.1, which were projected as lines on the net (Figure 5.4 (B)). The attitudes of the conjugate sets were calculated as N4W, 54W and N48E, 60W for the NW and NE trending conjugate fractures respectively (Figure 5.4). The maximum principal stress direction (σ_1) was estimated to be N18E, 6^o (Figure 5.4 (B)). This value is about 14^o off from N4E which was derived by analyzing more than 1,600 lineaments in the domain. The discrepancy may be due to the local heterogeneity in the small area in domain IV (Figure 5.4 (A)). The orientation however is within the range of the value of 2α (i.e., N38E and N30W).

Further, the third set with a mean orientation of N-S may have formed as an extensional set when the σ_1 persists over a long period. In addition, the set with a mean trend at N14W falls within NW-SE and N-S oriented fractures and hence considered as subsidiary to the conjugate sets. About 75 lineaments oriented about N44W may be a subsidiary set formed along major NW-SE set.

In domain V, the second and third sets of lineaments trending N41E and N27W, respectively are conjugate shear fractures (Figure 4.10 (A) and (B)). The angle 2α between the two conjugate sets is about 68^o. The 34^o angle of α is close to the value derived from the laboratory experiment. The direction of maximum principal stress (σ_1) can be estimated as N7E. The first set trending N1W is within 10^o of the σ_1 and may have formed as an extensional sets as the σ_1 persisted through time. The frequency of the lineaments is higher in this direction because domain V includes a number of E-W trending folds (both synclines and anticlines), and the majority of fractures are developed along the limbs of the folds. In addition to this, there are two more minor sets of fractures

with a mean trend of N16W and N16E, since these fractures fall within the major sets of the fractures they are considered as subsidiary sets.

In domain VI, there are three main sets of lineaments with a mean orientation of N36E, N-S, and N26W. Among these, the first and third sets of lineaments can be considered as conjugate sets of shear fractures (Figure 4.11 (A) and (B)). The angle 2α between the two conjugate sets is about 62^{o}. The angle α (i.e., 31^{o}) matches the value derived from the laboratory experiment; hence, the direction of maximum principle direction σ_1 can be estimated as N5E. The second set trending N-S can be considered as an extensional set .In addition, there are about 76 lineaments with a mean of N39W and about 52 lineaments with a mean of N15E directions. Since these two have relatively low frequencies and fall within the major sets, they are considered subsidiary to the conjugate sets. Furthermore, there are about 30 spatially and statistically dispersed (with standard deviation of 12.3^{o}) lineaments which might not have any structural and statistical significance.

In addition, the two-line technique was applied to the NW and NE trending conjugate sets in order to calculate the attitude of the fracture sets and the orientation of the σ_1. The trends and plunges of the lines 13, 14 and 15, 16 for the NW and NE orientated lineaments were calculated using the DEM and distance and direction measuring tools in ArcGIS (Figure 5.5 (A)). The trends and plunges of the lines were plotted on the stereonet, which were projected as points (Figure 5.5 (B)).

A

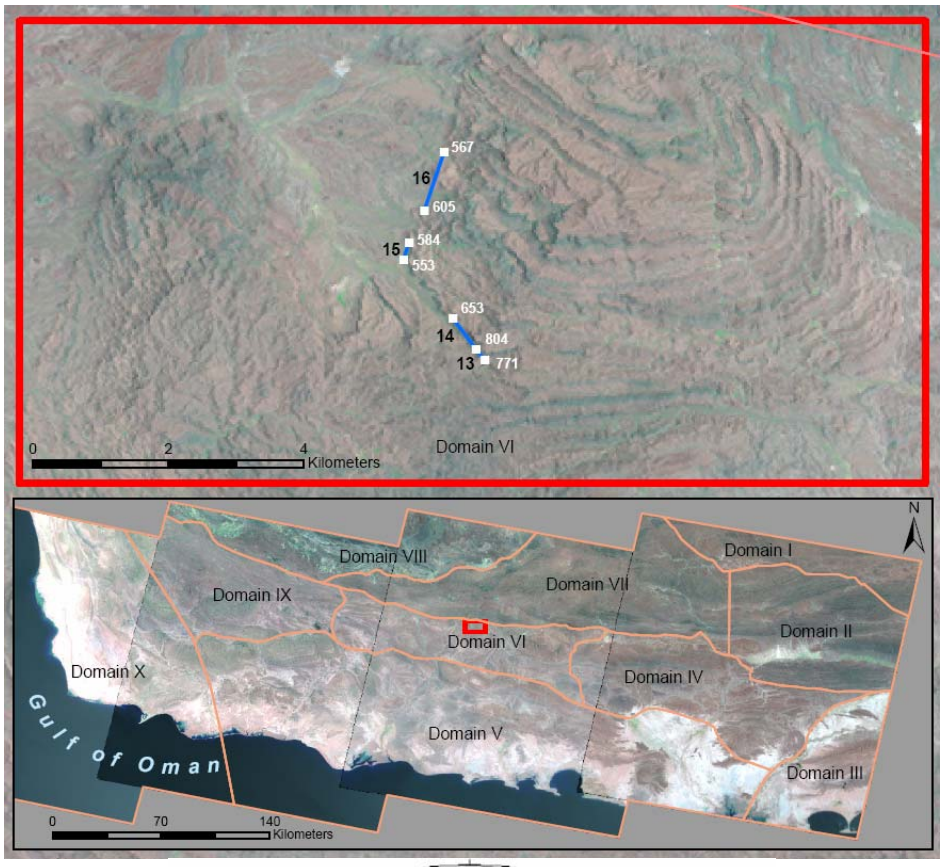

B

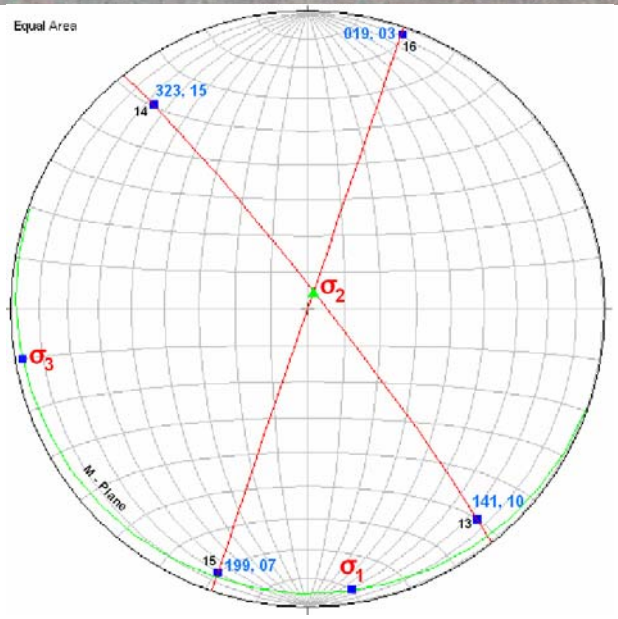

Figure 5.5: Two-line technique applied to estimate the attitude of a pair of conjugate sets in domain VI. (A) white boxes are the points where the elevation were measured by using the DEM. Blue lines labeled with 13, 14 and 15, 16 are NW and NE trending fractures respectively. (B) Conjugate sets calculated by aligning the points 13, 14, 15 and 16 (blue dots with trend and plunge) on the great circles. σ_1, σ_2 and σ_3 are the maximum, intermediate and the minimum principle stresses. M-plane = movement plane.

The attitude of the conjugate fracture sets were determined by aligning the points in the great circles. The values were calculated as N38W, 85E and N18E, 89W for the NW and the NE sets respectively (Figure 5.5 (B)). The direction of σ_1 was calculated as S9E, 4 (or, N9W, 4). The direction of σ_1 is about 14^o off the direction of N5E estimated by using the lineaments analysis in domain VI. This discrepancy may be due to the local heterogeneity in domain VI. However, considering the standard deviation of the NE and NW trending lineaments being 8.3^o and 7.2^o respectively, the N9W value can be considered as consistent with NS shortening direction.

Domain VII consists of the largest number of lineaments in terms of both frequency and density. The domain is basically comprised of well exposed sedimentary mélange and rhythmically bedded sandstone and shale where the structures are easily identifiable in the satellite images. The domain has three major sets of lineaments as shown in figure 4.12 (A) and (B). The angle between the first set with a mean trend of N46E, and the third set with a mean trend of N35W is about 80^o, which is noticeably higher than the value derived from the laboratory experiment. The high standard deviations of both for these sets (i. e., 10.8^o and 9.6^o respectively) suggest that the orientation data are highly random. Since the angle between them is less than 90^o, we can still consider the sets as conjugate shear fractures, and the angle between them (2α) as 80^o. The sense of movement is left-lateral and right-lateral for the first and second sets, respectively (Figure 5.6 (A)). The 40^o angle of α can be used to derive the direction of maximum principal stress (σ_1), which is estimated to be N6E. The second set with a mean orientation of N2W is subparallel to the σ_1 direction and hence considered as

extensional set. The discrepancy of 8^{o} might be due to rotation after the formation of the conjugate sets.

The two-line technique was applied to the NE and NW trending fractures in order to calculate the attitudes of the planes and to estimate the direction of σ_1. The trend and plunge of the lines 9, 10 and, 11, 12 for the NE and NW trending lineaments were calculated by using the DEM, and the distance and direction-measuring tool in ArcGIS (Figure 5.6 (A)). The calculated trend and plunge of these lines were plotted on the stereonet (Figure 5.6 (B)). The attitude of the conjugate sets (strike, dip amount and dip direction) was calculated by aligning the lines on the great circles (Figure 5.6 (B)). The strike, dip values were calculated as N50W, 89N and N9W, 89E for the NE and NW trending fractures, respectively. The direction of σ_1 was calculated to be N18E, 6^{o}. This direction is 12^{o} off from the value of N6E derived from the lineament analysis. The discrepancy might be due to the local heterogeneity in that part of the domain (Figure 5.6 (A)). Considering the NW and NE trending fractures sets with standard deviations of 10.8^{o} and 9.6^{o} respectively, the direction of σ_1 can be considered as consistent to N-S direction of shortening. In addition, a fourth set with a mean at about N17E falls within the conjugate sets. There are about 55 spatially random lineaments at about E-W direction, which might have formed as tension gashes.

A

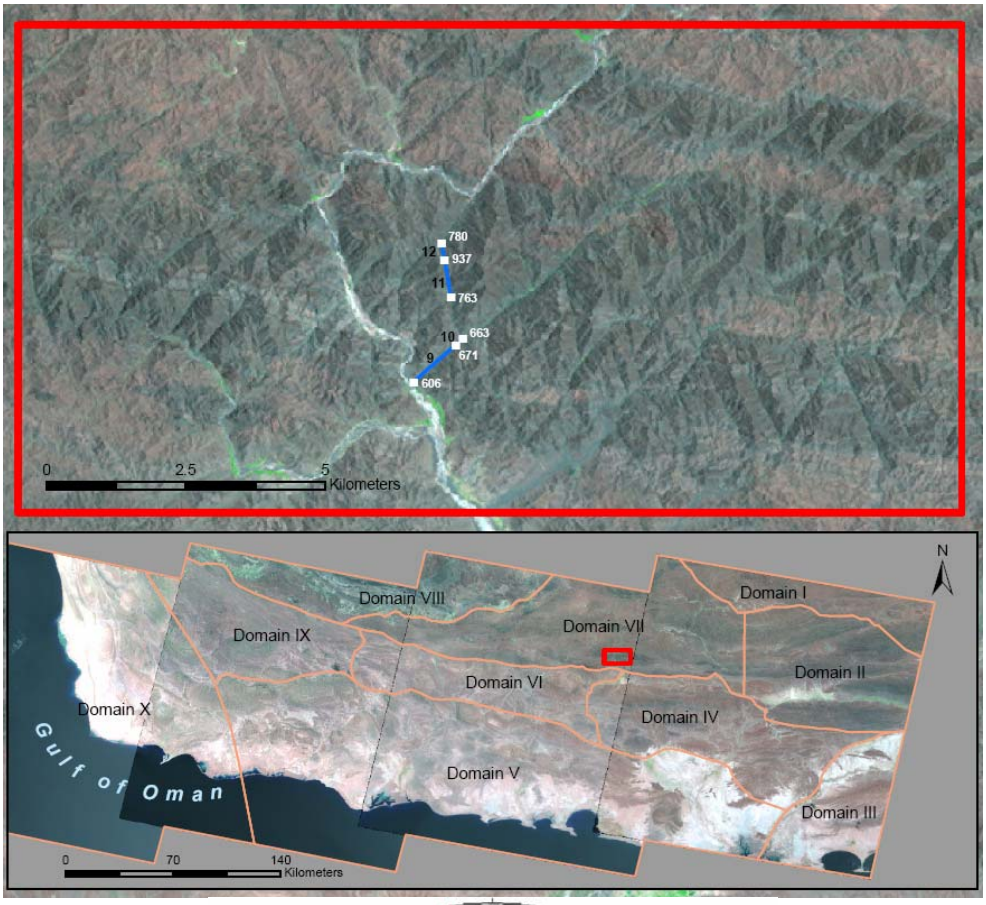

B

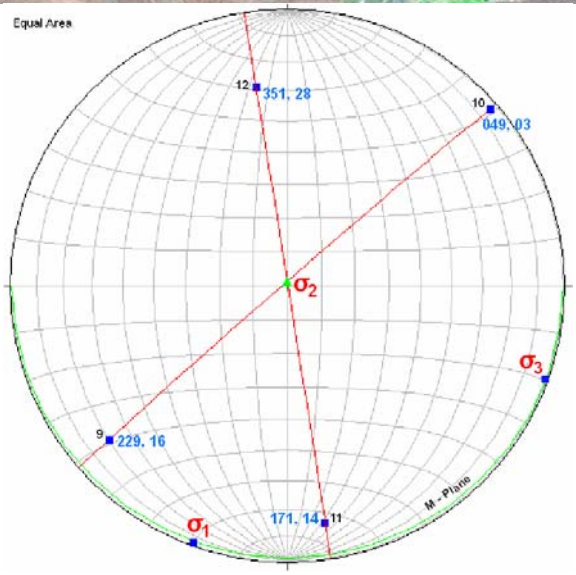

Figure 5.6: Two-line technique applied to estimate the attitude of a pair of conjugate sets in domain VII. (A) white boxes are the points where the elevation were measured by using the DEM. Blue lines labeled with 9, 10 and 11, 12 are NE and NW trending fractures respectively. (B) Conjugate sets calculated by aligning the points 9, 10 and 11, 12 (blue dots with trend and plunge) on the great circles. σ_1, σ_2 and σ_3 are the maximum, intermediate and the minimum principle stresses. M-plane = movement plane.

Domain VIII has three major sets of lineaments with a mean orientation of N45E, N-S and N36W. Among these, the first and third sets of lineaments are conjugate sets of shear fractures (Figure 4.13 (A) and (B)). The angle 2α between the conjugate sets is found to be 81^{o}. This value is significantly higher than the expected value of 2α. By definition, the bisector of the angle 2α between these two conjugate sets faces the maximum principal compressive stress σ_1 (Marshak et al., 1982). The angle α between σ_1 and each of the conjugate shears is about 40^{o} and hence the direction of mean σ_1 along the bisector of the two sets can be estimated to be N5E. The second set with a mean trend of N-S direction is an extensional set that is almost parallel to the calculated σ_{1}. In addition, the fourth set with a mean of N20E falls between the two major sets (i. e., N-S and N45E).

In domain IX, the first and third sets of lineaments trending N36E and N33W are conjugate sets of shear fractures (Figure 4.14 (A) and (B)). The angle 2α between the conjugate sets is found to be about 70^{o}. The 35^{o} angle of α is close to the value derived from the laboratory experiment. The orientation of the maximum principal compressive stress (σ_1) is estimated to be N1E. The extensional set with mean trend of N-S direction is parallel to the estimated σ_1 value. In addition to this, a fourth set with a mean orientation of N18W also exists in the domain. Since this domain is close to the right lateral Minab-Zendan fault system, this set might have formed as subsidiary riedel shears (R) synthetic to the right-lateral fault system.

Domain X is intersected by the NNW-SSE trending Minab-Zendan fault system (Figure 4.5). This right lateral fault system with a mean trend of N15W connects the

collision zone of the Zagros Fold and Thrust Belt (ZFTB) to the subduction zone of the Makran accretionary prism by transpressional tectonics (Regards et al., 2004). Since the domain is within the buffer area of 50 km of the Minab-Zendan fault system, the rocks are experiencing the simple shear deformation forming a variety of subsidiary shear fractures that are associated with the fault system in the domain (Figure 5.7).

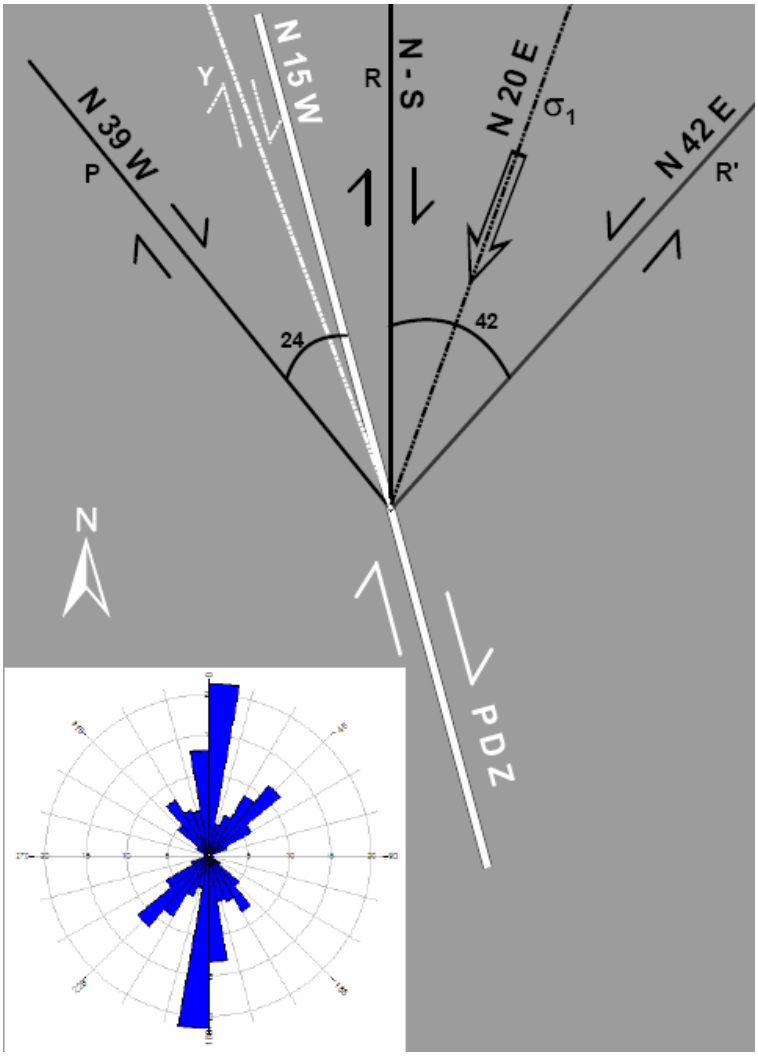

Figure 5.7: Different subsidiary shear fractures associated with the Minab-Zindan fault system (leveled as Principal Displacement Zone (PDZ) developed during simple shear deformation. See text for explanation. Inset rose diagram shows the orientation of the sets of fractures associated with the Minab Zendan fault system.

Theoretically, during simple shear deformation, different subsidiary shear fractures are developed (Sylvester, 1988; Leech, 2003; Twiss and Moores, 2007). During the progressive deformation, a complimentary system of shear fractures called Riedel R, and R', form (Price and Cosgrove, 1990). Reidel shears or, R shears, are synthetic to the main fault (develop at a small angle, i.e., roughly 10-20^{o} and have the same sense of shear as that of the main fault). The main fault is also called the Principal Displacement Zone (PDZ). P shears are another type of subsidiary fractures, which are synthetic, and may develop symmetric to the R shears on the other side of the PDZ. Conjugate reidel shears, or R' shears are antithetic (develop at high angle roughly 70-80^{o} and have an opposite sense as the PDZ). Y shears also may develop more or less parallel to the PDZ (Twiss and Moores, 2007).

Altogether 1,404 lineaments that were identified in domain X can be interpreted within the context of the Minab-Zendan right lateral strike-slip fault system. As shown in Figure 5.7, the first set of lineaments having a mean trend of N-S direction is interpreted as subsidiary reidel shear (R shear) developed synthetically to the PDZ. The second set with a mean orientation of N42E can be interpreted as conjugate reidel shear (R' shears) antithetic to the PDZ. The angle of 42^{o} between these two conjugate sets is less than theoretically expected value of about 60^{o}. This discrepancy may be due to the statistical dispersion of the data given by the 8.1^{o} standard deviation of the second set. Since the Minab-Zendan fault system is in the transitional zone between the NNE-SSW trending Zagros collision and the N-S trending subduction of the Makran accretionary prism (Regard et al., 2004), this discrepancy may also be interpreted as due to the external rotation within the simple shear system caused by the transpressional tectonics during the

transformation of collision to subduction. Therefore, the 42^o angle between the two conjugate shears can be considered as 2α and the bisector of which is parallel to the maximum principal stress (σ_1). Hence σ_1 is estimated to be oriented N20E as shown in figure 5.7. The third set with the mean at N39W is interpreted as P shear, which is symmetric to the R shear and synthetic to both R shear and the PDZ. The fourth set of lineaments with a mean trend at N20W is within 5^o of the PDZ and hence interpreted as Y shears. Moreover, there are about 76 lineaments with a mean orientation of N20E, which is parallel to the σ_1 and interpreted as extensional fractures. Table 5.1 shows the value of the angle between the two conjugate shears (2α) and the maximum principal stress (σ_1), estimated in each domain by analyzing the lineaments detected in the digitally enhanced satellite imageries and digital elevation models.

Table 5.1: The value of the dihedral angle (2α) and maximum principal stress direction (σ_1) for all the domains.

Domain	**2α (^{o})**	**σ_1**
I	74	N24E
II	76	N6W
III	62	N3E
IV	68	N4E
V	68	N7E
VI	62	N5E
VII	80	N6E
VIII	81	N6E
IX	70	N1E
X	42	N20E

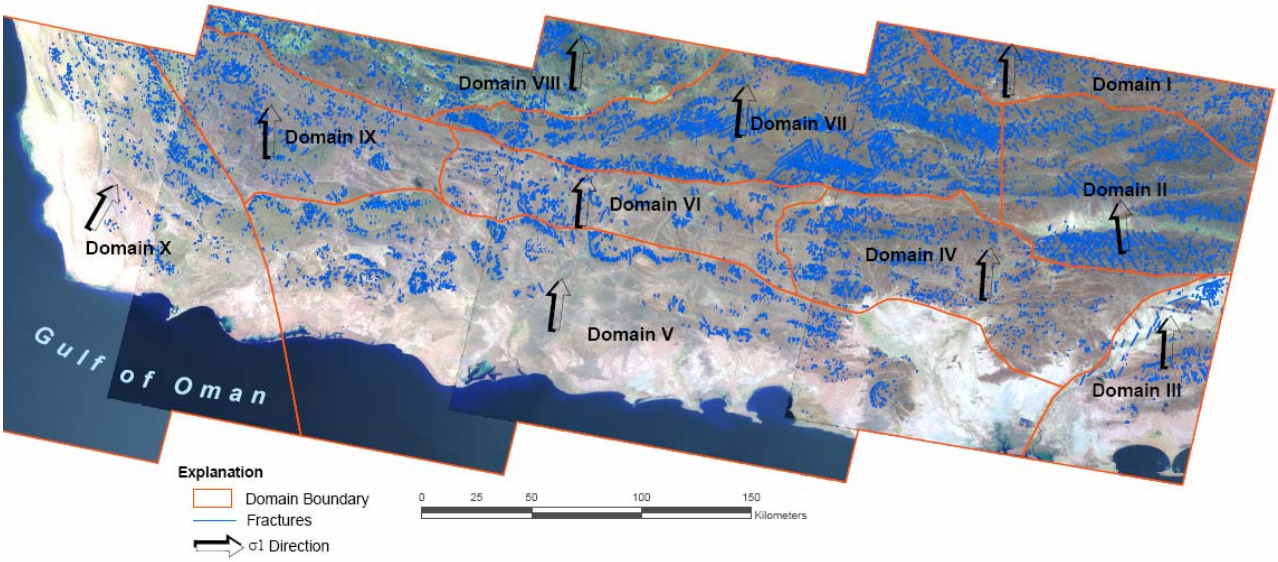

Figure 5.8: Map showing the distribution of the maximum principal stress direction (σ_1) in different domains in the study area.

The values of the dihedral angle 2α increase from southeastern domains to the northwestern domains (Table 5.1; Figure 5.8). Domain III has the lowest 2α value of 62°, which is then followed by domains V and IX with values of 68° and 70°, respectively. Similarly, further north, the value increases from domain II (76°) to domain VII (80°) and VIII (81°) (Figure 5.8). This northward incremental increase in the value of 2α may be due to horizontal shear on vertical fracture surface (Leech et al., 2003) within a pure shear system. During a progressive deformation, the conjugate sets of fractures might have separated along a vertical axis increasing the dihedral angle (2α) between them due to the internal rotation. This increment of the angle between the conjugate sets may also be described in the context of the Mohr diagram as follows:

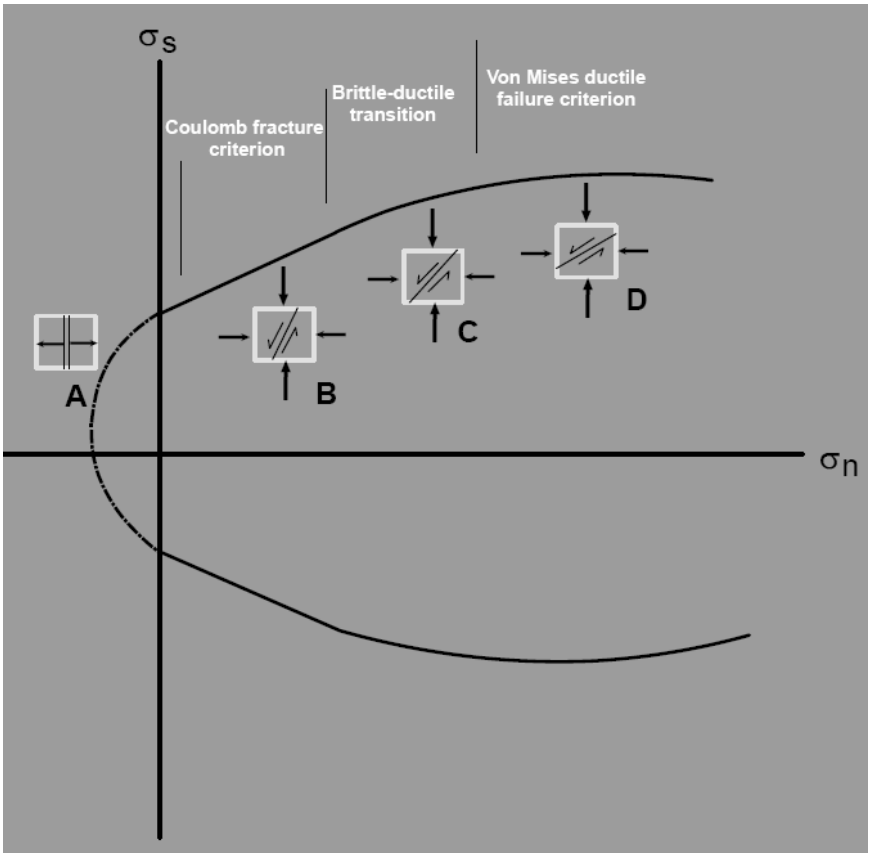

Figure 5.9: Mohr diagram showing the failure envelop and related fractures. Boxes are physical space diagrams showing the orientation of the failure plane at different points along the failure envelope. Double lines inside the box represent extension fractures: solid lines inside the boxes indicate shear fractures. (A) Tension fracture. (B) Brittle shear fracture according to Coulomb criterion. (C) Shear fracture in the brittle ductile transition. (D) Ductile shear failure according to the Von Mises criterion. σ_n = normal stress; σ_s = shear stress. [Modified after Twiss and Moores, 2007, p. 218].

If the Mohr circle is tangent to the parabolic fracture envelope, tension fractures form parallel to the maximum principal stress as shown in Figure 5.9 (A) (Twiss and Moores, 2007, p. 217). With increasing confining pressure, the Mohr circle shifts to the right, increasing its diameter, and shear fractures form according to the Coulomb fracture criterion (Figure 5.9 (B)). With continued increase in the confining pressure, the fracture envelope will become concave toward the normal stress axis decreasing the slope. Due to this, the angle between the two conjugate shears (2α) increases (Figure 5.9 (C)). With

increasing pressure, the rock behavior will shift from brittle to ductile and the Coulomb criterion is replaced by the Von Mises criterion (Figure 5.9 (D)). Due to the Von Mises criterion, the ductile deformation begins at a critical shear stress (Twiss and Moores, 2007, p. 218), and the angle between the conjugate shears 2α is further increased (Figure 5.9 (D)).

The northwestern part of the study area (domains VIII and IX) is made of older rocks (colored mélange with gabbros and, dunites and basaltic andesite with pillow lava structure see, Figure 2.2). Since, these rocks are subjected to compressional stress over a long period, the rocks may have transformed from brittle to ductile deformation increasing the angle between the conjugate sets 2α from the southeastern part to the northwestern part of the study area.

The direction of maximum principal stress (σ_1) is within the range of N6W and N7E from domain I to IX (Table 5.1). This consistency is may be due to the lack of external rotation during the pure shear deformation. However, in domain X, the Minab-Zendan fault system has been formed in the overlying strata due to the movement of the basement blocks as shown by the lab experiment conducted by Riedel (1929). Hence the higher angle of the maximum principal stress (σ_1) may be due to the external rotation during the progressive deformation in the simple shear system.

5.2 Fault analysis

Accretionary prisms are assemblages of stacked thrust sheets, which are continuously offscraped off the subducting sediments (Grando and McClay, 2007). In an out-of-sequence accretion model, the structurally higher thrust sheets are accreted first and are deformed (i.e., strained, rotated, translated) the most, and the thrusts at the toe of

the prism are the youngest structure in the prism, with the least amount of deformation. In addition to mapping fractures, I mapped the major thrust faults that bound the tectonostratigraphic units in the prism. Traces of all the major faults in the study area were detected on the satellite image with false color composite (FCC) 742, and mapped using ArcGIS 9.1 program. Altogether 233 major faults with length ranging from 800 m to longer than 152 km were identified and digitized (Figure 5.10).

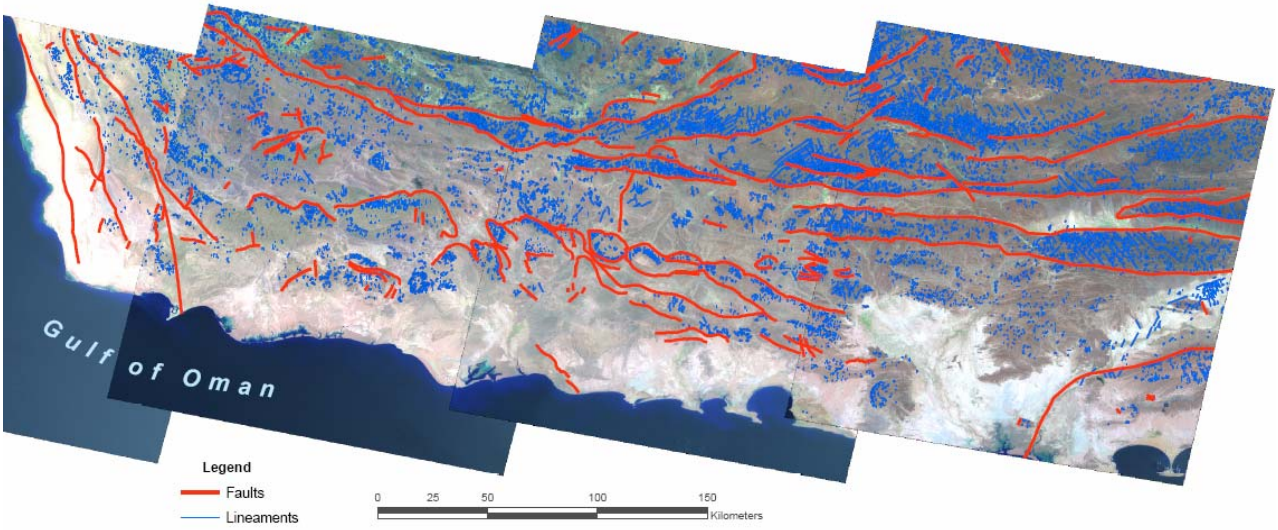

Figure 5.10: Major faults in the study area. Blue lines represent the lineaments (fractures).

The faults generally trend WNW-ESE in the southern (i.e., younger parts) of the prism, E-W in the middle part, and ENE-WSW in the northern, older part of the prism. The faults in the western part of the prism are elements of the Minab-Zendan fault system. The overall trend of the faults in the accretionary complex ranges between 90^{o} and 108^{o} (i.e., E-W).

The attitudes (i.e., strike, dip and the dip direction of the fault plane as opposed to just the trend of fault trace) of several of the E-W trending thrust faults in the study area

were calculated. False color composites calculated from combining digitally enhanced Landsat ETM+ bands 7, 4 and 2 (Figure 3.6) and the digital elevation models derived from the Shuttle Radar Topographic Mission (SRTM-DEM) were used to calculate the true attitude of the E-W trending thrust faults. To calculate the attitude, several structural contours were determined and plotted at specific locations on the plane of thrust fault. A structural-contour map is a map on which contour lines represent lines of equal elevation on a structurally significant surface such as a fault surface (Marshak and Mitra, 1988, p. 27). Structural contour lines are linear or curvilinear lines that are drawn by connecting the points on a lithological or structural surface that intersects the same topographic elevation at more than one location.

Figure 5.11 shows the attitude of a thrust fault calculated by drawing structural contours with the help of a satellite image and DEM. Structural contours are drawn at 1,060 m and 1,015 m asl (above sea level). The horizontal distance between the two structural contours was measured as 202 m. By definition, the structural contours are parallel to the strike of the thrust plane (Xu et al., 2004). Using trigonometry, the strike of the thrust plane is estimated to be N85E. The direction of the dip was determined from the pattern in the values of the structural contours. Since the structural contours values decrease from SE to NW along the fault, the thrust plane was determined to dip toward NW. The amount of dip of the thrust plane (i.e., dip angle) was calculated to be about 12^{o} using the following formula;

Dip angle (θ) = arc tan (elevation difference between the structural Contours/distance between them)

$\theta = \text{arc tan } \{(1060\text{-}1015)m/202m\} = \text{arc tan } (45/202) = 12.5^{o}$

$\theta = \sim 12^{o}$

Overall, the attitude of the major faults were estimated using this technique in the study area in 15 different locations (Figure 5.12) which are listed in Table 5.2. Most of the faults are north-diping low-angle thrust faults. Four out of these 15 faults are found to dip to the south.

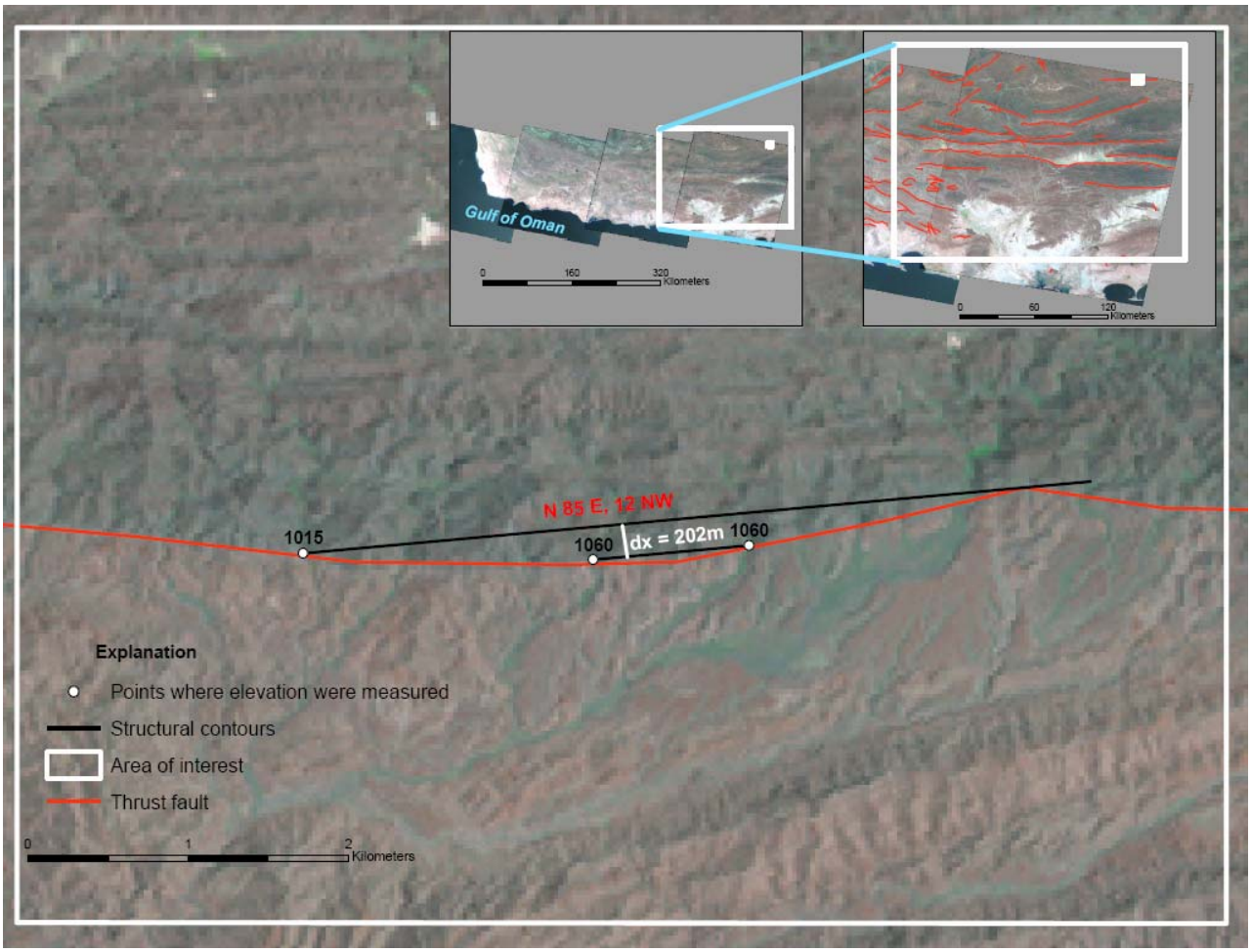

Figure 5.11: Attitude of the thrust fault (strike, dip angle and dip direction) measured by drawing structural contours. White points are the locations where elevations were measured using the DEM. Black straight lines are structural contours drawn at two different elevation levels where they are intersected by the thrust plane.

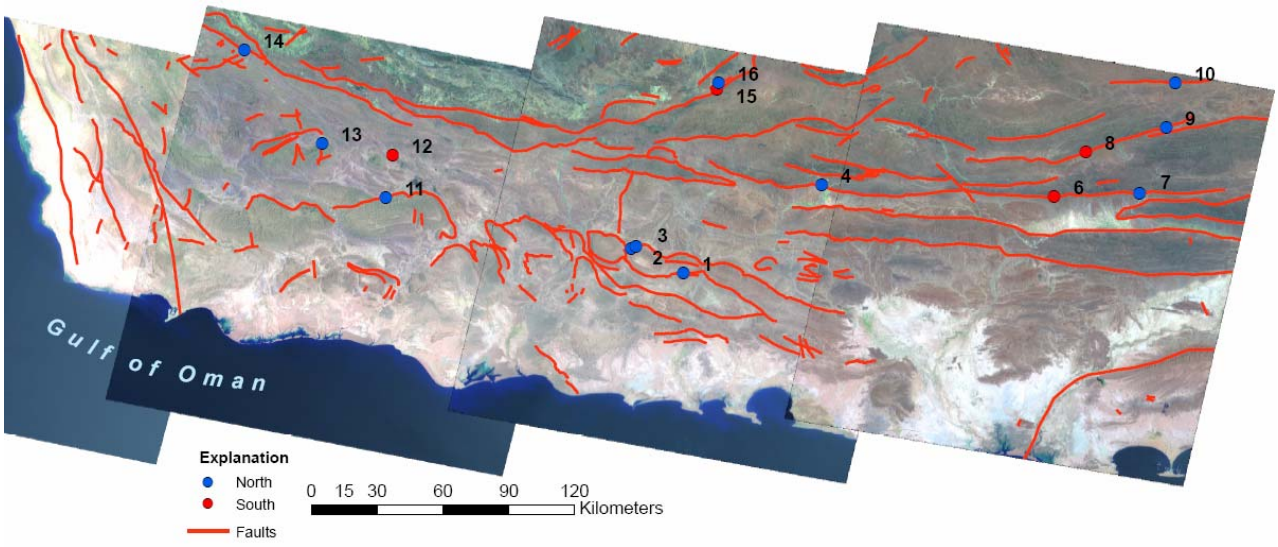

Figure 5.12: Points showing the locations where the attitudes of the faults were measured. Red lines are major faults mapped in the study area. Blue points represent the north diping thrust fault location. Red points represent south diping faults. The numbers represent the unique identification number (See Table 10.11 for the attitudes).

The northward increase in amount of the fault dip angles agree with the northward increase in the dihedral angle between the two conjugate sets of shear fractures (2α), from south (coastal Makran) to north across the prism. In the accretionary prisms, older rocks are found on top of younger rock sequences and are subjected to prolonged contractional tectonics during accretion. In the study area, the northern part consists of older rock sequences that were subjected to the contraction and related rotation, which led the increase in dip angle of the fault planes. A study done by Grando and McClay, 2007, suggests that the rear (north) portion of the Makran accretionary wedge is uplifted and extended by normal faulting and ductile flow. There conclusion supports the finding of this study that, the deformation changes from brittle to ductile from south to north. The normal faulting is evident by the presence of relatively high angle south dipping faults as shown in Figure 5.12.

Table 5.2: Attitude of the faults measured in 15 locations in the study area (see Figure 5.12 for the locations).

ID	Strike	Dip Amount	Dip Direction
1	EW	1.7	N
2	N60E	10	NE
3	N72E	2.4	NW
4	N74W	3	NE
5	N87E	9.2	SE
6	N86E	12	NW
7	N81E	7	SE
8	N81E	10	NW
9	N85E	12.5	NW
10	N75E	16	NW
11	N53W	7.4	SW
12	N80E	3	NW
13	N84E	3	NW
14	N53E	6	SE
15	N64E	9.7	NW

5.3 Fold analysis

I used the hillshade maps derived from the SRTM-DEM, the geological map produced by National Iranian Oil Company (NIOC, 1977), and the digitally enhanced satellite imageries with band combinations of 7, 4 and 2 (Figure 3.6) to identify and map the fold axial traces in the study area. The main purpose of the fold analysis was to determine the relationship of fault and fold, and to unravel the internal architecture of the prism. The fold axial traces reveal the folded structure of the thrust sheets, which is also apparent on reflection seismograms of the subducting sediments (Schluter et al., 2002; Grando and McClay, 2007). More than 65 fold axial traces of both synclines and

anticlines were identified and digitized (Figure 5.13). The mean orientation of the fold axial traces were found to be E-W, which is subparallel to the E-W striking major faults in the study area, and perpendicular to the N-S orientated vector of convergence in the subduction zone determined from the orientation of the calculated maximum principal stress (σ_1).

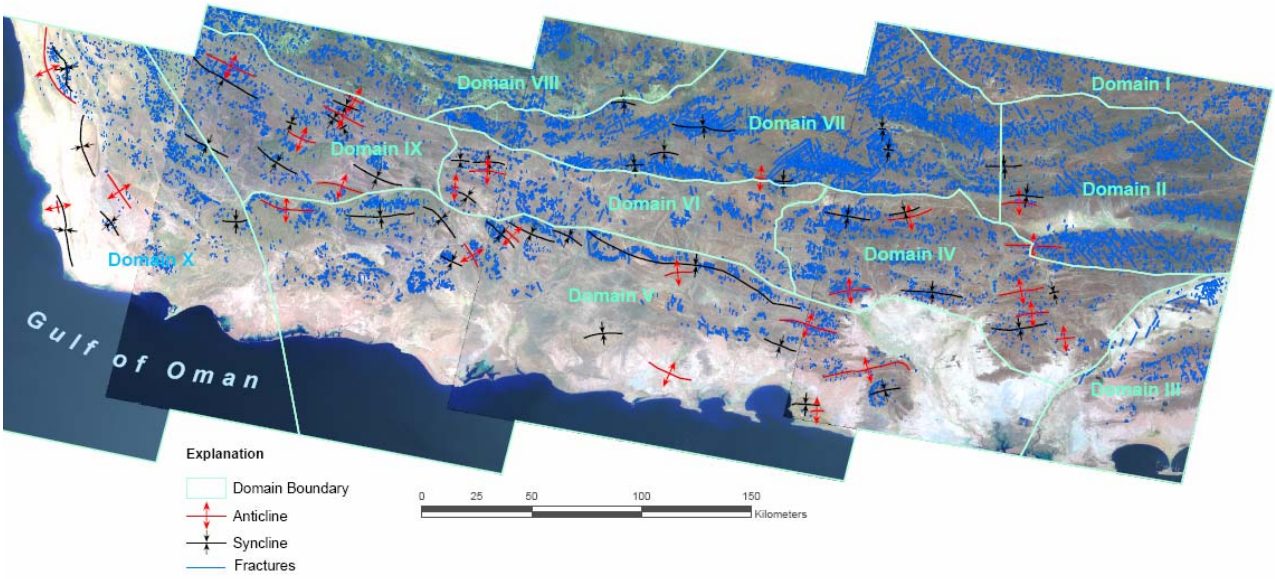

Figure 5.13: Axial traces of the folds mapped in the study area.

In addition, four elliptical synclinal fold basins were also identified in domain V (Figure 5.14). These synclinal basins were probably formed during offscarping and related folding of sediments due to the nearly N-S contraction, which is evident, by mutually non-orthogonal principal axes of the ellipses as shown in figure 5.14. These are comprised of sandstone with siltstone and some conglomerate of the Makran unit (Figure 2.2).

I used the Wellman strain measurement method to estimate the strain ellipse related to the deformation of these deformed basins. The Wellman method, which is

usually applied to the strain measurement of deformed fossils (Ramsay, 1967, p. 242; Marshak and Mitra, 1988, p. 346; Twiss and Moores, 2007, p. 455), is described bellow:

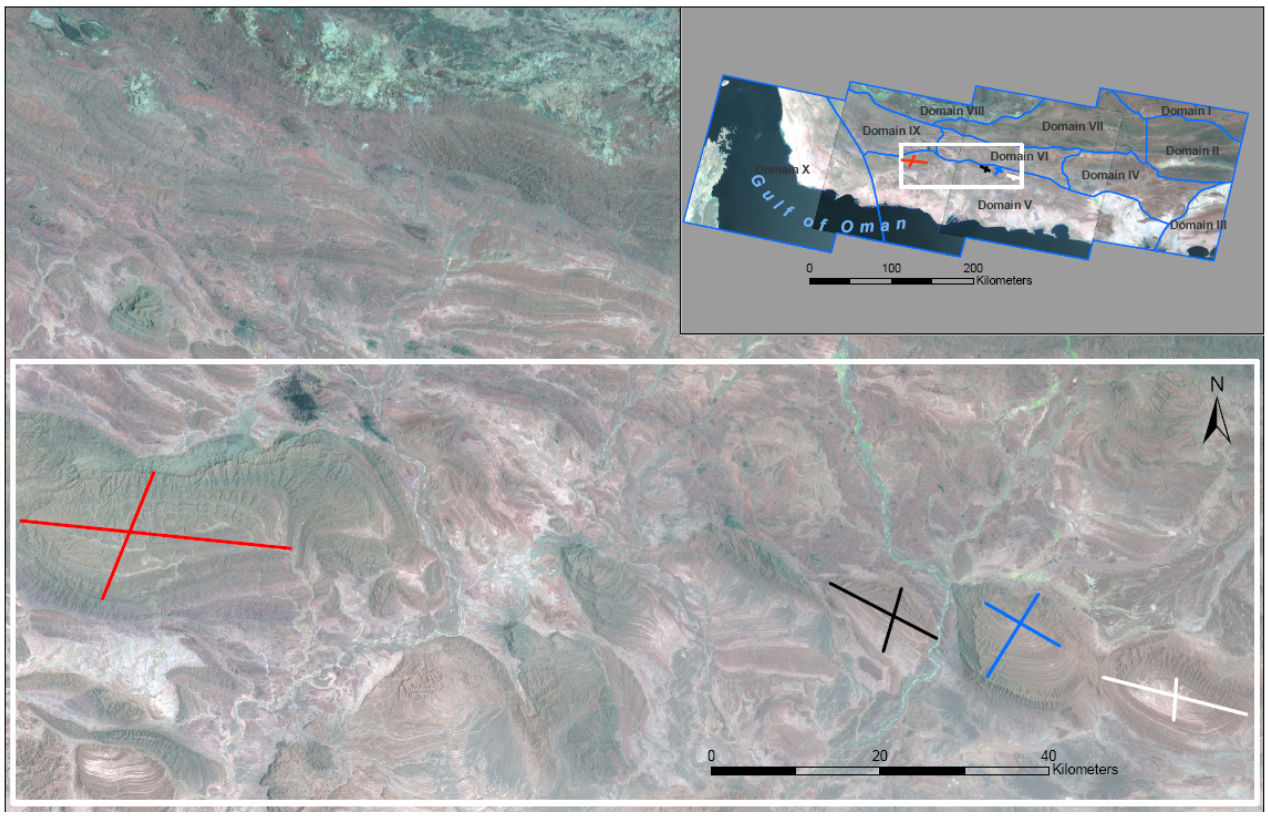

Figure 5.14: Map showing location in domain V where E-W trending elliptical syncline fold basins were used for the Wellman method of strain measurement.

The Wellman method for determining the strain is based on the geometric fact that any angle inscribed in a semicircle is necessarily a right angle (Twiss and Moores, 2007, p. 455). Two perpendicular lines of any given orientation, constructed from the opposite ends of any diameter of a circle, intersect on the circumference of the circle (Twiss and Moores, 2007, p. 455). After a homogeneous strain, any semicircle based on a diameter becomes a semi-ellipse but it still intersect on the circumference of the newly formed ellipse (Twiss and Moores, 2007, p. 455).

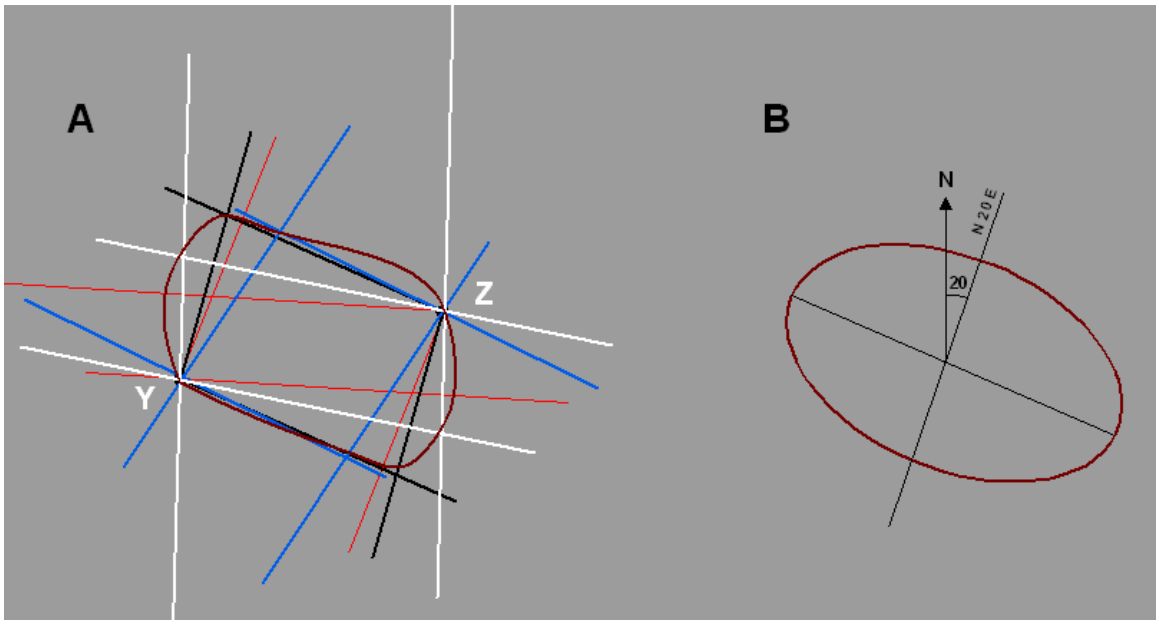

Figure 5.15: Wellman method of strain measurement. (A) Transformation of the fold axes of the folds. (B) Best fit strain ellipse.

The major and minor principal axes of the four ellipses were mapped. Two reference points Y and Z were chosen arbitrarily as shown in figure 5.15 (A). All the principal axes of the deformed folds were transferred individually through the reference points Y and Z, and extended until they intersected (Figure 5.15 (A)). Each pair of orientations generated two intersections, which lie on the strain ellipse. A best-fit ellipse was drawn through these points of intersections as shown in Figure 5.15 (B). The principal axes of the strain ellipse thus derived, defined the orientation of the principal stretches (Twiss and Moores, 2007, p. 455). The minor principal strain axis is parallel to the maximum principal shortening (Z), which is assumed to parallel the maximum principal direction of stress (σ_1). The shortening direction is calculated to be N20E (Figure 5.15 (B)). This value is 13^o off the N7E orientation of σ_1 calculated from fracture

orientation analysis as shown in Figure 4.10 (A) and (B). This discrepancy is probably due to the small number of the elliptical basin used in one single domain (i.e., 4 elliptical folds in domain V) in the study area,. The extensional set of fractures range from N10W to N10E in domain V, and there is a minor set with mean trend of N15E in this domain (Figure 4.10 (A) and (B)), which might also be an explanation for the discrepancy. The western part of the domain V is close to the Minab-Zendan fault system (Figure 5.16), where the direction of maximum principal stress is calculated to be oriented along N15E (in domain X), as shown in Figure 4.14 (A) and (B). The discrepancy may also be due to the influence of the NW-SE orientated right lateral Minab-Zindan fault system.

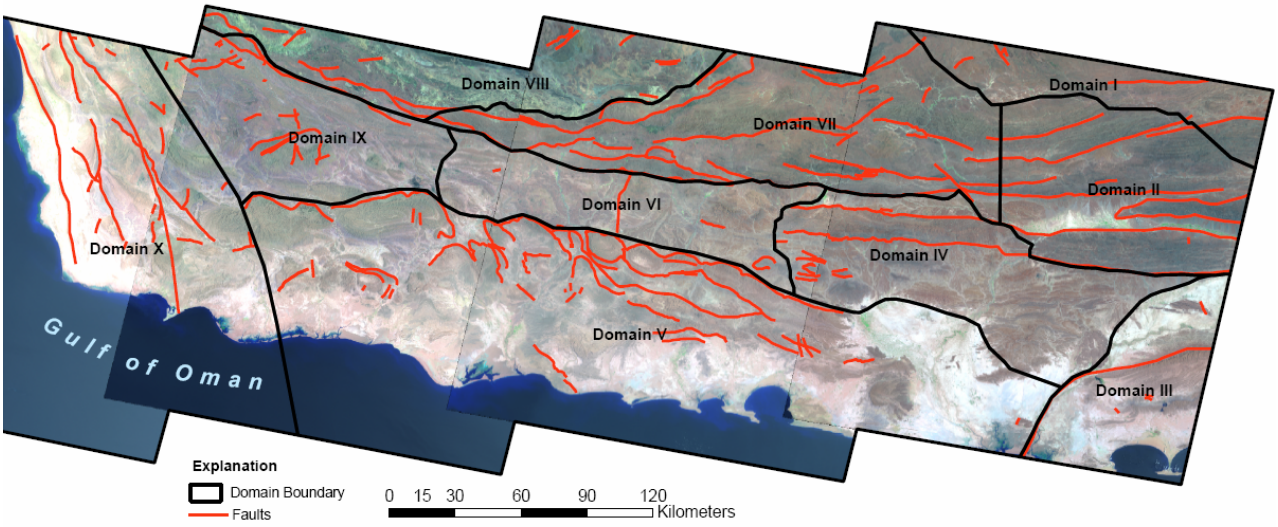

Figure 5.16: Major faults in the study area with domain boundary.

A fold with its axial trace trending N87E is also identified in the Landsat band combination 7, 4, and 2 in the northeastern part of domain I (Figure 5.17). Assuming that the orientation of the maximum principal compressive axis (σ_1) is perpendicular to the fold axial trace, the orientation of σ_1 is calculated to be N3E, which agrees well with the value of N2E estimated from the lineaments analysis in domain I (Table 5.1).

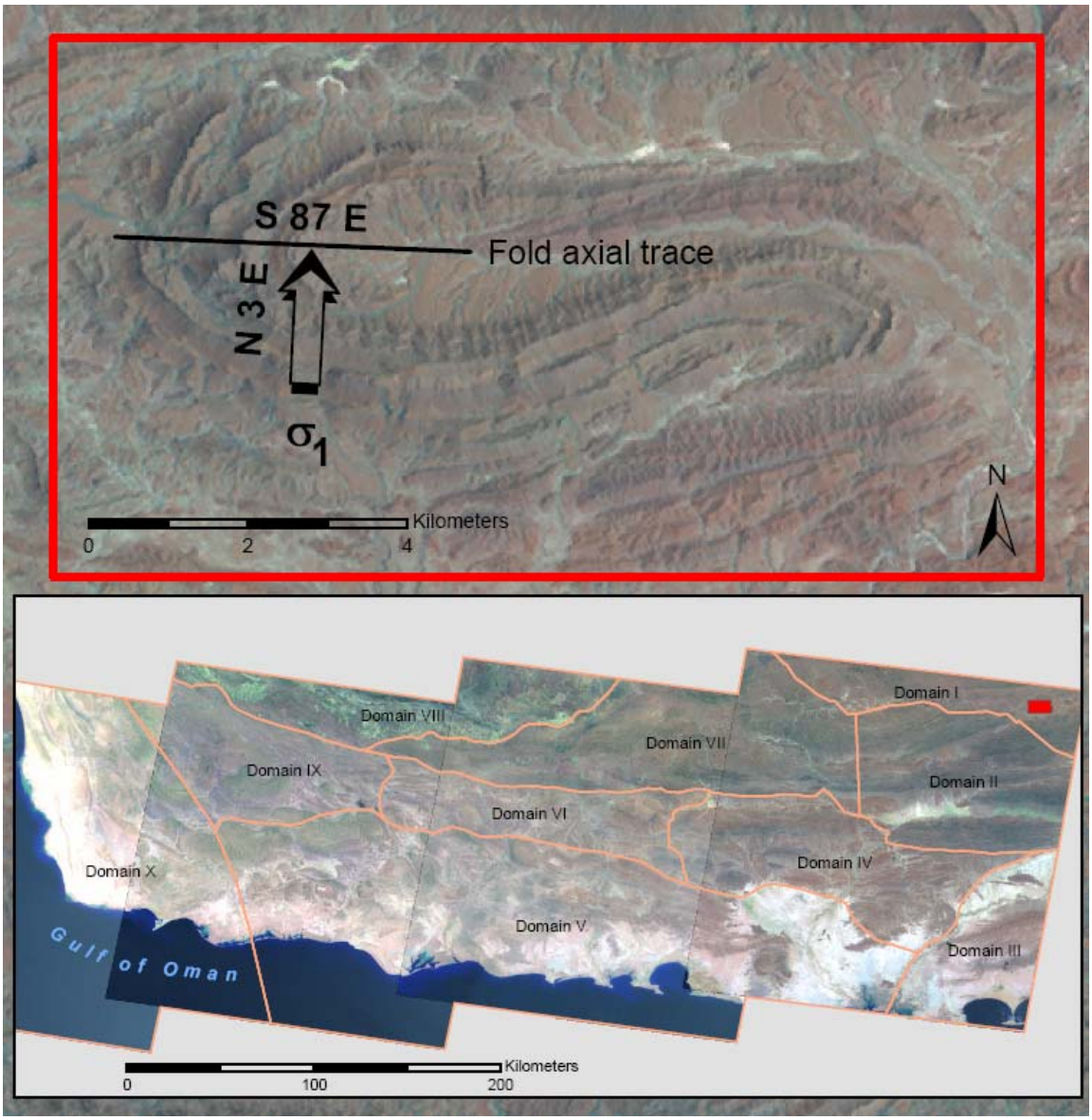

Figure 5.17: A fold with E-W trending axial trace identified in domain I, which was used to estimate the σ_1 direction in domain I.

5.4 Earthquake data analysis

The level of seismicity in the Makran accretionary is low. However, there are significant numbers of earthquakes to the west of the prism in the Zagros Fold and Thrust Belt (ZFTB) (Figure 5.18). The transition from the collision in the ZFTB to the subduction in the Makran accretionary prism is marked by a sharp contrast in seismicity

(Byrne et al., 1992). There are about 11 seismic events documented in and near the study area (Figure 5.19). A List of seismic events recorded in the past with their location, depth and magnitude are given in Table 5.3. In the Makran accretionary prism, the seismicity increases from the west to east(i.e., from Iranian Makran to Pakistani Makran). The transition zone between the aseismic to seismic zone is almost parallel to the Sistan suture zone (Byrne et al., 1992), where notable numbers of earthquakes have been observed in the past (Figure 5.19). The convergence rate of the Arabian plate under the Eurasian plate is about 3.65 cm/yr in the western Makran, and about 4.2 cm/yr in the eastern Makran (DeMets et al., 1990). This may be responsible for the low number of seismic activities in the western part of the Makran accretionary prism. In addition, a number of mud volcanoes have been found in several places along the Makran coast (Grando and MaClay, 2007), which are aligned along the thrust anticline, and their numbers and sizes seem to decrease from east to west (Grando and McClay, 2007). This also agrees with the low number of seismic events recorded in the western part of the accretionary prism.

Table 5.3: List of 11 seismic events recorded in and around the study area with their time, coordinate of the epicenter, magnitude, attitude of both of the nodal planes and trend and plunge of the compressional (P) and extensional (T) axes.

Attributes of Study_area_Quakes

ID	YEAR	MONTH	DAY	LAT	LON	DEPTH	MAGNITUD	STRIKE_1	DIP_1	STRIKE_2	DIP_2	P_Azi	P_Plung	T_Azi	T_Plunge
1	1979	1	10	26.75	61.23	15	6	338	62	234	65	195	39	287	2
2	1979	1	10	26.75	61.31	15	6.1	328	58	227	72	184	36	280	9
3	1980	1	1	26.99	60.27	64.1	5.4	208	80	118	88	72	8	163	5
4	1983	2	7	26.28	57.21	33	5.9	5	42	101	85	224	27	335	36
5	1992	12	17	25.68	61.43	37	5.7	8	54	123	60	244	4	339	51
6	2003	6	24	27	60.91	72.4	5.5	97	45	244	50	89	73	350	3
7	2004	1	28	26.75	57.36	29.8	5.2	27	59	127	73	254	9	351	34
8	2005	3	13	26.73	62	58	6	253	37	72	53	340	82	162	8
9	1989	12	7	25.59	58.86	15	6	142	37	305	54	43	8	177	78
10	2005	3	13	27.09	61.87	56	6	257	37	72	53	328	81	164	8
11	2006	7	18	26.07	61.23	30.8	5.3	107	67	201	79	66	24	333	8

Record: 1 Show: All Selected Records (0 out of 11 Selected.) Options

The earthquake data derived from the USGS National Earthquake Information Center show that the depth of the earthquakes varies from 15 km to more than 72 km (Table 5.3). The beach ball diagrams derived from the earthquakes focal mechanism solutions (lower hemisphere projection of the earthquakes nodal planes with the orientation of the P-axis (compressional axis) and T-axis (dilatational axis) show that most of the deep earthquakes occurred along normal fault planes (Figure 5.20). It is assumed that, the maximum compressive stress (σ_1) bisects the angle between the two nodal planes in the dilatational quadrant and perpendicular to the line of intersection between the nodal planes (Twiss and Moores, 2007, page 236). The calculated angle of 45^o between σ_1 and the shear plane is consistent with the Von Mises criterion for ductile flow, but not with the Coulumb fracture criterion (also see Figure 5.8) which requires σ_1 to lie approximately 30^o from the shear fracture plane (Twiss and Moores, 2007, page 236).

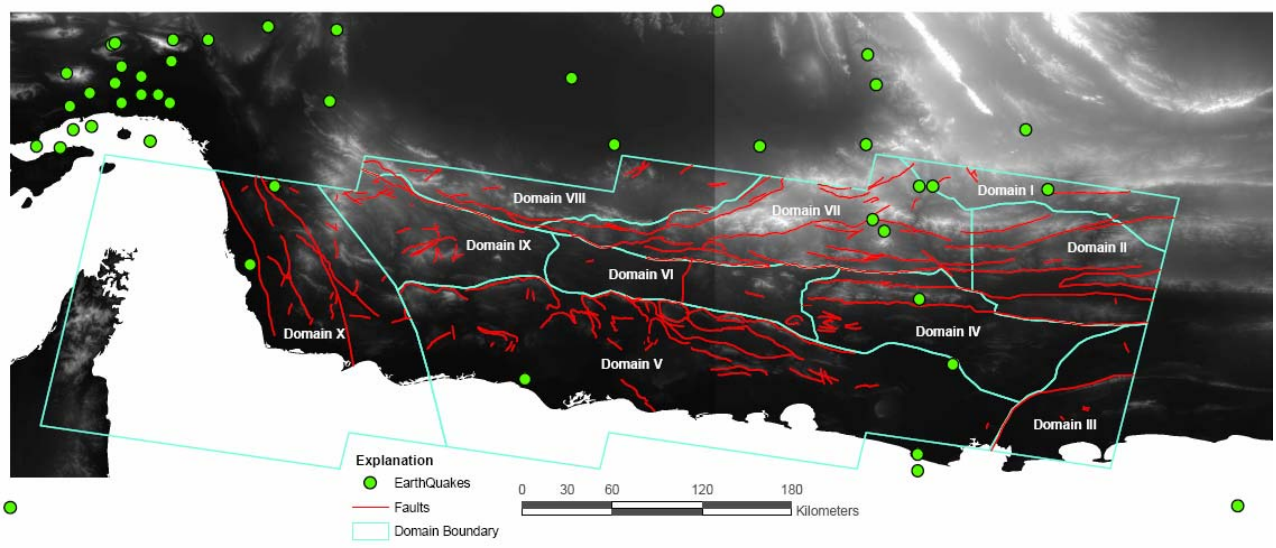

Figure 5.18: Digital elevation model showing the earthquakes in the Makran accretionary prism and the Zagros-Thrust and Fold Belt (ZFTB).

The Makran accretionary prism is one of the world's largest fore arc basins (Byrne et al., 1992). The sediment thickness on the oceanic crust is extremely high, and the dip angle of the subduction is extremely low (Schluter et al., 2002). The seaward 70 km of the Makran accretionary prism consists of more recently accreted, unconsolidated sediments with low seismic velocity (about 4 km/s) and high pore fluid pressures (White, 1982; Fowler et al., 1985). Unconsolidated sediments exhibits higher coefficients of friction at highest slip velocities, causing a resistance to the accelerating slip associated with earthquakes (Marone and Scholz, 1988). The absence of seismicity in the study area indicates either the western accretionary prism is being subducted aseismically or, the subduction is currently locked and experiences great earthquakes with long repeat times.

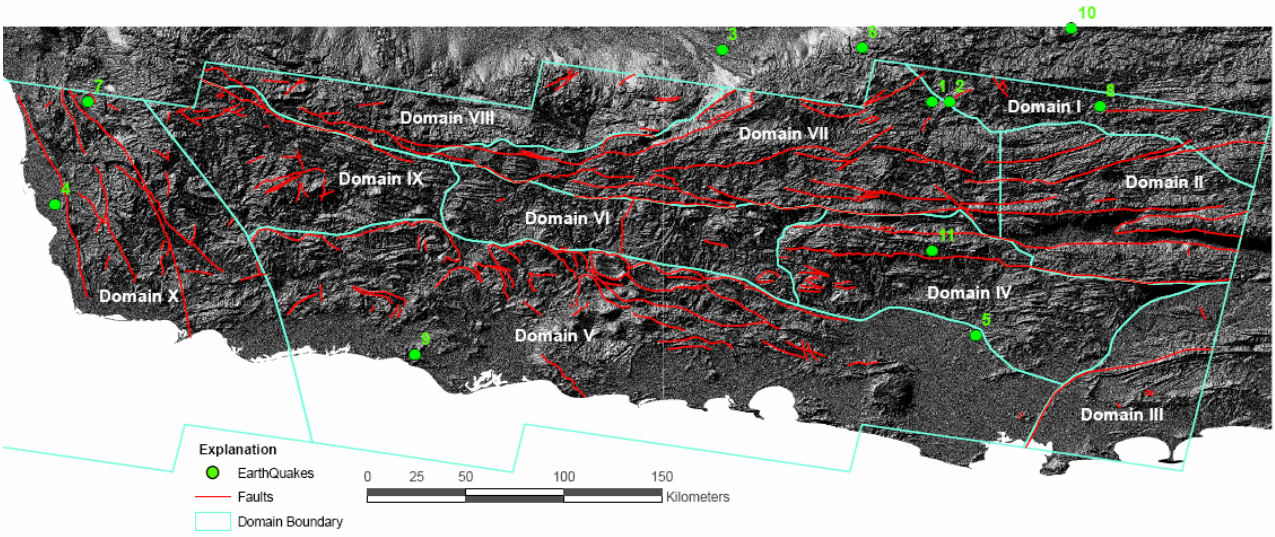

Figure 5.19: Hillshed map showing the 11 earthquakes in and around study area which focal mechanism have been analyzed.

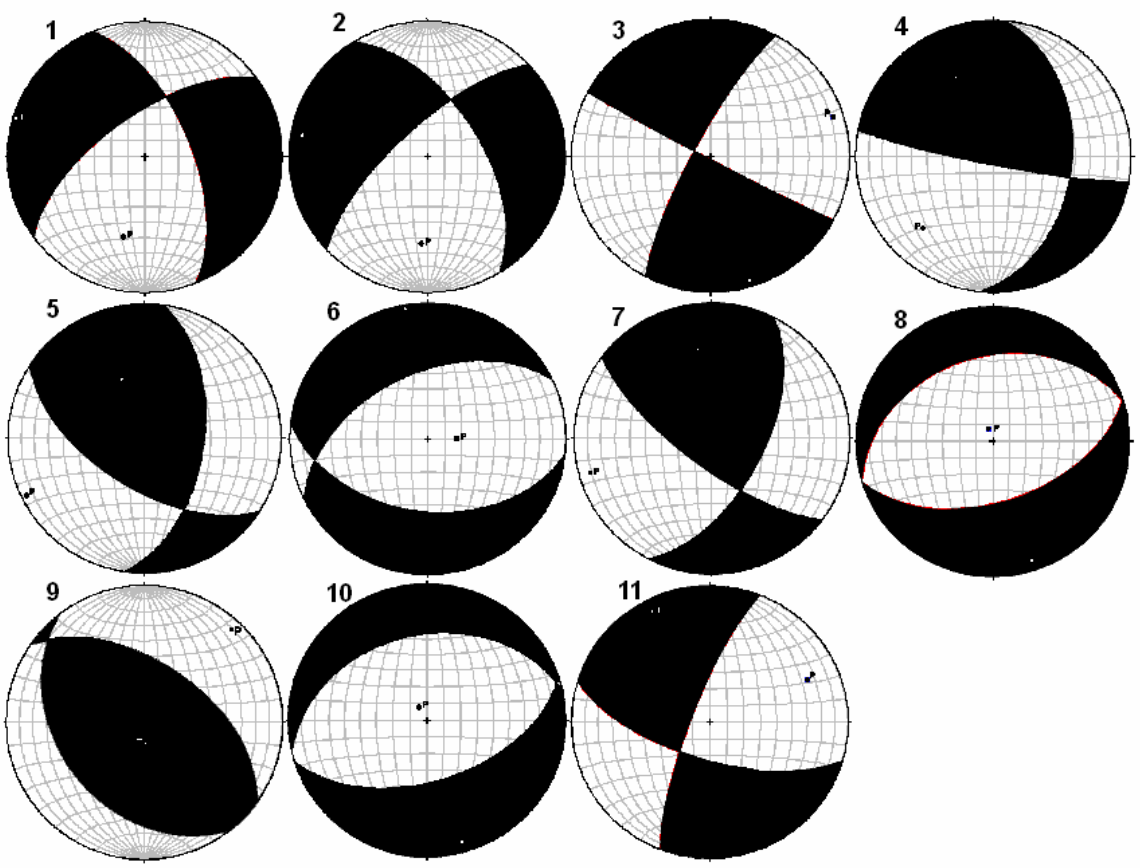

Figure 5.20: Beach ball diagram derived for the 11 seismic events recorded in and around the study area from the focal mechanism of the earthquakes nodal planes. White areas represent compressional regime whereas black areas represent extensional regime.

CHAPTER 6

6.1 Conclusions

The following conclusions are derived from the results of this study:

1. GIS and Remote Sensing are powerful tools for geological and tectonic study in the desert areas like southeast Iran where the geologic structures are well exposed and field visit is difficult due to remoteness and the adverse geopolitical situation of the area. Digitally enhanced Landsat ETM+ bands with spatial resolution of 30 m and digital elevation models (DEMs) with spatial resolution of 90 m, together with geological principals and methodology allowed extraction of most of the linear features such as fractures, fold elements and faults, and analysis of their tectonic significance in the study area.
2. Combination of different image enhancement techniques such as principal component analysis (PCA) and color composite (CC) were effective and suitable for lineament identification for the structurally complex areas like the Makran accretionary prism. The two-line technique and the structural contour method were used with the help of the DEMs to calculate the true attitudes of the fractures and major faults in the study area.
3. Domain-based quantification approach of fractures showed two major systems of fractures. The first system of fractures in domain I to domain IX consists of three major sets associated with the N-S orientated subduction of the Arabian oceanic plate under the Eurasian plate. The NW-SE and NE-SW orientated sets are conjugate sets of shear fractures that formed during the accretionary process. The N-S orientated set represents extensional fractures which form parallel to the direction of maximum

principal compressive stress (σ_1). The direction of σ_1 determined from the kinematics analysis of these fractures ranges from N6W to N7E, which is consistent with the N-S subduction. The second system of fractures in domain X are in close proximity (i.e., about 50 km) to the Minab-Zendan right-lateral, strike slip fault system.

The second system consists of five sets of fractures associated with the NW-SE oriented Minab-Zendan strike slip fault system. The development of the subsidiary reidel shear (R), which is synthetic to the Minab-Zendan fault system, and the conjugate reidel shears (R'), which is antithetic to the fault systems, indicates the changing of the deformation style from pure shear to simple shear as the structural style transitions from the subduction tectonics to the east, to the collision tectonics to the west across the Makran accretionary prism.

4. Fracture analysis also showed that the dihedral angle (2α) between the conjugate sets of fractures increases from southeast to northwest across the study area. The north ward gradient in the value of 2α may be due to the transition from brittle deformation defined by the Coulomb criterion to ductile deformation defined by the Von Mises criterion as the confining pressure increases from south to north across the accretionary prism.
5. The amount of true dip of the major faults in the prism, estimated by drawing structural contours from the satellite imageries and the DEM, shows a northward increase. The gradient in the fault dip angle, which parallels the northward increase in the angle of 2α between conjugate fractures, is consistent with accretionary tectonics, and supports the argument that the deformation style changes from brittle to ductile from the south to the north across the prism.

6. The axial planes of 65 major fold axial traces have an E-W mean orientation, which is sub parallel to the E-W orientated major faults in the study area. These faults and fold axial traces are formed perpendicular to the N-S direction of convergence of the plates.
7. The N20E orientation of $\sigma_{1,}$ estimated applying the Wellman method of strain measurement to the elliptical synclinal fold basins is 13^{o} off the N7E orientation of σ_1 calculated from fracture analysis. This discrepancy is probably due to the small number of elliptical folds identified in the study area or, because of the influence of the NW-SE orientated Minab-Zendan fault system on the stress calculation using fractures.
8. The level of seismicity in the Makran accretionary prism is significantly low. The beach ball diagrams derived from the earthquakes focal mechanism solutions show that most of the deep earthquakes occurred along normal fault planes. The calculated angle of 45^{o} between σ_1 and the shear plane is consistent with the Von Mises criterion for ductile flow, but not with the Coulumb fracture criterion which requires σ_1 to lie approximately 30^{o} from the shear fracture plane.

REFERENCES

Abarca, M.A.A., 2006, Lineament extraction from digital terrain models: case study San Antonio del Sur area, south-eastern Cuba. Masters of sciences in geoinformation science and earth observation thesis, International Institute for Aerospace Survey and Earth Observation (ITC).

Ali, S.A. and Pirasteh, S., 2004, Geological applications of Landsat Enhanced Thematic Mapper (ETM) data and Geographic Information System (GIS): mapping and structural interpretation in south-west Iran, Zagros Structural Belt: International Journal of Remote Sensing, v. 25, no. 21, p.4715-4727.

Anderson, E.M., 1951, The dynamics of faulting and dyke formation with application to Britain: Oliver and Boyd, 2nd edition, Edinburgh.

Barsi, J.A., Schott, J.R., Palluconi, F.D., Helder, D.L., Hook, S.J., Markham, B.L., Chander, G., and O'Donnell, E.M., 2003, Landsat TM and ETM+ thermal band calibration: Canadian Journal of Remote Sensing, v. 29, p.141-153.

Barzi, M.H., and Talbot, C.J., 2003, A tectonic pulse in the Makran accretionary prism recorded in Iranian coastal sediments: Journal of the Geological Society, London, v. 160, p.903-910.

Byerlee, J., 1978, Friction of rocks: Pure Applied Geophysics, v. 116, p.615-626.

Byrne, D.E., Sykes, L.R., and Davis, D.M., 1992, Great thrust earthquakes and seismic slip along the plate boundary of the Makran subduction zone: Journal of geophysics, v. 97, p.449-478.

Campbell, J.B., 1987, Introduction to Remote Sensing: The Guilford Press, New York, 493 pp.

Canas, A., and Barnett, M., 1985, The generation and interpretation of false-colour composite principal component images: International Journal of Remote Sensing, v. 6, p.867-881.

Chavez, P.S., Guptill, S.C., and Bowell, J.A., 1984, Image processing techniques for thematic mapper data: American Society of Photogrammetry, p.728-743.

Clark, C.D., Wilson, C., 1994, Spatial analysis of lineaments: Computers and Geosciences, v.20, p.1237-1258.

Davis, G.H., 1984, Structural Geology of Rocks and Regions: Wiley, New York, 475 pp.

Dehls, J.F., Cruden, A.R., and Vigneresse, J.L., 1998, Fracture control of later Archean emplacement in the northern Slave Province: Journal of Structural Geology, v.20, p.1145-1154.

DeMets, C., Gordon, R.G., Argus, D.F., and Stein, S., 1990, Current plate motions: International Journal of Geophysics, v. 101, p.425-478.

Faust, N.L., 1989, Image enhancement. In: Kent, A., and William, J.G. Editors, 1989. Encyclopedia of Computer Science and Technology: Marcel and Dekker, New York.

Fisher, J.I., and Mustard, J.F., 2004, High spatial resolution sea surface climatology from Landsat thermal infrared data: Remote Sensing of Environment, vol. 90, p.293-307.

Fowler, S.R., White, R.S., and Louden, K.E., Sediment dewatering in the Makran accretionary prism: Earth and Planetary Science Letters, v. 75, p.427-438.

Gonzalez, R., and Woods, R., 1993, Digital Image Processing: Addison-Wesley Publishing Company, Menlo Park, CA, p.148-156.

Grando, G., and McClay, K., 2007, Morphotectonics domains and structural styles in the Makran accretionary prism, offshore Iran: Sedimentery Geology, v. 196, p.157-179.

Hancock, P., 1985, Brittle microtectoics: principles and practice: Journal of Structural Geology, v. 7, p.437-458.

ITC, 2001, ILWIS 3.0 Academic User's Guide: International Institute for Aerospace Survey and Earth Sciences, Enschede.

Jansson, K.N., and Glasser, N.F., 2005, Using Landsat 7 ETM+ imagery and Digital Terrain Models for mapping glacial lineaments on former ice sheet beds: International Journal of Remote Sensing, v. 26, no. 18, p.3931-3941.

Jensen, J.R., 1996, Introductory digital image processing: a remote sensing perspective: London, Prentice-Hall Inc., 2nd edition, p.172-176.

Karnieli, A., Meisels, A., Fisher, L., and Arkin, Y., 1996, Automatic extraction of geological linear features from digital remote sensing data using a Hough Transform: Photogrammetric Engineering & Remote Sensing, v.62, p.525-531.

Koike, K., Nagano, S., and Ohmi, M., 1995, Lineaments analysis of satellite images using a Segment Tracing Algorithm (STA): Computers and Geosciences, v.21, p. 1091-1104.

Kopp, C., Fruehn, J., Flueh, E.R., Reichert, C., Kukowski, N., Bialas, J., and Klaeschen D., 2000, Structure of the Makran subduction zone from wide angle and reflection seismic data: Tectonophysics, v. 329, p.171 – 191.

Kukowski, N., Schillhorn, T., Huhn, K., Rad, V.U., Husen, S., and Flueh, R.E., 2001, Morphotectonics and mechanics of the central Makran accretionary wedge off Pakistan: Marine Geology, v. 173, p.1-19.

Lacombe, O., Mouthereau, F., Kargar, S., and Meyer, B., 2006, Late Cenezoic and modern stress fields in the western Fars (Iran): Implication for the tectonic and kinematic evolution of central Zagros: Tectonics, v. 25, TC1003,doi:10.1029/2005TC001831.

Leech, D.P., Treloar, P.J., Lucas, N.S., and Grocott, J., 2003, Landsat TM analysis of fracture patterns: a case study from the Coastal Cordillera of northern Chile: International Journals of Remote Sensing, v. 24, p.3709-3726.

Leica Geosystems, 1999, ERDAS Field Guide Fifth Edition: ERDAS, Inc., Atlanta, GA.

Lillesand, T.M., and Kiefer, R.W., 2000, Remote Sensing and Image Interpretation: New York, John Wiley & Sons.

Mabee, S.B., Hardcastle, K.C., and Wise, D.W., 1994, A method of collecting and analyzing lineaments for regional-scale fractured bedrock aquifer studies: Ground Water, v. 32, p.884-894.

Marone, C. and Scholz, C.H., 1988, The depth of seismic faulting and the upper transition from stable to unstable slip regimes: Geophysical Research Letters, v. 15, p.621-624.

Marshak, S., and Mitra, G., 1988, Basic method of structural geology: Prentice-Hall, Inc. NJ.

Masoud, A., and Koike, K., 2006, Tectonic architecture through Landsat-7 ETM+/SRTM DEM-derived lineaments and relationship to the hydrogeologic setting in Siwa region, NW Egypt: Journal of African Earth Sciences, v. 45, p.467-477.

McCall, G.J.H., 1983, Mélanges of the Makran, southern Iran, In: Ophiolitic and related mélanges, Benchmark Papers in Geology, v. 66, p.292-299.

McCall, G.J.H., 1997, The geotectonic history of the Makran and adjacent areas of southern Iran: Journal of Asian Sciences, v. 15, p.517-531.

McCall, G.J.H., 2003, A critique of the analogy between Achaean and Phanerozoic tectonics based on regional mapping of the Mesozoic-cenozoic plate convergent zone in the Makran, Iran: Precambrian Research, v. 127, p.5-17.

Mostafa, M.E., and Bishta, Z.A., 2005, Significance of lineament patterns in rock unit classification and designation: a pilot study on the Gharib-Dara area, northern eastern desert, Egypt: International Journal of Remote Sensing, v. 26, p.1463-1475.

Mustard, J.F., and Sunshine, J.M., 1999, Spectral analysis for earth science: Investigations using remote sensing data: Remote sensing for earth sciences: Manual of remote sensing: John Wiley and Sons, Inc., 251-306 pp.

Nalbant, S., and Alptekin, O., 1995, The use of Landsat Mapper imagery for analyzing lithology and structure of Korucu-DuZla area in western Turkey: International Journal of Remote Sensing, v. 10, p.2337-2374.

Nama, E.E., 2004, Lineament detection on Mount Cameroon during the 1999 volcanic eruptions using Landsat ETM: International Journal of Remote Sensing, v. 25, p.501-510.

NIOC, 1977, Geological map of Iran: National Iranian Oil Company, Sheet no. 6, South East Iran, scale 1:1, 000, 000.

North, H.C., and Pairman, D., 2001, Edge detection as a starting point for remote sensing scene interpretation: IEEE, p.2994-2997.

O'Learly, D.W., Friedman, J.D., and Pohn, H.A., 1976, Lineament, linear, lineation: some proposed new standards for old terms: Bulletin of the Geological Society of America, v. 87, p.463-1469.

Platt, J.P., Leggett, H.K., Young, J., Raja, H., and Alam, S., 1985, Large scale sediment underplating in the Makran accretionary, south-west Pakistan: Geology, v. 13, p.507-511.

Price, N.J., and Cosgrove, J.W., 1990, Analysis of geological structures: Cambridge University Press, Cambridge, 502 pp.

Ramsay, J.G., 1967, Folding and fracturing of rocks: McGraw-Hill Book Company, 242 pp.

Regard. V., Bellier, O., Thomas, J.C., Abbassi, M.R., Mercier, J., Shabanian, E., Feghhi, K., and Soleymani, S., 2004, Accommodation of Arabia-Eurasia convergence in the Zagros-Makran transfer zone, SE Iran: A transition between collision and subduction through a young deforming system: Tectonics, v. 23, TC4007, doi:10.1029/2003TC001599.

Schulter, H.U., Prexl, A., Gaedicke, C., Roeser, H., Reichert, C., Meyer, H., and Daniels V.C., 2002, The Makran accretionary wedge: sediment thickness and ages and the origin of mud volcanoes: Marine Geology, v. 185, p.213-219.

Shearman, D.J., Walkar, G.P.L., Booth, B., and Falcon, N.L., 1976, The geological evolution of southern Iran: the report of the Iranian Makran expedition: The Geographical Journal, v. 142, no. 3, p.393-410.

Sengor, A.M.C., Altiner, D., Cin, A., Ustaomer, T., and Hsu, K.J., 1998, The Tethyside orogenic collage, In: Audley-Charles, M.G., Hallam, A. (Eds.), Gondwana and Tethys: Geological Society and Oxford University Press, Special Publication of the Geological Society, no. 37, p.119-181.

Smith, J., Dolati, A., Bahroudi, A., and Burg, P.J., 2006, Geophysical Research Abstracts, v. 8.

Solomon, S. and Ghebreab, W., 2006, Lineament characterization and their tectonic significance using Landsat TM data and field studies in the central highlands of Eritrea: Journal of African Earth Sciences, v. 46, p.317-378.

Sylvester, A., 1988, Strike-slip faults: Geological Society of America Bulletin, v. 100, p.1666-1703.

Vencent, R.K., 1997, Fundamentals of geological and environmental remote sensing, Upper Saddle River, New Jersey: Prentice Hall.

Suppe, J., 1985, Principes of Structural Geology: Prentice-Hall, Englewood Cliffs, N.J., 537pp.

Taylor, P., 1977, Quantitative Methods in Geography: An Introduction to Spatial Analysis: Boston, Massachusttes, Houghton Mifflin Company.

Twiss, R.J., and Moores, E.M., 2007, Structural Geology, Second Edition: W.H. Freeman and Company, New York, 210pp.

Walker, R.T., 2006, A remote sensing study of active folding and faulting in southern Kerman province, southeast Iran: Journal of Structural Geology, v. 28, p.654-668.

White, R.S., and Louden, K.E., 1982, The Makran continental margin: structure of a thickly sedimented convergent plate boundary, In: Watkinsand, J.S., Darke, C.L. (Eds.). Studies in continental margin geology, Memoirs: American Association of Petrology and Geology, p.499-518.

Xu, S.S., Velasquillo, M.L.G., Grajales, N.J.M., Murrillo, M.G., and Nieto, S.A.F., 2004, Determination of fault slip components using subsurface structural contours: methods and examples: Journal of Petroleum Geology, v. 27, p.277-298.

Yun, S.H., and Moon, M.W., 2001, Lineament extraction from DEM using drainage network: School of Environmental Sciences, Seoul National University, Kwanak: IEEE, p. 2337-2339.

Zumsprekel, H., and Prinz, T., 2000, Computer-enhanced multispectral remote sensing data: a useful tool for the geological mapping of Archean terrain in (semi) arid environment: Computers and Geosciences, v. 26, p.87-100.

APPENDIX

Abbreviation for the geological map shown in Figure 2.2

Ef	= Rhythmically bedded sandstone and shale with minor siltstone, limestone, conglomerate and basic to intermediate volcanic rocks
Eof	= Rhythmically bedded sandstone and shale with volcacoclastic sandstone, minor limestone and tuff
KPedu	= Basalt and basaltic andesite locally with pillow lavas sturcutre
KPef	= Thinly bedded sandstone and shale with siltstone, mudstone, limestone and conglomerate
KPefv	= Crystal tuff, tuffaceous sandstone, recrystallized limestone and sandy limestone
Kugr	= Granite and granodiorite
Kupl	= Pelagic limestone with globotruncana
Kurl	= Late Cretaceous pelagic limestone, radiolarian chert and red shale
M1f	= Rhythmically bedded sandstone, calcareous sandstone, mudstone, gypsiferous mudstone and shale
M2	= Neogene and Miocene red beds
M2gm	= Gypsiferous and calcareous marl, marlstone and mudstone with interbeded siltstone and sandstone
M3ms	= Marl and marlstone, locally gypsiferous and sandstone with interbeded shale and mar l
MPlc	= Polymictic conglomerate, sandstone and mudstone
MPls	= Sandstone with siltstone, mudstone and minor conglomerate
Mlmmi	= Low weathering grey marls alternating with bands of more resistant shelly limestone
Mm1-2	= Undifferenciated Paleogene Flysch
Ms2-3	= Neogene clastics and Paleocene conglomerate

MuPlaj	= Brown to grey, calcareous sandstone and gypsum
OMf	= Rhythmically bedded sandstone and shale with minor siltstone and mudstone
PlQc	= Fluvial conglomerate
Plbk	= Low weathering grey marls alternating with bands of shelly limestone
Plc	= Polymictic conglomerate and standstone
Plms	= Mudstone, locally gypsiferous and sandstone
Pzkb	= Undifferentiated basic schist pelitic schist
Qal	= Stream channel, braided channel and flood plain deposites
Qcf	= Clay flate
Qcsm	= Clay salt marsh
Qft1	= High level piedmont fan and valley terrace deposits
Qft2	= Low level piedmont fan and valley terrace deposits
Qitd	= Intertidal deposits
Qmt	= Undifferentiated marine terraces
Qplc	= Lake deposits
Qs	= Unconsolidated wind blown sand deposits and back shore sand dune
Qsw	= Swamp and marsh
db	= Diabase
gb	= Layered and isotopic gabbros
l	= Refal, coral and algal limestone
om2	= Tectonized association of pelagic limestone, radiolarian chert with basic volcanics
om3	= Pelagic limestone, radiolarian chert and shale with basalt and basaltic

andesite

pd = Peridotite, dunite, harzburgite and serpentinite

sea = Water body

sm2 = Sedimentary mélange, sheared and boudined sediments with no recognizable stratigraphy

tm = Colored mélange, Tectonic mélange associated with ophiolitic components, pelagic limestone, radiolarian chert